ACOUSTIC BEHAVIORS OF POLYMER MICROSPHERES WITH TAILORED CHAIN OR MATRIX STRUCTURES

NG YEAP HUNG

(B. Eng. (Hons.), NUS)

A THESIS SUBMITTED

FOR THE DEGREE OF MASTER OF ENGINEERING

DEPARTMENT OF CHEMICAL AND BIOMOLECULAR ENGINEERING

NATIONAL UNIVERSITY OF SINGAPORE

2004

Acknowledgement

I would like to express my gratitude to my supervisor and mentor, A/P Hong Liang, for his generosities in sharing his knowledge, experience and time with me. I have greatly benefited from his dedication and patience towards research.

Special thanks are also extended to everyone who has either directly or indirectly helped me to accomplish this enjoyable task, especially L. H. Tan.

Table of Contents

Summary

Utilizing the viscoelastic property of a polymer network to attenuate sound waves is an important technology that has been leading to a living environment free of noise pollution. Both in civilian and in military applications, the trend is toward the utilization of lighter weight materials with larger operational temperature range and more diversified of frequency coverage. In this study, three types of novel polymer microspheres were synthesized, and their acoustic damping performances were studied.

The first type of microspheres, having a hybrid core-shell structure, namely poly(methyl acrylate-co-divinylbenzene) (PMADVB) beads wrapped up by a thin and porous Ni-P alloy layer, have been prepared by suspension polymerization and then electroless nickel (EN) plating. Regarding the second type of microspheres, they are characterized of meso-porous structure having crosslinked matrixes of poly(styrene-co-divinylbenzene) [PSTDVB], poly(styrene-co-2-hydroxyethyl acrylate-co-divinylbenzene) [PSTHEADVB] and poly(acrylonitrile-co-divinylbenzene) [PANDVB]. On there three respective microspheres nickel nanoparticles were implanted via chemical reduction method. The last type of microspheres, which owns semi-interpenetrating network (semi-IPN) composed of poly(ethyl acrylate) [PEA] chains and PSTDVB network, has been produced by arranging an in-situ polymerization of ethyl acrylate inside the matrix of PSTDVB beads.

Characterizations of the above three types of microspheres involve the use of Fourier transform infrared spectroscopy (FT-IR), differential scanning calorimetry (DSC), field emission scanning electron microscopy (FE-SEM), and the scanning electron

spectroscopy (SEM) equipped with an Energy Dispersive System (EDS). In addition, the porous features (pore size distribution, porosity and specific pore volume) of beads produced under various synthetic conditions were evaluated by mercury intrusion porosimetry (MIP).

Assessing sound damping performance of the three interested microspherical structures, polymer-metal core-shell, meso-porous, and semi-IPN, is the objective of this research. The attenuation test was undertaken by using the thick membranes (3cm×2mm, made of a particular batch of microspheres and 5 wt % of methylcellulose binder), placed in the mid position of the Perspex testing tube of which a speaker and a microphone were fastened at two ends respectively. The extent of sound absorption was evaluated by the attenuation coefficient ($\alpha \cong I_{Attenuated} / I_{Incidence}$), which is a simplified version of standard impedance tube method. The investigation was carried out using both the high and low audio frequency bands, 100-1000 Hz and 4000-5000Hz. In addition, an exploration into the ultrasonic wave (~35 kHz) absorption feature of the core-shell microspheres was conducted by a chemical means, namely, the chemisorption extent of copper ions on a biomass adsorbent was employed to assess the attenuation of the absorber to the ultrasonic wave with a specific frequency. The measurement was carried out in a home-made double wall ultrasound absorption chamber.

The enhancement of acoustic damping due to introduction of a metal(Ni) shell is accomplished through two mechanisms, i.e. scattering the incident wave by sub-micron metallic-grains and the intrinsic vibration damping by the viscoelastic PMADVB network that converts the sound energy to heat. As to the porous

microspheres, the meso-pores were found to be responsive in dissipating the low audio frequency band, relied on the boundary viscous layer between air and polymer phase. The implantation of Ni nanoparticles onto the porous microspheres increased visco-component of the polymer network and altered the noise damping efficiency by certain extent. Finally, the porous semi-IPN microspheres could apparently relax the incident frequency, and the magnitude of which became large in the higher frequency sound range, and attenuate the higher frequency sound waves more effectively.

These three specially tailored spherical structures display apparent improvements in acoustic damping behavior, although restricted in confined frequency ranges. These materials have great potential for advanced application in the extensional and constrained layer damping system, as the filler in cavity resonator and also utilized independently as the granular precursor of plastic foams or honeycomb damping panels.

Nomenclature and Abbreviations

Chemicals/ Compounds

AN	Acrylonitrile
BPO	Benzoyl peroxide
DI	Deionized water
DVB	Divinylbenzene
EA	Ethyl acrylate
EN	Electroless nickel
HEA	2-Hydroxylethyl acrylate
MA	Methyl acrylate
PEA	Poly(ethyl acrylate)
PMADVB	Poly(methyl acrylate-co-divinylbenzene)
PSTDVB	Poly(styrene-co-divinylbenzene)
PSTHEADVB	Poly(styrene-co-2-hydroxyethyl acrylate-co-divinylbenzene)
PVA	Polyvinyl alcohol
SDS	Sodium dodecyl sulfate
ST	Styrene

Instrumentations

DSC	Differential Scanning Calorimetry
EDS	Energy Dispersive System
FE-SEM	Field Emission Scanning Electron Microscopy
FT-IR	Fourier Transform Infrared Spectroscopy
SEM	Scanning Electron Microscopy

Mathematical Symbols

$\overline{d}$	Number average diameter
t	Time
S(t) %	Swelling ratio
w_t	Weight of the PMADVB beads after swollen for time t
w_0	Dry sample weight
Ni-P wt %	Ni-P percentage weight gained after electroless plating

M_{EN}	Mass of Ni-P plated PMADVB
$M_{Pristine}$	Mass of pristine PMADVB
C	Concentration of adsorbate (copper ions) at time t
k_s	Surface diffusion rate constant
C_0	Initial concentration of the copper(II) ion.
I	Acoustic intensity
c	Plane traveling wave phase velocity
P	Sound pressure at the observation point
P_0	Total incidence sound pressure when there was no damping layer implemented
C^*	Concentration obtained from the control cell
SL	Relative sound level attenuated
α_v	Absorption coefficient due to the existence of non-elastic (or viscous) vibration component of the testing membrane
ω	Angular velocity of the incident sound
M	Mass per unit area of the testing disk
ρ_0	Static value of air density
d	Thickness of the disk
ρ_b	Bulk density of the disk
η	Viscosity of the streaming medium
τ	Tortuosity
ε	Total porosity of the materials
R_{eff}	Effective flow resistance
ψ	Shape factor account of the complexity of the packing system
$\bar{r}$	Mean radius of the pores in the testing disk
k	Complex propagation constant for a porous packing disk
β	Phase constant
γ	Attenuation constant
α_p	Absorption coefficient due to porous packing
α	Effective sound attenuation coefficient
ϕ_v	Contribution term for the intrinsic vibration mechanism
ϕ_p	Contribution term for the flow-related dissipative effect

List of Figures

List of Tables

Chapter 1

Introduction

Utilizing viscoelastic properties of polymers to damp sound waves has been a technology related to the protection of human being from the pollution of noise. The theoretical basis and recent developments of this type of functional polymeric materials have recently been summarized in the book of Jones (2001). Damping, due to the deformation of a polymer matrix, takes place in the glass transition region, which represents the onset of coordinated segment-motions of a polymer. Dynamic mechanical spectroscopy (DMS) characterizes the storage modulus, *E'*, the loss modulus, *E"*, and the loss tangent, $tan\delta$, as functions of temperature and vibration frequency of the polymer sample in question. The storage modulus *E'* decreases rapidly above T_g, while the loss modulus *E"* and the loss tangent ($tan\ \delta$) exhibit maximum values with a few degree difference (Sperling, 2001) in the proximity of T_g. In other words, the elastomer possesses the strongest capability of dissipating mechanical vibration in the form of heat at the peak temperature of *E"*.

Apparently, broadening the peak of loss modulus could increase the dissipation frequency coverage. A wider loss modulus band includes a larger number of excitation states of the segment motions, which in turn respond to a more extensive of frequency of noise. Usually most homo-polymers possess effective vibration attenuation in a rather narrow temperature range of 20~30 ^{o}C around their T_g (Aklonis et al., 1983). However, polymer materials useful for outdoor damping applications should exhibit a high loss factor over a temperature range of 60~80 ^{o}C at least (Yak, 1994). Interpenetrating polymer network (IPN) has been invented as a special matrix effective

for widening the glass transition region (Sophiea et al., 1994; Hu et al., 1997a, 1997b). In the first part of this research, PMADVB was constructed because the T_g of the linear segments between two cross-linking points must be higher than that of the linear homopolymer PMA (5~10 ^{o}C). In addition to this two-end-fixation effect, the existence of 3-, 4-ethylvinylbenzene (from the DVB mixture) units in the linear segments is another factor retarding the segment motions. It is thus expected that the glass transition of segments would be close to the ambient temperature providing appropriate cross-linking degree is created. As expected, the PMADVB network resulted from the monomer feed (with molar ratio of MA / DVB = 4) was found to exhibit a glass transition range inclusive of the ambient temperature.

This work focuses on the investigation into variation of thermal response caused by plating individual PMADVB beads with a thin Ni-P alloy layer (which is essentially an assembly of small metal granules rather than a dense film). In principle, a spherical temperature field could be established rapidly within the particle because Ni-P alloy possesses superior thermal conductivity (4.187~8.374 $W \cdot m^{-1} \cdot K^{-1}$) (Mallory et al., 1990) and radiativity than the styrenic polymer network (ca. 0.03 $W \cdot m^{-1} \cdot K^{-1}$ at 25 ^{o}C) (Zarr et al., 1996). Consequently, the segment-motions in different spherical layers of PMADVB network are expected to become more coordinated. This is regarded as a positive feature for the attenuation of sound and ultrasonic waves. The other anticipated feature is that the metal particles can assist spread incident sound wave towards all directions, which would facilitate destructive interferences.

On the other hand, the porous polymer matrix is considered as one of the effective sound absorption media with high attenuation coefficients because of its high surface

area in contact with air where sound wave travels (Jarzynski, 1990). A high interfacial area exists in the porous polymer matrix since it contains a lot of narrow and tortuous voids (Kuttruff, 2000; Raichel, 2000). This particular structural feature allows it to develop a highly extensive temperature- gradient boundary layer, which is formed because of the occurrence of maximum sound pressure amplitude at the surface of polymer phase (Allard, 1993). The air pressure fluctuations in response to the external sound field causes periodically alternating heat flows toward and from the polymer surface. Consequently, a significant amount of sound energy is withdrawn from the external sound field and converted into heat. In addition, when a sound wave strikes the polymer surface and causes vibrations, rotations and creeping of polymer segments or pendant groups, tiny amounts of heat are generated due to the frictions of these motions or change of potential energy in the polymer phase. Polymer segments locating at polymer-air interface have higher degrees of freedom of motions (in comparison with those packed in the bulk phase) because they feel less constraint of cohesive force (Garbassi et al., 1998, Jo et al., 2002), and as a result, the loss tangent will be promoted with an increase in the contact area. As an example, the polymer foam has excellent sound absorption properties at both medium and low frequencies of the shrill and irritating sound (400-5000 Hz), while rigid porous materials have poor acoustic performances at low frequencies due to the absence of viscoelastic deformation element and only the heat flow occurring at the boundary layer plays a role as addressed above.

The second part of this research focuses attention on a sound absorption medium composed of porous polystyrenic microspheres ($d<50$ μm) but rather than a continuous and porous medium. From the prospective of real applications, polymer microspheres

constitute the basic unit of a paint formula for forming an interior acoustic layer inside buildings or vehicles. In contrast to the continuous porous medium, this micro-spherical powder packing layer could damp sound waves through relative motions among spheres. It is of interest fundamentally to explore the relationship between sound attenuation capacity and the structural characteristics of microspheres, such as porosity, pore-size distribution and glass transition temperature. In addition, the porous framework inside each individual particle offers a space suitable for different types of structural tailoring to improve the acoustic performance.

The porous microspheres composed of prevalent polystyrene network (SD) were synthesized by means of suspension polymerization in which the presence of an effective porogen mixture during formation of the network brought about porous structures. As mentioned above, structural modifications on the resulting SD skeleton have been carried out accordingly: (1) A low molar percentage of 2-hydroxyethylacrylate unit was incorporated (as the polar unit) into the matrix of SD beads to form poly(styrene-co-2-hydroxyethylacrylate-co-divinylbenzene) (SDH) matrix correspondingly; (2) A substantially small portion of Ni nano-particles was deposited onto the matrix of both SD and SDH beads via an immobilizing-reducing procedure; (3) Ethyl acrylate (EA) monomer was arranged to undergo polymerization inside the matrix and pores of SD beads, and as a result, linear chains of PEA penetrate the matrix of SD microspheres to generate the semi-IPN structure, described by the symbol SD*x*EA*y*.

This study aims at understanding of the acoustic absorption of microspheres with the SD framework in the two ends of the concerned frequency range: 100-1000 Hz and

4000-5000 Hz, respectively. The meso-porous structure inside the microspheres offers a perceptible damping effect in the low frequency range in addition to the other attenuation mechanisms. However in the high frequency range, sound waves infiltrating intra-particulate meso-pores become as easy as infiltrating interstice voids among microspheres. Therefore further improvement on the high-frequency acoustic absorption could be pursued by following the two ways: firstly, to enhance the reflection (or scattering) of incident sound waves through raising elastic property and therefore storage modulus of the matrix, this concept has been tested herein by incorporating Ni nano-particles into the SD and SDH matrixes; secondly, to increase the visoelastic damping capability namely the loss modulus component by bringing in the rigid SD matrix a soft polymer to form the semi-IPN. Both efforts have turned out with the expected effects that are also essential for further expanding the advantage of modification.

Chapter 2

Literature Review

2.1 Suspension Polymerization

2.1.1 General Aspect

In this research, suspension polymerization (or beads polymerization) was employed to produce the micron-sized non-porous and porous polymer microspheres. Suspension polymerization is one of the two common heterogeneous polymerization systems; it is used extensively in laboratory and industry mainly for the preparation of spherical polymer beads as the substrates of different types of ion-exchange functional groups, homogeneous catalysts and anchors for synthesis of proteins. Of course, similar to the emulsion polymerization, the suspension polymerization system allows to dissipate polymerization heat effectively and to maintain low viscosity throughout the entire reaction course. The suspension polymerization system comprises water-sparingly soluble monomer (dispersed phase), water or other non-solvent (continuous phase), oil-soluble initiators and suspension stabilizers or dispersants. In this process, the monomer droplets are dispersed in the aqueous phase under suitable agitation, and are protected from coalescing by the suspension stabilizers.

Typical suspension stabilizers used are ionic surfactants and non-ionic water soluble polymers, which can form a colloidal protective skin on the dispersed monomer droplets and then solid polymer particles. Other than these two types of stabilizers, insoluble inorganic fine powders are use to mechanically interfere the coagulation of polymer beads formed. Also electrolytes (e.g. NaCl) can be also added to increase the ionic strength of the continuous phase, facilitate the adsorption of surfactant molecules

on the surface of dispersed phase (Billmeyer, 1984). A number of important polymer products are made by suspension polymerization; they include poly(vinyl chloride) and poly(vinylidine) used for extrusion and injection-molding, styrenic-based polymer beads used for further deriving ion-exchange resins or functional substrate for needs of combinatory chemistry. Moreover, acrylic polymer resins, acrylonitrile, vinyl acetate, and tetrafluoroethylene can be also obtained from this polymerization technique.

2.1.2 Historic View and Current Progress in Suspension Polymerization Technique

Suspension polymerization was developed around early 20 century motivated by the formation of native rubber in aqueous phase, under mild conditions (Grulke, 1989; Hofmann et al., 1912). The importance of suspension stabilizers and agitation speeds were also mentioned in earlier patents. Since1960s various theoretical studies on the molecular weight distribution in heterogeneous phase polymerization have been carried out (Frenkel, 1963; Shaltyko et al. 1964, Frenkel et al., 1964). In 1970s, the application of suspension polymerization for the production of poly(vinyl chloride) (PVC) became a commercially important process. The basic aspects of this technique were then more attended to, which involved the effect of the surfactants on the formation of adsorption layer on the surface of PVC latex (Shvarev et al., 1975), the kinetics of polymerization of VC monomers with the dispersed droplets (Popov et al., 1975), the physicochemical state of VC molecules in suspension polymerization system (Bort et al. 1975) and stereoregularity (or tacticity) of PVC chain obtained from the controlled suspension polymerization (Macoveanu et al., 1977). The study on the suspension polymerization of PVC reveals characteristics of this system that exist also in the polymerization of other vinyl monomers.

Because of the importance and wide applicability of suspension polymerization technique, numerous review articles focusing on different the fundamental aspects and the strength and weakness of the technique have been published (Arshady et al., 1983; Yuan et al. 1991; Vivaldo-Lima et al., 1997; Dowding et al., 2000a). As remarked by Yuan et al. (1991), the suspension polymerization has the advantage of easier heat and temperature control, low dispersion viscosity, low level of impurities in the product and less separation incurred. However, the disadvantages of this process include: lower polymer productivity, difficulty for attaining operable commercial continuous process, difficulty for producing uniform copolymer composition and serious polymer built on the wall of reactor, at the surface of mechanical stirrer and baffles. More recent review by Dowding et al. (2000a) for the past ten years of published literatures showed that the suspension polymerization technique gain increasing importance for the production of catalyst support, immobilized substrate, biomaterials etc in industrial scale, over the emulsion polymerization technique because it can offer larger particle sizes. Factor governing the droplets stability, the morphologies of particles for both water-in-oil and oil-in-water system are also discussed in this article. Of course, the suspension polymerization research activity remains attractive, the trend shifts towards the production of monodispersed micron-sized particles (Liang et al., 1997; Omi et al., 1999; Kim et al., 1998), preparation of hollow and porous specialty particles (Okubo et al., 1998, 2003; Kawaguchi, 2000; Kolarz, 1994), inverse suspension polymerization (Omidian et al., 2003; Dowding et al., 2000b; Stupenkova et al., 1991), and also modeling of polymerization reactor for more reliable process control and scale-up purposes (Machado et al., 1998; Lewin, 1996; Maschio et al., 1992; Saeki et al., 2002).

2.1.3 Suspension Stabilizers

As mentioned above, the majority of suspension stabilizes used are either water-soluble polymer or small inorganic particulate materials. Typical polymer stabilizers include poly(vinyl alcohol) (80~95% degree of hydrolysis), gelatin, hydroxyethylcellulose (HEC), hydrophobically modified HEC (HMHEC), (Hydroxypropyl)methylcellulose (HPMC), sodium poly(styrene sulfonate), and sodium salt of acrylic acid-acrylate ester copolymer. Amphiphilic PVA from partial hydrolysis of poly(vinyl acetate) is the most common used dispersant for suspension polymerization due to its higher interfacial activities. It consists of hydrophilic hydroxyl (OH) groups and hydrophobic hydrocarbon backbone. By adsorption onto the surface monomer droplets and growing polymer particles, the dispersed phase can be stabilized due to sharp reduction in interfacial tension between oil and aqueous phase. Under properly controlled stirring rate, the dispersed polymer particles formed can be maintained in spherical shape throughout the suspension polymerization process.

The present research employed sodium chloride (NaCl) to cooperate with PVA for improving particulate properties. Previous research work done by Cao et al. (2000) showed that the microsphere size decreased and the size distribution tended to be broader with increasing sodium chloride content in the dispersion medium (water) due to the fluctuation of surface potentials. The effect of sodium chloride added in the PVA solution had been also investigated by Yahya et al. (1996). It was observed that adding NaCl to the polymer aqueous solution increases the surface activity of the PVA chain, as the surface tension was observed to decrease drastically with increasing NaCl concentration. The behavior can be attributed to the increasing adsorption of the PVA

at the surface of the dispersed polymer particles due to raising of dielectric constant in the aqueous solution, which expel PVA molecules from the bulk phase of water, causing more molecules to go to the microspheres surface and consequently reduce the surface potential, and thus stabilize the microspheres formed throughout the progress of reaction more efficiently.

2.2 Metallization of Plastics by Means of Electroless Plating

2.2.1 General Aspect

The electroless plating is an important surface finishing technique to achieve superior chemical corrosion resistance, abrasion resistance and mechanical properties. Electroless plating is essentially an autocatalytic chemical reduction process, taking place only at the catalytic reducing sites formed on the surface of objects, which are renewed by the reducing agent in bulk of aqueous plating solution. Electroless nickel (EN) and copper platings are the most popular technique applied in semiconductor industry for imbedding conducting bump or via on PCB. Recently, the electroless plating process become favorable choice over conventional electroplating process. The uniformity of the metal deposits, with better solderability and weldability, make the electroless process viable for carried out on complex shapes substrate. In addition, the electroless deposits are found to be less porous, to exhibit higher corrosion resistance, inherent lubricity and non-galling characteristics. Most importantly, the plating can be used to deposit a conductive surface on a nonconductive object, provided that suitable surface activation process has been performed.

2.2.2 History and Current Status of Electroless Plating Technology

Electroless plating technology was originated in early 19th century, developed in mid 19th century and fully utilized industrially after 1950s. About 1819, the reduction power of hypophosphorous acid was found. Based on that, a reduction phenomenon from nickel cations to black nickel metal powder was observed by Wurtz in 1844. Thereafter, Breateau obtained the first bright metallic deposits of nickel-phosphorus alloys in 1911 (Mallory, 1990). In 1916, Roux applied for a patent for obtaining a metal deposit from a bath containing hypophosphite, ammonia and metal salts, devising the first ever complete EN bath (Roux, 1916). More sophisticated and stable plating solution comprising reducing agents, complexing agents and stabilizers are found after 1910s. In 1946, A. Brenner and G. E. Ridell (1947) announced and applied for a patent that described the proper conditions for electroless deposition, and invented the term "electroless plating".

From 1947 and 1952, Research and development at General American Transportation Company (GATC), leaded by Gutziet, produced the "Kanigen" process (Catalytic Nickel Generation), which achieved tremendous improvements in baths and deposits. The EN process Based on that, pilot plant was built at 1953, in order to study the large-scale EN process industrially. In 1958, Japan Kanigen Co. Ltd which technically tie-up with GATC was established, and the first ever large-scale EN plant was started. Concurrently, for the last 50 years, other types of EN plating baths had been studied intensively, using different types of reducing agent, eg. sodium borohydride, hydrazine, dimethylamine borane and etc. Useful technology had been also developed capable of depositing coatings on both metals and non-metals.

In Europe today, more than 90% of all electroless nickel deposits are formed from hypophosphite-based baths. All other bath types are use only in special circumstances. Also, apart from corrosion and wear protection, the contemporary application of electroless plating includes mechanical and thermal loading, electrical properties and solderability controls. The high annual rate of market expansion of 15% for electroless nickel and copper plating ate anticipated, due to the development of more superior electroless bath properties. Also, the emergence of newer application such as coating of ceramic, polymer or glass and shielding against electromagnetic and microwave radiations using the electroless processes have account for the positive growth in the industry (Riedel, 1991).

The research activities in electroless nickel and copper plating process still remain vibrant as the trend shift towards the plating process of various substrates, metallization of nano materials, EMI shielding studies of the metal-coated materials (Tzeng et al., 2001; Huang et al., 2002; Han et al., 2001, Kim et al.; 2004), studies on the mechanism of different activating solutions and a lot more on the characterization of deposition film or layer (Chen et al., 2002; Sugihara et al., 1996; Li et al., 2001; Souleimanova et al., 1999), for the improvement in morphology, corrosion resistance and mechanical properties. Electroless metal plating of non-conducting materials, such as polyimide (Esrom et al., 2000; Bhansali et al., 1995), polypyrrole (Abrantes et al., 2000, Lim et al., 2001), poly(ethylene terephthalate) (Domenech et al., 2003), poly(methyl methacrylate) films (Grigore, 2000) and etc have been reported, which have shown potential application in microelectronics packaging. Other than polymeric film, various submicron and nano-sized particulates were found feasible to be realized by means of electroless plating, such as natural pollen particles (Xu et al., 2001), fly-

ash cenospheres (Shukla et al., 2001), zirconia powder (Wen et al., 2000), mica powder (Jiang et al., 2002), polymer microspheres and nanospheres (Warshawsky et al., 1989; Wang et al., 2000; Kishimoto et al., 2000; Kaltenpoth et al., 2003), which have been claimed to be found useful as conductive fillers, EMI shielding materials, catalysts, acoustic and energy-absorbing materials and so for.

2.2.3 Chemistry of Electroless Nickel Plating

Sodium hypophosphite is a reducing agent accompanying with the development and commercialization of EN plating technology, and it still predominates the industry unless non-phosphorous Ni or Ni-boron alloy deposition is intended. This is basically due to the unique electrochemistry of hyposphite anion. Since Ni-P alloys are basically formed during the reaction, the mechanisms of EN plating involves a secondary reaction of hypophosphite to elemental phophorus. The classic electrochemical mechanism, originally proposed by Brenner and Riddell (1947), is represented as follows:

Anodic reaction:

$$H_2PO_2^- + H_2O \rightarrow H_2PO_3^- + 2H^+ + 2e^-,\ E^0 = 0.50V \qquad (2.1)$$

Cathodic reaction:

$$Ni^{2+} + + 2e^- \rightarrow Ni^0,\ E^0 = -0.25V \qquad (2.2)$$

$$2H^+ + 2e^- \rightarrow H_2,\ E^0 = 0.00V \qquad (2.3)$$

$$H_2PO_2^- + 2H^+ + e^- \rightarrow P + 2H_2O,\ E^0 = 0.50V \qquad (2.4)$$

Reaction 2.1 is the initiation step, where the electrons are formed by the reaction between water and hypophosphite. The second reaction (reaction 2.2) accounts mainly

for the deposition of nickel metal in the EN process. Reaction 2.3 is the secondary reaction explains the evolution of hydrogen which takes place and reaction 2.4 proposes that the reaction between hypophosphite and hydrogen ions results in the formation of elemental phosphorus in the coated nickel layer. A recent study on the anodic process of phosphate ion from viewpoint of electron tunnel effect has been attempted by Yin, X. and Hong, L. (2004).

2.2.4 Electroless Plating on Non-Conductive Substrates

The electroless plating of plastics or non-conductive substrate involves the surface pretreatment and activation process prior to the plating step. The purpose of this procedure is to introduce spatially distributed palladium seeds on the surface of plastic substrate. The seeds act as the initial sites to initiate the so-called self-catalysis process, in which the deposition of very tiny Ni-P alloy grains happens only at the catalytic sites on the surface of the plated item so as to build up a plating layer, but rather than happen in the plating solution. This is the most important difference between electroless plating and conventional chemical deposition of metallic fine powders in solutions. Industrially, the non-conductive substrate surface preparation process is termed as the preplate cycle. The basic components of the surface pretreatment process comprise cleaners, predips, etchants, preactivators, activators and accelerators. Each step of pretreatment process was discussed and reviewed in literatures (Kuzmik, 1990; Muller et al., 1970).

Etchants are strong oxidizing agents that eat away the plastic surface of the microspheres. The microscopic holes formed in the surface of microsphere provide the bonding sites for the deposited metal. These sites are needed for the adhesion between

polymer microsphere and metal. Commonly used etchants for styrenic plastics are chromium trioxide and sulfuric acid. The etching procedure is generally operated at 140 to 160 ^{o}C for 4 to 10 minutes.

Activators act as the catalyst to provide capability of plastic substrate to undergo electroless nickel deposition. The catalyst is commonly the mixture of palladium (II) ions and stannous ions. The classic surface activation process involved a two-step activation procedure. The first step is the adsorption of stannous ion (Sn^{2+}) onto the substrate surface from stannous chloride and hydrochloric acid solution. After rinsing with water, the substrates are immersed or stirred in palladium chloride and hydrochloric acid solution. The second step involves the reduction of palladium cations by the adsorbed stannous ions into metallic palladium, which become the catalytic site for EN deposition. The mechanism is summarized as follows:

Step 1: $Sn^{2+} \rightarrow Sn^{2+}_{ads}$ (2.5)

Step 2: $Sn^{2+}_{ads} + Pd^{2+} \rightarrow Sn^{4+} + Pd^{0}$ (2.6)

For convenience, the first and second steps were termed as sensitizing and activating step, respectively.

The contemporary catalyst system used widely for sensitizing and activating procedures is essentially the combination of two step version. The palladium chloride, stannous chloride and hydrochloride acid are mixed into a colloidal mixture on certain portions. The catalytic layer or nucleation site formed is a palladium-tin hydrosol, which is a solution of complex ions and colloidal particles. The stability depends on

the concentration of chloride and stannous ions. The activation process is depicted schematically as below. The characterization of $PdCl_2/SnCl_2$ electroless plating catalyst have been carried out intensively for better understand of the sensitizing-activating mechanisms, and also for the improvement of catalyst efficiency on different substrate-plating solution system (Meenan et al., 1994; Dressick et al., 1996, Perez-Herranz et al., 2003; Romand, 1998).

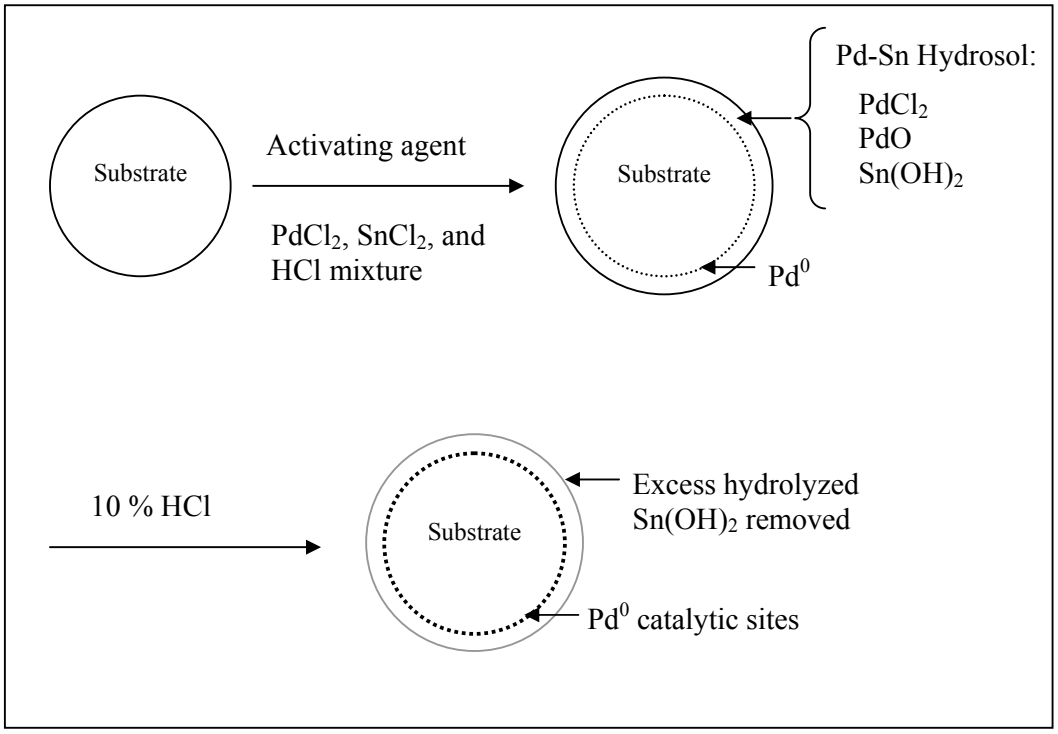

Figure 2.1 Surface pretreatment and activation mechanism for EN plating substrate

2.3 Chemical Reduction of Nickel (II) Salts by Hydrazine

Acting as a reducing agent for EN bath to offer non-phosphorous Ni plating layer, hydrazine is an important and commonly used reducing agent, and it also fits for EN of several other types of metals, such as Cu, Co and Pd. The use of hydrazine as a metal reductant can be traced back to 1940s (Pessel, 1947) and the chemistry and structure of different metal-hydrazine complexes had brought much attention after that (Athavale et al., 1967; Nicholls, 1968). Hydrazine is a powerful reducing agent in aqueous alkaline solution:

Anodic reaction:

$$N_2H_4 + 4OH^- \rightarrow N_2 + 4H_2O + 4e^-, E^0 = 1.16V \quad (2.7)$$

Cathodic reaction:

$$2Ni^{2+} + 4e^- \rightarrow 2Ni^0, E^0 = -0.25V \quad (2.8)$$

Overall reaction:

$$2Ni^{2+} + N_2H_4 + 4OH^- \rightarrow 2Ni^0 + N_2 + 4H_2O, E^0 = 0.91V \quad (2.9)$$

In this research, another attempt was to deposit nickel metal nanoparticles onto a porous styrenic-polymer substrate via in-situ deposition. Formation of nano-structural metal particles that could offer special functionality other than just high reactive surface in certain chemical environment has recently become prosperous. This is resulted from the drastic increase of the surface to volume ratio in such a way that the surface atoms predominate over framework atom to determined the nano-material properties. Metal nanoparticles are promising building block for future electronic, magnetic, optoelectric and sensing device (Feldheim et al., 2002). It is believed that by

anchoring of nickel nanoparticles onto porous polymer substrate, the composite may exert special acoustic properties.

The chemical method of the preparation of metal nanoparticles involves the reduction of metal ions in the presence of stabilizers such as surfactant, linear polymers and heterogeneous supports (Esumi et al., 1995; Leff et al., 1995; Bradley et al., 1991; Toshima et al., 1992, 1994; Brayner et al., 2000). A. Degen and J. Macek (1999) had devised the system for the preparation of submicrometer size nickel powders in non-aqueous solution of nickel salts, in which hydrazine was used as the reducing agent and ethylene glycol, ethanolamine were the dispersing medium. In more recent work, nickel ultrafine powder have been prepared by chemical reduction of aqueous solution of $NiSO_4$ and hydrazine, under high pH condition and a temperature higher than 85 ^oC (Li et al., 1999). The latter condition has been used as the benchmark of deposition of nickel particles onto our porous styrenic network. Of course, deposition of nickel particles onto heterogeneous polymeric supports by chemical reduction is relatively unexplored process. This process is feasible as nickel metal nanoparticles supported on low surface area silica, prepared by reduction of nickel acetate with hydrazine in aqueous medium had been reported recently (Boudjahem et al., 2004).

2.4 Sound and Vibration Damping Behaviors of Polymers

2.4.1 General Aspect of Sound and Vibration Damping

The studies of sound and vibration damping become dramatically important, both involve in increasing number of high-payoff applications. In military and civilian applications, the studies of sound attenuation and sound damping materials have been leading to continuous improvements on protection of human from the hazardous noise pollution. Due to the needs for structural durability, performance, stability and reduction of machine noise, vibration damping control emerges as another important field in the research realm.

Classically, materials for sound and vibration damping are mainly metal and polymers, due to their elastic and viscoelastic behavior. From two recent review articles (Chung, 2001; Buravalla et. al. 2001), the advanced materials used for the damping application involved gradient polymer materials, liquid crystal polymers, smart magnetostrictive materials, shape memory alloys and ceramic-matrix composites. The key areas for the future development is in using electro-mechanical and magneto-mechanical coupling properties to enhance damping performance. However, it appears that the utilizations of polymer remain popular and essential due to the good and tunable mechanical properties.

The studies of polymer sound damping and attenuation behaviors have drawn our attention in this research. Most importantly, the mechanisms of sound attenuation, as quoted by Jarzynski (1990, 2003), include the redirection, the scattering by inhomogeneities, and mode conversion at boundaries and intrinsic absorption by conversion mechanical energy to heat in viscoelastic materials. Direct reflection of

sound from a surface can be achieved due to impedance (of the material to the structural deformation) mismatch between the surround medium and vibrating substrate. The reflected sound waves would interfere destructively with themselves or with incident sound waves if they are out-of-phase or produces more diffuse acoustic field in backscatter direction. An obstacle or inhomogeneity in the path of sound wave propagation causes scattering if secondary sound spreads out from it in a variety of directions. The smearing of propagation directions happens when a sound beam is reflected from a rough surface and is therefore considered as scattering. The intrinsic absorption and mode conversion mechanisms will be accounted for in subsequent sections.

2.4.2 Sound and Vibration Damping with Polymers – The Intrinsic Absorption

The ability of materials to damp vibrations is exemplified by dynamic mechanical terms (Jones, 2001; Menard, 1999). Dynamic mechanical spectroscopy characterizes the storage modulus (*E'*), loss modulus (*E"*), and the loss tangent (*tan* δ) as functions of the temperature and vibration frequency of the polymer sample in question. The storage modulus (*E'*) is the quantity of energy stored through elastic behavior while the loss modulus (*E"*) is energy lost through conversion of vibration energy to heat via molecular and structural relaxations. In other words, *E"* that relies on the partial or complete deformations of polymer segments paves an important course for damping, which becomes more pronounced in the glass-transition region (Sperling, 2001). The transition marks the onset of coordinated segment motions of polymer chains accompanying with a change from stiff glassy state to soft rubbery state or vice versa, wherein the polymer exhibits the highest level of damping.

When the polymer is forced to carry out vibrating excitation, which is done either by external vibrating substrate or by incidental acoustical wave; some of macro-molecules undergo viscous deformation (flow) while others remain rigid or make response by an elastic deformation. The molecular friction, due to both types of deformations, builds up heat and brings about a decreasing amount of transmitted energy. *E'* decreases rapidly above the glass-transition temperature, whereas *E"* and the *tan* δ exhibit maximum values within a few degrees of T_g. In other words, an elastomer possesses the strongest capability for dissipating mechanical vibrations in the form of heat at the peak temperature of *E"*. Broadening the *E"* peak can apparently increase the dissipation frequency coverage. There are several measures suitable for expanding *E*" such as copolymerization, formation of interpenetrating network, partial crystallization or adsorption.

In pursuant to the about discussion, the main challenge is to find the optimum balance for *E'* and *E"*. Interpenetrating polymer networks have been invented as special matrices effective for widening the glass-transition region (Sophiea et. al., 1994; Hu et. al., 1997a, 1997b; El-Aasser et. al., 1999). The history and general aspects of IPNs have been reviewed by L. H. Sperling in numerous publications (1994, 1996 1997), which are not included here. Many IPNs exhibit a heterogeneous morphology of mico-domains in the scale of 10~20 nm, due to extensive physical crosslinking and mixing in the molecular level. Comprising essentially interphase materials, the glass transition region of IPN would become broader and span the range between the constituent polymers. The mechanical property (toughness) and vibration absorption capacity of a polymer material can be simultaneously enhanced at the macro- and micro-mechanical levels. The macro-mechanical design includes fiber-reinforced texture, foam medium,

wool silk board and etc., whereas the micro-mechanical tailoring includes modifications of polymer chain structure and matrix structure. The carbon-fibre reinforced polymer composites are most popular in sports goods, which represents the needs for achieving both excellent toughness and vibration damping capacity (Benchekchou et al., 1998; Finegan et. al., 1999, 2000; Chung, 2003). Equally important, the structural damping configurations which involved the extensional damping as well as the constrained layer damping remain popular from the viewpoint of macroscopic mechanical design. For the extensional damping, a polymer is placed as a free layer on a resonating vibrating system. For the constrained layer damping, the polymer damping layer is sandwiched in between an additional stiff material and vibrating substrate to increase the shearing action. Both the extensional and shear deformations are highly damped by intrinsic absorption due to the viscoelastic nature of the polymer material.

2.4.3 The Role of Inclusion Cavity in Damping Behaviors – The Mode Conversion

The generic manners by which a porous polymeric medium behaves to attenuate acoustic amplitude relies primarily on three factors: the rigidity of absorbent (wall), the micro-geometry (pore size distribution, tortuosity of pore channels and roughness of interfacial regions), and the viscoelastic properties of the polymer framework. As found by Sophiea et al. (1994), for improving absorption of airborne noise, the attenuation can be more a function of cell morphology rather than polymer morphology and intrinsic absorption properties. This implies that a material with a broad glass transition range could result in an enhancement to mechanical energy absorbing properties but not always an improvement to absorption of airborne noise.

The role of voids in a polymeric damping material can be explained by mode conversion mechanism. For the propagation of the longitudinal sound wave (as depicted in Figure 2.2) the motion of medium particles (e.g. air) is parallel to the direction of sound propagation. Mode conversion of longitudinal deformation to shear deformation is readily achieved at the boundaries in porous materials or the soft (air-filled) cavity in a solid. This is because over polymeric materials shear waves typically travel with very low speeds and are rapidly attenuated. To attenuate the incident sound energy, the shear deformation energy is converted to heat by molecular relaxation, most prominently happened in porous viscoelastic polymer, in which the shear modulus at inter-phase is much lower than the bulk modulus.

The cavities construction for the purpose of sound attenuation can be macroscopic and microscopic. Macrocavities augment the sound attenuation at the vicinity of pore resonance frequency itself, which act like a Helmholtz resonators (Barber, 1992; Howe, 1976; Chanaud, 1994; Dickey, 1996). At the resonant condition, the particles motion can be maximized relative to the porous structure. This, in turn, enhances the mode conversion of the incident sound. However, the macrocavities resonant frequency is unique and the attenuation mechanism is limited to low frequency range.

Sound dissipation process in microcavities is a particular example of the acoustical scattering by inhomogeneities in a host medium. The main effect of the tiny cavities in the polymer is to provide pressure release conditions at the cavity boundary. With principally the conversion of longitudinal strain to shear strain that responds to incidental sound in the first place, the subsequent dissipation process involved the "mass-spring" resonance or the viscoelastic relaxation processes, depending upon the

elasticity and rheology of the host medium. When the longitudinal wavelength is much greater than the diameter of the cavity, the scattering of sound by the cavity is brought about by a combination of radial motion and a translational motion; it is a contribution to weakening of compression strain energy. The end result is the production of secondary weaker diffuse acoustic wave after most of the energy has been converted to heat.

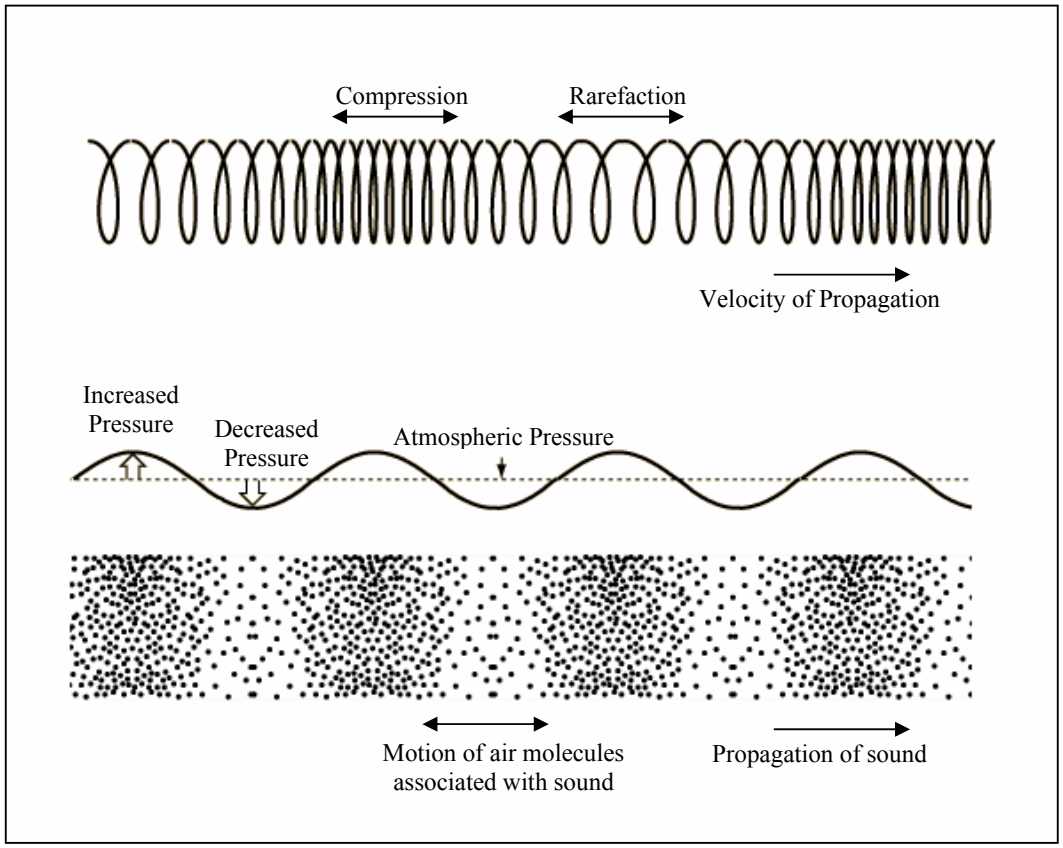

Figure 2.2 Schematic for a one-dimensional longitudinal plane wave and the pertinent mode of air borne wave transmission

From the application perspective, the porous and viscoelastic polymer packing are particularly useful in the design of coatings for broadband sound absorption layer, due to the intrinsic vibration damping behavior immediately follow the mode conversion. However, the service of elastic porous network packing is undeniably efficient, owning to the responsive dissipation process, which involves viscous flow across porous medium, friction drag of vibration air particles with respect to the polymer matrix, and also the elastic vibration response of microcavities covered a broad frequency range.

The research of porous sound attenuation material mainly involves the semi-empirical correlations of the acoustic properties of various rigid, flexible or elastic porous media. Cummings et al. (1994) correlated the bulk acoustic properties such as frequency parameter and the flow resistance coefficients of porous media to the geometry of different kinds of fully reticulated polyurethane foams. More specifically, Attenborough et al. (1995) modeled fixed thickness of soil layer as air-saturated rigid porous medium, to explore the sound field of the granular layer by accurate measurement of attenuation behavior of the medium. On the other hand, Voronina (1997, 1998) studied acoustic parameters for rigid frame porous materials (the foam constructed by gypsum, slag-concrete and ceramics) and elastic porous urethane foams, derived another empirical model which can be used to predict the acoustic impedance and sound-absorption coefficient for the porous materials. The theoretical study on the dual porosity existing in porous granular packing, for which the sound damping layer is constructed by interstitial voids and granular microcavities, was also investigated (Boutin et al., 1998). This result showed that the introduction of microporosity gave rise to an enhancement to absorption properties over a wide range

of frequencies. Hence, more advanced empirical studies of loose granular materials covered the characterization and incorporation of particle dimension, porosity, tortuosity and specific density of the grain base into the semi-empirical acoustical model (Voronina et. al., 2003). On the whole, the packing of porous polymer microsphere for the construction of sound damping panel or coating layer remains as an unexplored but exciting area for acoustical attenuation research.

2.4.4 A Brief Review on Commercial and Traditional Soundproofing Materials

This section investigates the common materials utilization of contemporary soundproofing treatment and design, to protect the human and machineries from unwanted airborne noise and structure borne noise. The former is direct acoustical wave transfer in air; the latter is the transfer of energy from vibrating surface into noise. Airborne noise can be absorbed or blocked by using sound absorbers or sound transmission barrier (commercially identifiable by the terminology "absorber" and "barrier"). The constrained layer damping treatment, viscoelastic damping composites are employed particularly for structure borne noise damping and isolation treatment. Figure 2.3 presents the generic mechanism used in particular for commercial soundproofing materials.

Table 2.1 presents the commercial soundproofing materials, produced in a few selected companies in US. In particular to sound absorbing materials, the absorption process relies on the frictional process on the surface of cells (e.g. air cavity, viscoelastic filler). The most representative materials used for the commercial purpose comprise porous open-celled foam constructed by polyester, polyurethane, melamine and polypropylene, and acoustical fiber made by polyester, natural and recycle cotton.

Table 2.1 Commercial soundproofing materials manufactured by selected companies

Company	Category	Product	Materials
Technicon Industries, Inc. http://www.tcnind.com/	Sound Absorber	Standard Acoustical Foams	Polyester Foam, Vinyl Nitrile
		Standard Acoustical Fiber	Polyester Fiber, Cotton Fiber
	Sound Transmission Barrier	Facings for barrier composite	Reinforced Aluminized Polyester Film, Urethane Film
		Acoustical Barrier	Polyether/ Polyester Foam (Closed Cell), Vinyl Barrier
	Standard Damping Materials	Viscoelastic damping, constrained layer damping materials	Asphaltic based, acrylic viscoelastic polymer
Acoustical Surfaces, Inc. http://www.acousticalsurfaces.com/	Sound Absorber	Sonex™ S.T.O.P, Sound Absorber Foam	Willtec® Melamine Foam, polyurethane foam
		Bass Buster™ Low Frequency sound absorber	Recycled cotton
		Sound Silencer™ moistureproof panel	Porous expanded polypropylene bead foam
	Noise Barrier	Soundproofing wall and ceiling panel (STOP™)	Fiberglass
		Quilted curtains (STOP™)	Willtec® Melamine, fiberglass encapsulated in aluminized scrim
		Wood specialty ceiling	Wood, mineral fiber, expanded polypropylene, perforated metal
Singer Safety Company http://www.singersafety.com/noise_control.htm	Sound Absorber	Convoluted Acoustic Foam (CAF)	Open-celled polyester foam
		Aluminized Mylar Foam (AMF)	Open-celled polyester foam with aluminized mylar facing
		Standard Acoustic Foam (SAF)	Open-celled polyester foam
	Noise Barrier	Quilted Fiberglas Wall Panels (QFM)	Vinyl coated fiberglass

		Modular Acoustic Screen	Mass-loaded vinyl barrier material, fiberglass
Blachford Inc. http://www.blachford.com/	Sound Absorber	Conasorb®	Urethane foam
	Sound Transmission Barrier	Barymat®	PVC, EVA
		Barycast®	Thermoset polyurethane elastomer
	Vibration Dampers	Antivibe® and Aquaplas®	Water-based, sprayable viscoelastic polymer, with or without steel lamination
E-A-R Specialty Composites http://www.earsc.com/	Absorbing Forms	Tufcote® acoustical absorbing foams	Clear or Aluminized polyester, black urethane
	Barriers	Tufcote® acoustical barriers	Aluminized Scrim Reinforced Vinyl, Fiberglass, Vinyl coated fiberglass
	Damping Composite	Isodamp® damping materials	Foam Layer: polyester, urethane Solid Layer: Aluminum, vinyl barrier, urethane
American Acoustical Products http://www.thomasregisterdirectory.com/tlink.html?az=2833259&hd=20256&site=noise_control	Sound Absorber	Hushcloth® Melamine Foam	Melamine form
		Hushcloth® Acoustical Foams	Polyester or Polyurethane semi reticulated foam
		Hushcloth® Perforated Vinyl Faced foams	Vinyl-reinforced Polyester or polyurethane
	Sound Transmission Barrier	Whispermat® Barrier Sheet WM0	Flexible or reinforced vinyl
		Whispermat® –WM1 Barrier with foam decoupler	Open or closed cell foam and vinyl
		Whispermat® Melamine Septum	Melamine foam coupled with vinyl barrier material
	Damping Sheet	Whisperdamp® Damping Sheet (VE, DBL, MP, 6211, Pro 200)	Mineral based mineral, asphalt impregnated paperboard, Aluminum constrained layer, Bitumen modified polymer sheet, Polymer modified bitumen sheet

The acoustical barriers prevent the sound transmission with less absorption, in which the denser material can re-radiate sound more efficiently. A rigid barrier material can transmit vibration and regenerate noise on the other side of the barrier. For outdoor noise damping purpose, a more realistic commercial design is to sandwich the absorber in between noise barriers and suitable reinforced facings, so that dual mechanism of sound absorption and re-radiation can be achieved. The commercial products used as barriers are aluminized polyester and polyurethane sheet, closed-cell polyether and polyester foam (for additional heat insulating capability), vinyl nitrile (for fire retardant capability), polyvinyl chloride, wood, fiberglass, expanded polypropylene and perforated metal.

To trace back the history of application of sound absorbing materials, which is the main interest of our research, the handbook published by National Physical Laboratory (British Standards Institution) (Evans et al., 1960) provided numerous materials properties used for sound absorption half a century ago. The representative materials were mostly natural products: asbestos, glass wool, rock wool, slag wool, wood wool, gypsum, sponge rubber, fine cinders, loose-packed granite and compressed gravel soil. The trend shifts to the domination of polyester, polyurethane and melamine synthetic plastics foams for the 21st century market (Mehta et al., 1999), with very limitation usage of expanded bead foam constructed by granular materials. The latter possesses good commercial value, as it will be demonstrated that we have one more degree of freedom to fine tune the micro- and macro porosity of the packing materials, which is important for sound damping. The assessment and modification of micromechanical properties and viscoelasticity of the individual granules (beads or microspheres) by metallization generate various potential for enhancement of sound attenuation.

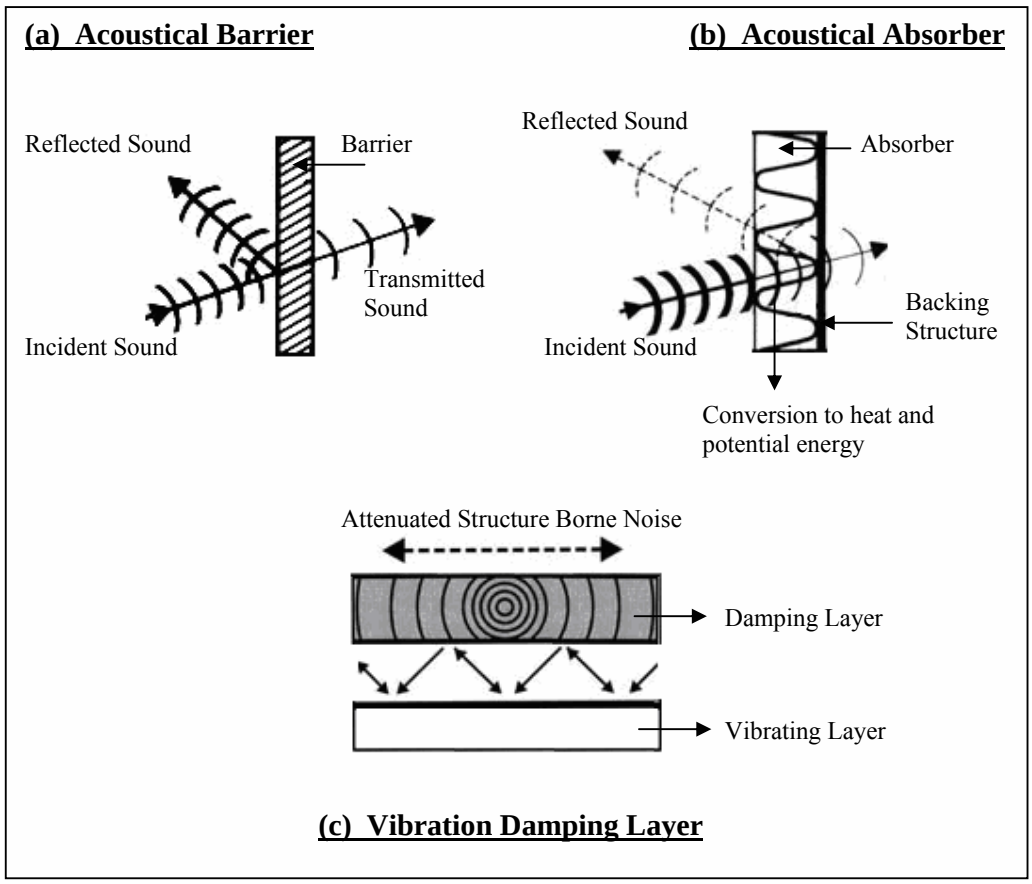

Figure 2.3 Three modes of damping and attenuation mechanisms for commercial soundproofing materials

Chapter 3

Experimental

3.1 Materials

Technical grade divinylbenzene (DVB, consisting of m-DVB 55.8%, p-DVB 24.6% and 3-, 4-ethylvinylbenzene 18.9%, Fluka), methyl acrylate (MA, 99.0%, Fluka), ethyl acrylate (EA, 99.0%, Fluka), styrene (ST, 99%, Aldrich), acrylonitrile (AN, 99%, Aldrich), 2-hydroxyethyl acrylate (HEA, 97%, Fluka) were used after removing inhibitors. Benzoyl peroxide (BPO, moistened with 25% water, Merck), 1,1'-Azobis(cyclohexanecarbonitrile) (98%, Aldrich), methanol (99.9%, Fisher Scientific), ethanol (99.8%, Merck), acetone (99.99%, Fisher Scientific), n-decane (99%, Merck), toluene (99.5%, Merck), tetrahydrofuran (99.99%, Fisher Scientific), polyvinyl alcohol (Molecular weight = 15,000 with degree of hydrolysation 86~89%, Fluka), sodium dodecyl sulfate (98%, Fluka) and Span® 80 (Fluka) were used as received without further purification. Reagents used for polymer metallization and other purposes were of the analytical grade: nickel sulfate hexahydrate (Sigma), lactic acid (85% solution in water, Aldrich), sodium phosphinate monohydrate (99%, Nacalai Tesque, Inc.), DL-malic acid (99%, Aldrich), palladium (II) chloride (anhydrous, 59% Pd, Merck), tin (II) chloride dihydrate (97%, Nacalai Tesque Inc.), sodium chloride (99.5%, Merck), hydrochloride acid (37%, Merck), sodium hydroxide (Merck), hydrazine (35% solution in water, Aldrich), nickel powder (Ni <10 μm, Merck), methylcellulose (Methocel A4M, Dow Chemical).

3.2 Synthesis and Modification of PMADVB Microspheres

3.2.1 Preparation of Poly(methylacrylate-co-divinylbenzene) Microspheres

The microspheres were synthesized by the suspension polymerization of methyl acrylate (MA) and divinylbenzene (DVB), using benzoyl peroxide (BPO) as the initiator and 0.5 wt % polyvinyl alcohol (PVA) as dispersant (Xu et al., 2000). The preparation was carried out in a three-necked round bottom flask equipped with a mechanical stirrer, a reflux condenser and a thermocouple. The mixture was stirred at fixed agitation rate (250, 600 and 700 rpm for each run), to give a suspension of oil droplets dispersed in aqueous phase, under argon gas purging. A three-ramp temperature profile (76^{o}C/3h, 85^{o}C/3h, 90^{o}C/5h) was implemented to conduct the polymerization. The resultant PMADVB powders were washed in warm water and followed by vacuum drying at 60 ^{o}C. After drying, the powders were graded using sieves. Three portions of microspheres: < 50 μm, 50~100 μm and 100~300 μm were therefore sorted out.

3.2.2 Electroless Plating on PMADVB Microspheres

The PMADVB powder of size range 50~100 μm was soaked in an alcohol solution of surfactant Span-80 (1 wt %). After filtration, the powder was activated and sensitized using a colloidal solution of palladium chloride and stannous chloride. After filtration and drying, the EN plating took place as the sensitized beads (0.5 g) were introduced into the plating solution (50 ml, Table 3.1) for a fixed duration (10 minutes) for all samples. To achieve different deposition rate, the reaction temperature was varied within the range of 40 to 80 ^{o}C. The nickel-coated beads were then washed several times in DI water after EN plating.

Table 3.1 The composition of electroless nickel plating solution formulated in house

Chemicals	Concentrations
Nickel Sulfate Hexahydrate ($NiSO_4.6H_2O$)	27 $g.l^{-1}$
Sodium Phosphinate Monohydrate ($NaH_2PO_2.H_2O$)	28 $g.l^{-1}$
Lactic Acid ($CH_3CH(OH)CO_2H$)	25 $ml.l^{-1}$
DL-Malic Acid (99%) ($HO_2CCH_2CH(OH)CO_2H$)	15 $g.l^{-1}$
pH 4.8	
Plating temperature: 40~80 ^oC	
EN bath stabilizers: Pb^{2+} ions	

3.3 Synthesis and Modification of Porous Copolymer Networks

3.3.1 Preparation of Porous Crosslinked Microspheres

Porous copolymer microspheres of styrene (ST) and divinylbenzene (DVB) (ST:DVB = 1:1 mol-mol basis) were synthesized by the suspension polymerization, using benzoyl peroxide (BPO) as the initiator and 0.5 wt % sodium dodecyl sulfate (SDS) as dispersant. The porogen or diluent, mixture of toluene and decane (1:1 or 1:3 vol/vol) were added in each synthesis, with the dilution ratio set at 0.5. The preparation was carried out in the reactor setup, as described above, with the similar heating profile and a stirring rate of 600 rpm. After polymerization, the resultant poly(styrene-co-divinylbenzene) [PSTDVB] powders were extracted with hot tetrahydrofuran in Soxhlet extractor for 24 hr. Finally, the powders were washed in warm water and followed by vacuum drying at 60 ^oC. Follow the similar procedures, poly(ST-DVB-HEA) and poly(AN-DVB) with same nominal crosslinking degree were prepared. The pertinent nomenclature, monomers and diluents composition for syntheses were summarized in Table 3.2.

Table 3.2 Compositions of the monomers feeds and the divergences between the solubility parameters of porogen and of polymer networks

Symbol	Molar ratio of monomers	Diluents v_{Dec} / v_{Tol}	δ_m ($MPa^{0.5}$) [1]	$\lvert\delta_m - \delta_p\rvert$ ($MPa^{0.5}$) [2]
SD0	ST:DVB = 1:1	-	-	-
SD11	ST:DVB = 1:1	1:1	15.85	2.75
SD31	ST:DVB = 1:1	3:1	14.68	3.92
SDH11	ST:HEA:DVB = 9:1:10	1:1	15.85	2.95
SDH31	ST:HEA:DVB = 9:1:10	3:1	14.68	4.12
AD11	AN:DVB = 1:1	1:1	15.85	10.85
AD31	AN:DVB = 1:1	3:1	14.68	12.02

For all reactions, [SDS] = 0.5wt%; Volume ratio of aqueous to organic = 10:1;
1. Solubility parameter of the porogen, $\delta_m = \delta(Dec) \times Vol(Dec)\% + \delta(Tol) \times Vol(Tol)\%$;
2. Solubility parameters of the respective polymer networks generated: $\delta_p(SD) = 18.6\ MPa^{0.5}$; $\delta_p(SDH) = 18.8\ MPa^{0.5}$; $\delta_p(AD) = 26.7\ MPa^{0.5}$

3.3.2 Metallization of Porous Copolymer Microspheres

The porous microspheres, e.g. the PSTDVB powder of size <50 μm (2 g) was soaked in methanol solution of nickel sulfate (0.5 Ni wt.% with respect to the porous substrate). This loading process was carried out for 6 hours, to ensure the proper wetting of the powder and also the thermodynamic equilibrium for the nickel ions adsorption. After slow evaporation of methanol, the dry powder was dispersed in an alkaline mixture of reducing agent and polymeric surfactant (100ml, Table 3.3). Substantial about of sodium chloride was added in order to depress the re-dissolution of nickel sulfate into continuous aqueous phase. To initiate the reduction reaction, the

reaction mixture was heated to 80 ^{o}C, for 12 hours. The nano-sized nickel-deposited beads were then washed several times in DI water, followed by acetone and dried under vacuum. Same metallization procedures were carried out, using different kinds of substrate, SD, SDH and AD series.

Table 3.3 The recipe used to reduce Ni^{2+} salt trapped inside SD beads

Chemicals	Concentrations
Sodium Hydroxide (4 M)	200 $ml.l^{-1}$
Hydrazine ($N_2H_4.H_2O$) 35%	100$ml.l^{-1}$
Polyvinyl Alcohol	5$g.l^{-1}$
Sodium Chloride	50 $g.l^{-1}$

3.3.3 Preparation of Semi-IPN Composed of Poly(ethyl acrylate) Chains and PSTDVB Network

For the incorporation of linear poly(ethyl acrylate) into the porous poly(styrene-co-divinylbenzene) matrix, the process was undertaken by two steps: monomer loading and in-situ polymerization. 5 g of microspheres (SD11 or SD31 series) were dispersed and stirred in a 50-ml solution of toluene (Tol), ethyl acrylate (EA) and Azo-bis(cyclyhexanecarbonitrile). The volume fraction of EA in the solution was varied by 10, 30 and 50 %, whereas the initiator azo compound concentration was kept as 1 mol % of EA.

After 24-hour stirring, the EA-loaded particles were dispersed in a 100-ml PVA aqueous solution and heated at 80 ^{o}C for 48 hours to lead to polymerization of EA inside the voids of PSTDVB beads. The setup is similar as described in section 3.2.1.

After polymerization, the resultant semi-IPN powders were washed in warm water and dried, followed by Soxhlet extraction with hot methanol for another 24 hours to remove un-polymerized EA. Finally, the powders were washed in warm water for several times, and were dried in vacuum at 50 ^{o}C. The reaction conditions are tabulated in Table 3.4.

Table 3.4 Compositions of the monomer feeds and the divergences between the solubility parameters of loading agent (EA+Tol) and of the SD networks

Symbol	Pore volume and mean radius of SD beads		Vol (EA) % In Tol	δ_m ($MPa^{0.5}$) [1]	$\lvert\delta_m - \delta_p\rvert$ ($MPa^{0.5}$) [2]
SD11EA10			10	18.14	0.46
SD11EA30	0.5936 (ml/g)	104 Å	30	18.02	0.58
SD11EA50			50	17.9	0.7
SD31EA50	0.7596 (ml/g)	117 Å	50	17.9	0.7

For all loading process, loading agent (EA+Tol) = 50 ml; Pristine beads = 5g; Duration = 24 hr.
For all reactions, [PVA] = 0.5wt% (100ml); Temperature: 80^{o}C/48hr; agitation rate = 500 rpm
1. $\delta_m = \delta(EA) \times Vol(EA)\% + \delta(Tol) \times Vol(Tol)\%$, where $\delta(EA) = 17.6\ MPa^{0.5}$, $\delta(Tol) = 18.2\ MPa^{0.5}$
2. Solubility parameters of the SD network: $\delta_p(SD) = 18.6\ MPa^{0.5}$

3.4 Methods of Characterization

3.4.1 Functionality, Surface Morphology and Topology Studies

Fourier transform infrared (FT-IR) spectroscopy was employed to verify the functionality of the microspheres. The spectra were obtained on a BIO-RAD FTS-135 FT-IR spectrometer. The analysis of the morphology of Ni-P coated microspheres as well as pristine PMADVB substrate was carried out on JEOL JSM-5600LV Scanning Electron Microscopy (SEM). To establish the cross-sectional view of the coated PMADVB, the microspheres were dispersed and mounted in the fast cure epoxy resin (Buchler® Epo-Kwick), followed by grinding and polishing processes to chop off part of the beads. The grinding procedure was a stepwise process, using four grades of silicon carbide grinding paper subsequently, which are FEPA (Europe) grit number P400, P600, P2500 and P4000. The work was carried out on a Metaserve® Grinder/Polisher with suitable rotating speeds. The final polishing cloth was Buehler Microcloth®, generally adept for final polishing of the ceramics or composite material items. To achieve a smooth cross-sectional surface that reveals the true microstructure, all steps from initial cutting to the final polishing were carefully maneuvered to avoid over heating and mechanical damages. Energy dispersive spectroscopy (EDS, Oxford Instruments INCA) was employed to carry out element mapping analysis on the cross-section of a coated microsphere.

For the detailed surface view of all kind of pristine porous microspheres (SD, SDH, AD), powders with nano-nickel deposition and PEA-PSTDVB, all the morphology characterization had been performed on JEOL JSM-6700 F Field Emission Scanning Electron Microscope (FE-SEM). Magnification of 10,000 to 100,000 X can be achieved.

3.4.2 Thermal Analysis

DSC analysis of both pristine PMADVB microspheres and the Ni-P plated ones were performed on a Differential Scanning Calorimeter (Mettler Toledo) instrument under dry nitrogen atmosphere. The temperature program was designed in such a way that the PMADVB powders were quenched from room temperature to -20 ^{o}C, heated up to 200 ^{o}C, cooled to -20 ^{o}C again (segment 3), and reheated to 200 ^{o}C (segment 4) at a constant rate of 10 K.min^{-1}. Each analysis used 5-6 mg of the powder sample, and the aluminum pan in which the powder was placed was gently shocked to assure the same packing density in different rounds of sample loading. The thermograms recorded were the second cooling and heating profiles (segment 3 and 4) covering a range from -20 to 100 °C.

For the scanning of porous microspheres and their nano-Ni deposited counterparts, since the glass transition range is far higher than ambient temperature, the temperature program was designed as: 25 ^{o}C~150 ^{o}C (segment 1), 150 ^{o}C~25 ^{o}C (segment 2) and 25 ^{o}C~150 ^{o}C (segment 3). The thermograms recorded were the second heating profile (segment 3) covering a range from 25 to 150 °C, to ensure similar thermal history for each sample. For the analysis of PEA-PSTDVB semi-IPN which trapped soft and linear PEA chains, the DSC analysis was done in exactly the same fashion as that described for PMADVB microspheres.

3.4.3 Determine Pore Sizes and Distribution by Mercury Intrusion Porosimetry

Pore sizes and their distribution of the porous microspheres synthesized by the suspension polymerization were determined on a mercury porosimeter (Micromeritics 9420), also obtained were the pore volume, surface area, and average pore diameter of the beads. Extra care had been taken when the porosimetry method was employed to investigate the porous properties of the tiny powders (Webb, 1997, 2001).

At lower intrusion pressure, the tiny microspheres were consolidated into a rigid mass with roughly constant packing density (for same type of powder), provided the disturbance within the penetrometer was minimized under long enough equilibration time. At the breakthrough pressure, the filling to interparticle void commenced, the interstice space registered in mercury porosimetry as pore volume. In reality, the pores within the microspheres usually are smaller than the void volume and can only be traced at high enough pressure.

Basically, the statistics done for entire intrusion range (0.5-60000 psia) provided the bulk properties of the closely packed powder. To estimate the porosity and pore sizes of individual microspheres, since the onset and endset pressure of interstitial mercury filling are arbitrary, we select an intrusion pressure ranges 500-60000 psia for the experimental data interpretation. It has been found that 500 psia is a pressure point to ensure the completion of void volume filling, whereas the intraparticle pores were effectively unfilled, evidenced by the “flat” incremental intrusion curve at the proximity of this point (see Figure 4.2.7).

3.4.4 Sound Attenuation Studies

3.4.4.1 Setup of Testing Device

The measurement of sound attenuation of the powders was performed in a cylindrical attenuation kit, made by Perspex tube (ID 6 cm, length 0.5 m), as shown in Figure 3.1. Stationary sinusoidal acoustic waves with frequencies from 100-1000 Hz and 4000-5000 Hz with fixed intensity were arranged to emit from one end of the tube and to collect by a microphone in the other end. A thin circular disk (thickness ≈ 2 mm) made of the microspheres was placed at the mid way in between the sound generator and receiver. The propagated plane waves hit the testing disk, followed by different transfer modes, including reflection, scattering, transmission and absorption as heat. The intensity of attenuated sound wave that reach the detector finally was then recorded, and extent of attenuation was expressed in terms of sound attenuation coefficient ($\alpha \cong I_{Attenuated} / I_{Incidence}$). Compared with the standard impedance tube method (ASTM C 384-98), the testing setup used in this work is a simplified one for it only measured the intensities of transmitted and attenuated sounds.

3.4.4.2 Preparation of Testing Disk

For the preparation of testing disk, the microspheres were introduced into a solution of methylcellulose (5% by weight of the powder) in water/acetone (v/v = 1:2). The resulting paste was thickened quickly by evaporating the solvent under mechanical stirring, and finally a dry powder was obtained. After that, fixed amount of the powder was pressed in a pellet-die on a Carver® hydraulic press (model #3912) to the level of 0.28 ton/cm^2 in order to maintain consistent porosities for all the testing disks.

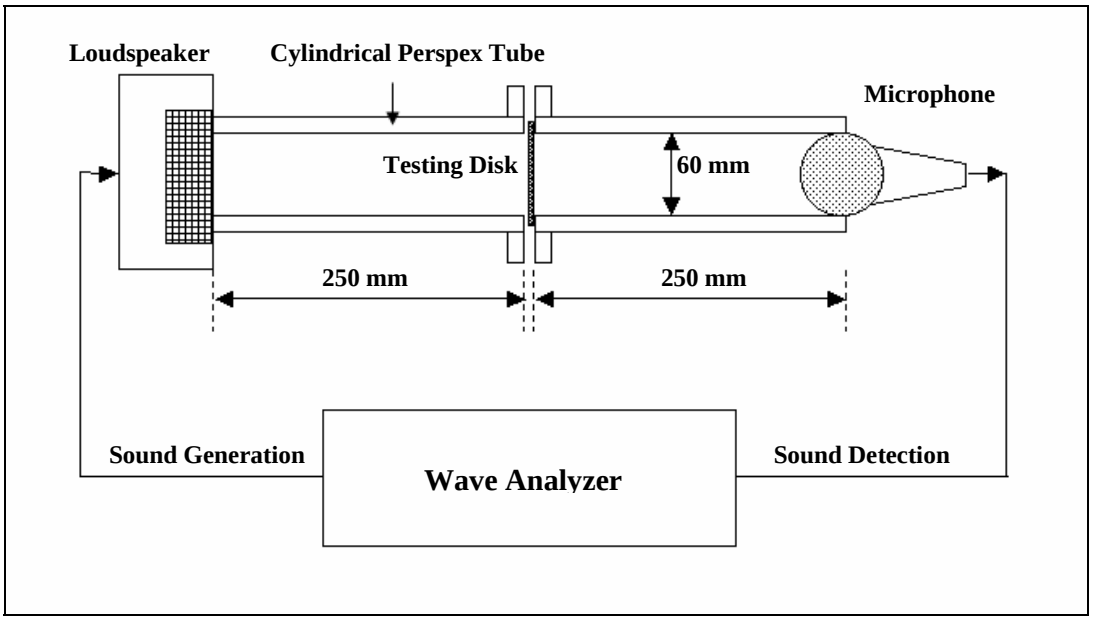

Figure 3.1 Experiment setup for acoustic wave attenuation

3.4.4.3 Sound Generation and Sound Detection

The sound generation and detection processes in this test were completely computerized. The software, TrueRTA™ Version 4.0.3 was used to generate standard sinusoidal wave of different frequency, under fixed intensity. The sound recording and analysis were performed using Sound Forge 4.5c (Build 319). In this program, the detected sound wave was recorded under a sampling rate of 44,100 Hz, and saved as a 16-bit wav file format. The Statistics tool for this program was utilized to calculate the root mean square (RMS) of the incident sound magnitude as a dB value. The dB value can readily be converted into sound intensity:

$$SL = -10\log\left(\frac{I}{I_0}\right) \quad \Rightarrow \quad I = I_0 \times 10^{-SL/10} \qquad (3.1)$$

where I_0 is the reference intensity detected by normal human ear at pressure levels as low as approximately 20μPa.

3.4.4.4 Measurement of Incident Intensity and Generation of Control Curve

The incident sound intensity is the prime parameter for calculation of sound attenuation coefficient. To measure this value under different frequency, a blank test of the sound attenuation kit had been carried out. Here, the control curve was the sound level profile (plotted as dB versus frequency) generated without the installation of testing disk in between of the sound generator and detector. As depicted in Figure 3.2 and 3.3, the control incident sound level varies with frequency even though all the hardware had been carefully monitored at constant operating condition. The local maxima of dB values appearing on the figures happens at ca 250, 400, 700 and 900 Hz, are speculated to be the resonance of the Perspex tube of the device. Resonance arises when the successive echoes reinforce the pressure on the inner face of the tube and the

surface of the testing disk. It depends on the diameter, length, density of the testing device and the outside streaming medium. At the resonance frequencies, the device acts as a horn that increases the sound intensity output of the source and thus lowers the α values for all attenuated acoustic waves. In the relatively high frequency (4000-5000 Hz) sound field, the resonance band was found at the vicinity of 4150-4250 Hz, which is less serious compared to low frequency range.

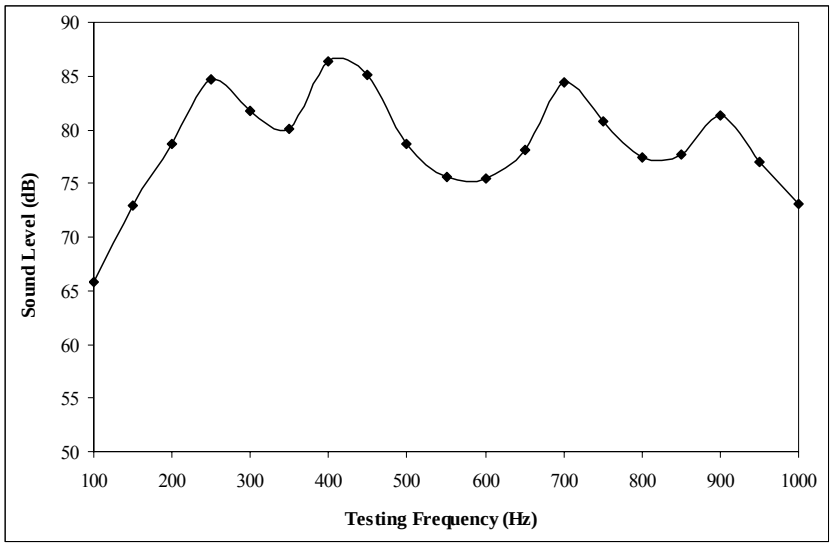

Figure 3.2 Control curve generated in the blank run for sound attenuation kit (100-1000 Hz)

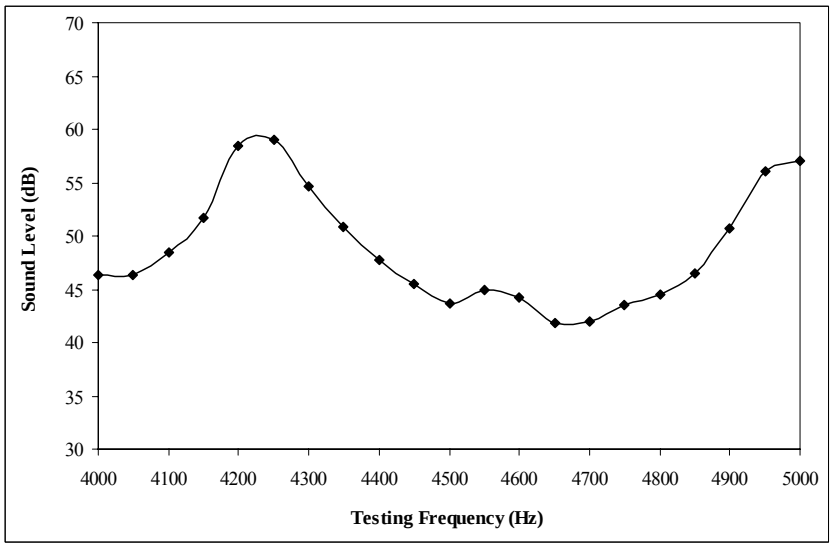

Figure 3.3 Control curve generated in the blank run for sound attenuation kit (4000-5000 Hz)

3.4.5 Ultrasound Attenuation Studies

3.4.5.1 Setup of Testing Device

To verify the ultrasonic damping capability of different types of microspheres prepared in section 3.2 and 3.3, we utilized the adsorption of copper (II) ion onto a solid biomass in aqueous medium as the probe since ultrasonic wave can strongly accelerate the adsorption rate. A special designed double-walled glass cylinder was used for this assessment, in which the polymer powder was placed in between the energy source and the probing system to attenuate the incoming ultrasonic wave (Figure 3.4). The inner tube was filled by 4 ml of 0.1 M copper sulfate solution and 0.2 g of an insoluble biomass adsorbent. The annular space between inner and outer tube was tightly packed by a given amount of uncoated or coated powders, constituting a constant-thickness damping layer (3 mm) for the adsorption chamber. This device was placed in an ultrasonic (laboratory cleaner, Geprufte Sicherheit Transsonic 460/H) chamber that holds water with a fixed depth. The operating frequency was 35 kHz with an instrument power of 300 W. The extent of ultrasound attenuation was evaluated by the adsorption of copper ions on the adsorbent. Compared with using sophisticated piezoelectric devices, this simple setup could satisfy the assessment on the relative basis though it cannot give absolute value of attenuation.

3.4.5.2 Testing Procedures

The ultrasonication treatment enhanced the adsorption of Cu^{2+} ions on the biomass. The temperature of water bath was maintained in a narrow temperature range (25~35 ^{o}C) through using an on-off ultrasonication process; 2-min cooling interval was set after 5 min of action. The whole process consisted of six ultrasonication phases. The concentrations of copper sulfate in the aqueous phase were then determined on a UV-

Visible Spectrophotometer (Shimadzu UV-3101 PC) at 800-nm wavelength, at which $Cu(H_2O)_6$ complex ion shows the maximum absorption. For calibration, the standard copper ions concentration curve has been presented (Figure 3.5). A control system was made by placing water into the chamber of the device, wherein the testing sample was packed otherwise, for generating an un-protective system.

The method for assessing the ultrasound attenuation is feasible because the ultrasonic wave accelerates remarkably the sorption of Cu^{2+} ions on biomass. Ultrasound wave can effectively remove the pore diffusion resistance and lower the liquid film resistance surrounding the surface of solid biomass adsorbent. This special action is attributed to the induced turbulence and additional convective mass transport inside the pores caused by micro-jets and pressure shocks. Any attenuation effect brought about by the polymer packing layer can thus be indirectly quantified with using the changes in the concentration of Cu^{2+} ions with sonication time.

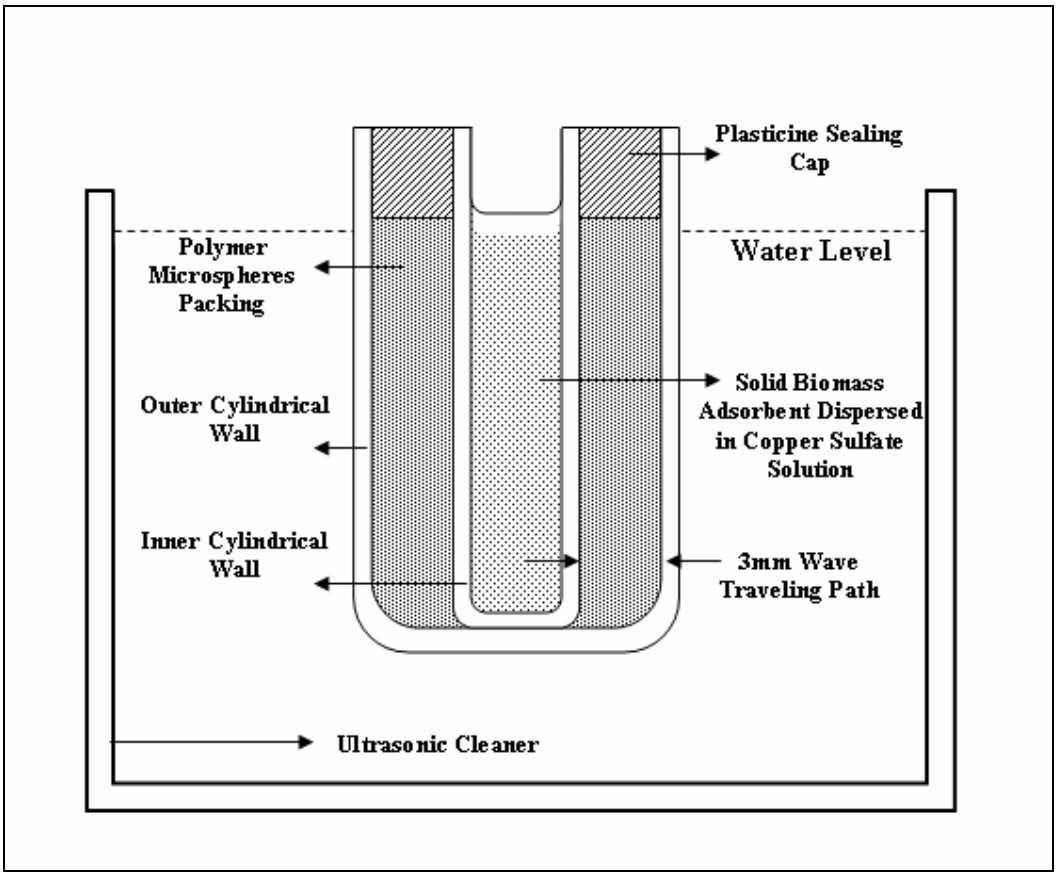

Figure 3.4 Experiment setup for ultrasound attenuation studies

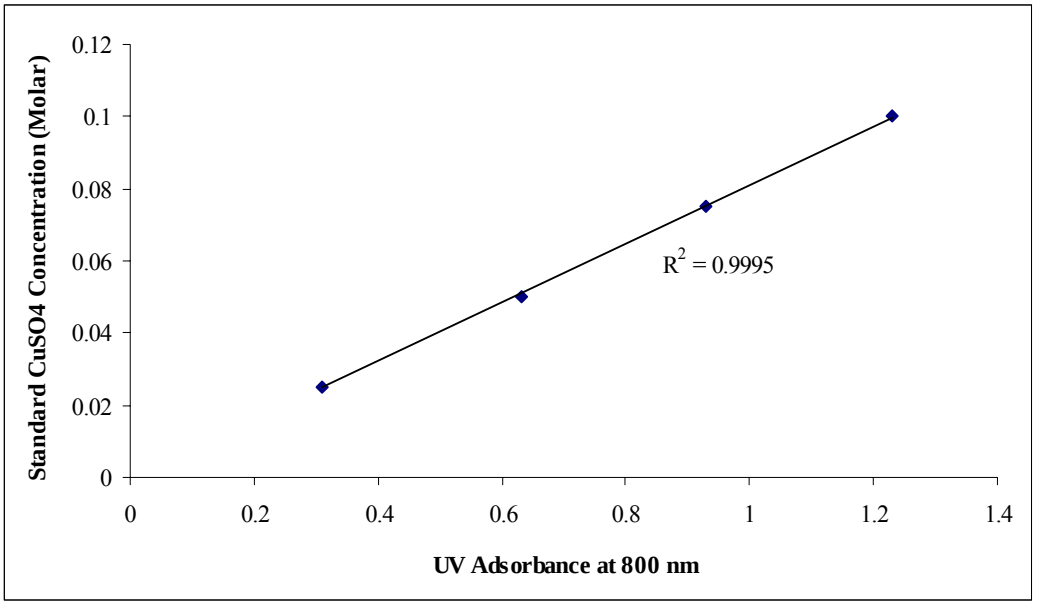

Figure 3.5 Standard $CuSO_4$ concentration calibration curve in UV-Spectrophotometry

Chapter 4

Results and Discussion

Highlight of the Absorption Materials Developed

The following investigations involve the three types of microspheres, which had been prepared and tailored for carrying out acoustic absorption test.

Type 1. Hybrid microspheres with core-shell structure, of which the core is poly(methyl acrylate-co-divinylbenzene) [PMADVB] and the shell a thin and porous Ni-P alloy shell that was deposited electrolessly (Section 4.1).

Type 2. Porous microspheres of poly(styrene-co-divinylbenzene) [PSTDVB], poly(styrene-co-2-hydroxyethyl acrylate-co-divinylbenzene) [PSTHEADVB] and poly(acrylonitrile-co-divinylbenzene) [PANDVB] on which nickel nanoparticles were implanted via chemical reduction method (Section 4.2).

Type 3. Semi-interpenetrating network composed of poly(ethyl acrylate) [PEA] chains and PSTDVB network, PEA was in-situ generated via monomer loading and polymerization (Section 4.3).

4.1 Characterization of Poly(methyl acrylate-co-divinylbenzene)

Executive Summary

In this section, the properties of pristine and Ni-P coated PMADVB were investigated. To study the effect of agitation rate on the size distribution of microspheres, we look into the PMADVB mass percentage produced by alternating stirring speed at 250, 600 and 750 rpm. The FT-IR spectroscopy for pristine sample is presented the following section for the characterization of surface functionalities. The density distribution of the beads was also accessed by swelling method. Subsequently, the surface

morphologies of the microspheres plated at different temperatures were carried out by SEM and EDX, as depicted in Section 4.1.5. The following two sections explore the relationship between thermal transition responses and sound attenuation behaviors of the microspheres, at low frequency range, 100-1000 Hz. Finally, the ultrasonic damping behaviors for pristine and selected Ni-P coated microspheres had been investigated, with the enhancement biomass-copper ions adsorption served as probing system for the extent of attenuation.

4.1.1 Size Distribution of PMADVB Produced by Suspension Polymerization

Standard sieves were used to fraction the purified PMADVB microspheres intro three different portions: i.e <50 μm, 50~100 μm and 100~300 μm. The effect of agitation speeds on the size distribution of the microspheres produced was displayed in the column diagram (Figure 4.1.1).

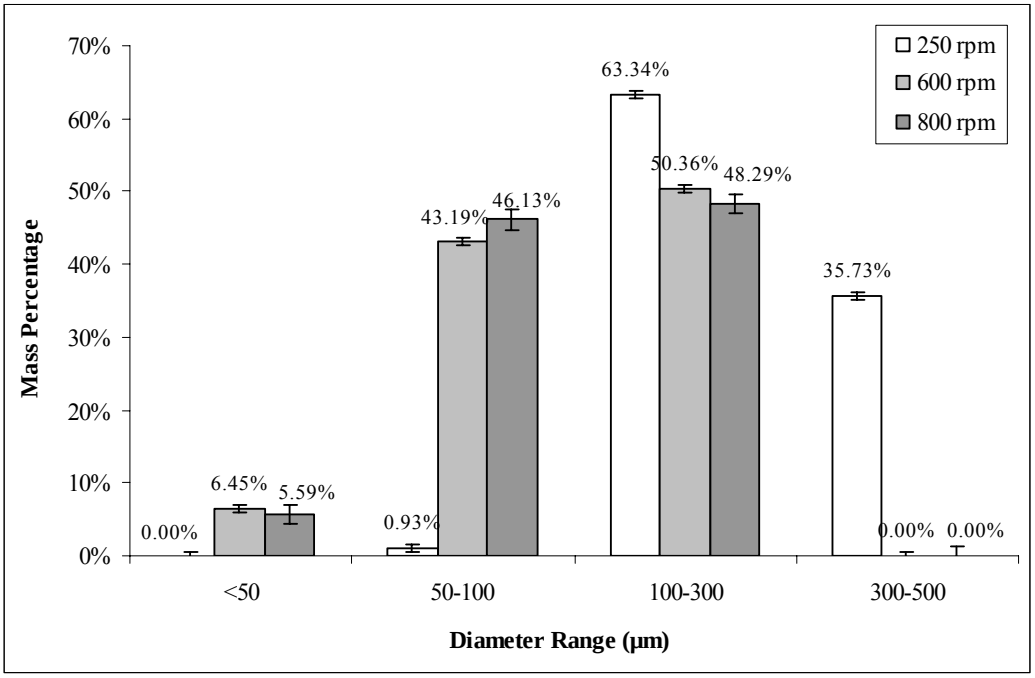

Figure 4.1.1 PMADVB microspheres size distribution under different agitation rates

In the syntheses of PMADVB microspheres, 0.5 wt % of poly(vinyl alcohol) solution was used as dispersant or suspension stabilizer. This non-ionic polymeric solution acted as a protective colloid for enhancing dispersion of monomer droplets and preventing polymer latex formed from agglomeration. PVA molecules created a steric and salvation barrier upon adsorption at the oil-water interface throughout the polymerization process (Mendizabal et al., 1992; Hashim et al., 2002; Yang et al., 2000). As noted above, the agitation rate had a direct effect to the size distribution of the formation of microspheres. To study this, three batches of samples were prepared, using exactly the same reaction conditions and suspension stabilizer system, with controlled stirring rate, 250, 600 and 750 rpm. Low agitation (250 rpm) tends to produce higher portion of bigger-sized particles due to lower shear stress imposed to the dispersed oil phase, as the coalescence phenomena was promoted. 600 and 750 rpm agitation rates display the nearly constant values of the size distribution, corresponding to the limitation of present suspension polymerization.

The 600 rpm stirring speed was found to be the optimal condition that balances the needs of minimizing coalescence and of maintaining a certain range of particle sizes; especially the shear induced coalescence was not yet become noticeable. Bound to this shear rate, three portions of microspheres sorted out by sieving procedure were: <50 μm (6.5%), 50~100 μm (43.2%) and 100~300 μm (50.4%). Further raising stirring rate could yield limited effect to promote the percentage of small-sized microspheres as long as the other conditions were fixed. This is because there is a thermodynamic equilibrium in the fluctuation of interfacial area between dispersed and continuous phases when the temperature, concentration of dispersant, and volume ratio of the two phases of the polymerization system are set up.

4.1.2 Characterization of PMADVB Microsphere by FT-IR Spectroscopy

Fourier transform infrared (FT-IR) spectroscopy was employed to study the functionality of the pristine PMADVB beads. The FT-IR analysis confirmed that the copolymer microspheres were composed of both methyl acrylate and divinylbenzene. Typical FT-IR transmittance spectrum is shown in Figure 4.1.2. The MA constituent is characterized by strong C=O stretching frequency near 1740 cm^{-1} (1750-1735 cm^{-1}), together with strong C-O stretching bands near 1200 cm^{-1} (1300-1030 cm^{-1}). Benzene ring in the DVB display different modes of vibrations, aromatic C-H stretching vibration (3100-3000 cm^{-1}), ring carbon skeletal vibration (1600-1580 cm^{-1}), C-H out-of-plane bending vibrations between strongly coupled adjacent hydrogens (900-667 cm^{-1}) and etc. Moreover, a peak at 1447.3 cm^{-1} was observed. It is due to the bending (scissoring) motion of saturated $–CH_2-$ groups.

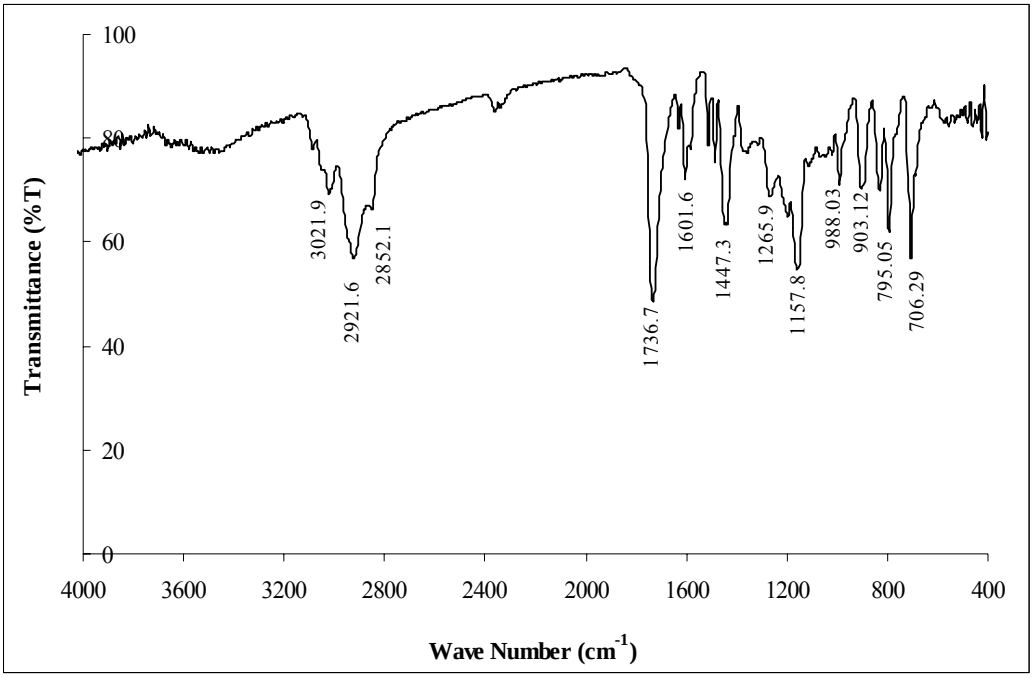

Figure 4.1.2 FT-IR spectrum of PMADVB microspheres

4.1.3 Density Distribution of PMADVB Microspheres

The density distribution inside a PMADVB bead is originally caused by different monomer reactivity ratios of the two co-monomers and will affect the viscoelastic behavior of the particle. This feature was investigated in the present work by the simple solvent swelling test (swelling % ~ t) at room temperature as the slope of the swelling extent versus time will reveal the structural information of this concern. The PMADVB beads of 50~100μm ($\bar{d}$ = 66 μm) portion and chloroform, a good solvent of the network, were used to carry out the test. The swelling ratio, $S(t)$ *%*, is defined by

$$S(t)\% = \frac{w_t - w_0}{w_0} \times 100 \qquad (4.1.1)$$

where w_t is weight of the PMADVB beads after swollen for time t, w_0 is the dry sample weight. To minimize experimental error, each $S(t)$% value was determined using a fresh PMADVB powder sample.

The PMADVB beads were prepared by the suspension polymerization method. According to the physical meaning of *Q*-*e* scheme, DVB must have a greater *Q* value and more negative *e* value than the styrene reference; DVB is therefore a more reactive monomer than styrene monomer when copolymerized with MA. As a result, the cross-linking extent (or density) in a bead should be reducing from core to shell. In order to verify this inference, the swelling test of PMADVB in chloroform was performed. The plot of swelling ratio against time (Figure 4.1.3) demonstrates a profile of progressively reduced gradients. This implies that the cross-linking extent (or density) of PMADVB network increases from shell to core, in parallel the swelling rate decreased along the radial direction.

The current swelling test method is subjected to significant experimental error when the weight of solvent uptake is measured to study the swellability of the beads. The improved method is to monitor the size increment of the beads by light scattering technique, under different swelling durations.

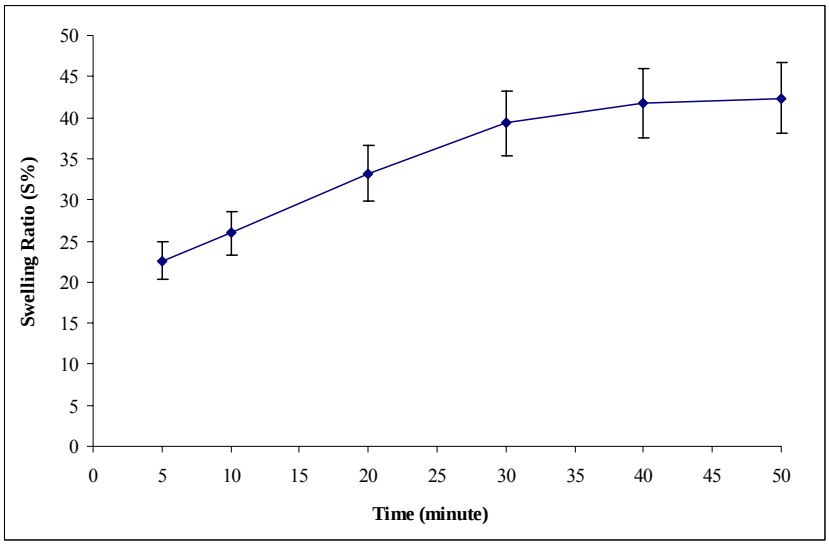

Figure 4.1.3 Swelling test for PMADVB beads

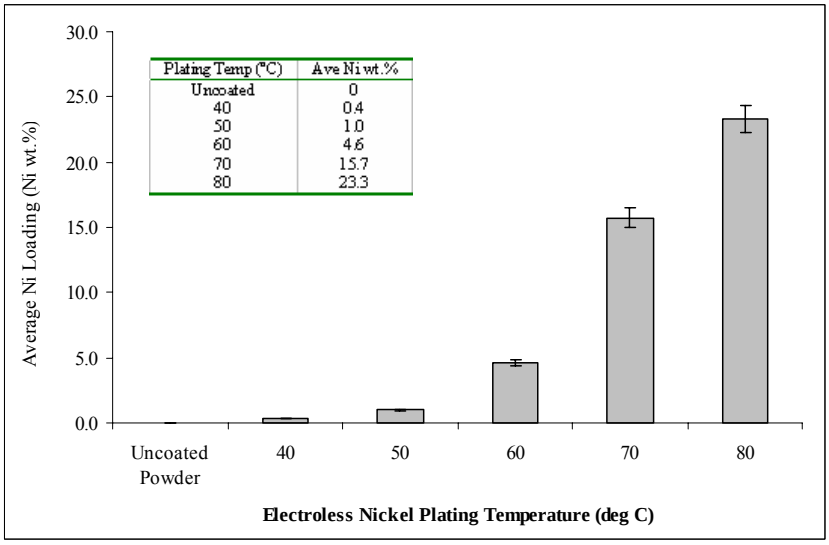

Figure 4.1.4 Nickel loading profile under different electroless plating temperatures

4.1.4 Ni-P Loading of Metallized PMADVB under Different Plating Temperature

The metal loading of electroless nickel on PMADVB substrate was varied by carrying out plating at different temperatures. The loading was defined as the mass percentage of Ni-P alloy deposited with respect to the total mass of the coated PMADVB (Figure 4.1.4). The figure was computed by the formula (4.1.2), where (M_{EN} – $M_{Pristine}$) is the weight gained after electroless plating.

$$(\text{Ni-P wt }\%) = \frac{M_{EN} - M_{Pristine}}{M_{EN}} \times 100\% \qquad (4.1.2)$$

To attain a more reliable metal loading measurement, for each electroless plating temperature, four samples were prepared (0.5 g pristine PMADVB was used each time). The metal loadings are the average value of the 4 samples, with an average error of ±4.5%. The results are tabulated against the different reaction temperatures, ranging from 40 to 80 ^{o}C, under fixed immersion time of 10 minutes. It appears that the metal deposition rate was fairly low when the plating temperature was set below 60 ^{o}C. This is due to the fact that the activation energy for autocatalytic electroless plating process will not surmounted at low temperature. Beyond 70 ^{o}C, the metal loading exceeded 10%, accompanied by more vigorous deposition of nickel. It is important to control the amount of stabilizers (heavy metal ions) added in EN bath to prevent the homogeneous reaction that triggers the random decomposition of the bath. (Mallory et al., 1990)

4.1.5 Surface Topology of PMADVB Microspheres with Different Plating Extents

Figure 4.1.5 and 4.1.6 present the SEM micrographs of pristine PMADVB and nickel-coated microspheres under different metal loadings, whose sizes still fall into the range of 50~100 μm ($\bar{d}$ = 66 μm, number-average diameter, estimated directly from the scanning electron micrograph at low magnification) after plating. Under 1000X magnification, the morphologies of elastomer microspheres remain intact and spherical before and after electroless plating**.**

Figure 4.1.6 shows more detailed changes in surface morphologies with increasing the Ni deposition extent. The surface of PMADVB sphere (Figure 4.1.6(a)) was typically flakes of interconnected micro-domains, which are distributed evenly. Figure 4.1.6(b) shows the surface of nickel deposition layer plated at 40 ^{o}C. Compare to uncoated polymer surface, this surface exhibits very similar texture and structure to the former. Low temperature plating process corresponds to very low metal deposition rate. It appears that only tiny amount of nickel metal deposited to the Pd catalytic sites on the surface. The amount of metal deposited is far from sufficient to form a metal shell on the surface; hence the topology of polymer substrate remains similar to the uncoated counterpart.

Figure 4.1.6(c) and 4.1.6(d) show the surface topology of Ni-coated layer, operating at immersion temperature of 50 and 60 ^{o}C, respectively. The surfaces reveal the presence of submicron-sized metallic grains. Denser and more uniform coatings have emerged and thus the thin metallic shell was formed to cover the spherical polymer substrate. These images indicate that the deposition was essentially a growth process of the pre-seeded palladium nuclei catalytic sites formed during the activation step which were

spread over on such a bumpy surface. Of course, higher plating temperatures (70 and 80 ^{o}C) resulted in clear agglomeration of submicon-grains, which were in general, larger, more porous and less uniform metallic grains. There are also tiny needle-like spikes protruding around the grain boundaries. This is likely to be related to the gas release kinetics involved in the plating process. (Wen et al., 2000)

$$H_2PO_2^- + H_2O \rightarrow H_2PO_3^- + 2H^+ + 2e^- \quad (4.1.3)$$

$$Ni^{2+} + 2e^- \rightarrow Ni^0 \quad (4.1.4)$$

$$2H^+ + 2e^- \rightarrow H_2\uparrow \quad (4.1.5)$$

Accompanying with the reduction of nickel, hydrogen gas was released during the plating, and in turn, would disturb the formation and deposition of nickel particles on the polymer substrate. A higher temperature led to a more rapid release of the hydrogen gas. As a result, the coating would be porous, and the metal grains would grow outwards along the paths of the released gas from the surface of the polymer substrate, forming thin plate-like or needle-shaped particles. On the other hand, when the plating was carried out at a relatively low temperature, the gas release rate was low, so that there was enough time for the gas to be released in the form of small isolated bubbles. Hence there was no pressure build-up, the lateral growth of the newly formed nickel particles was not inhibited, and a denser coating consisting of spherical nickel particles was formed.

Also, for these two categories, the cross-sectional views reveal a continuous ring structure of 1~2 μm thickness, which is essentially a grainy alloy layer, rather than a thin metallic dense film (Figure 4.1.7(a)-(d)). EDS elemental mapping of the cross

section justified that the metallic ring was formed primarily by nickel and phosphorus elements (Figure 4.1.7(e)-(f)).

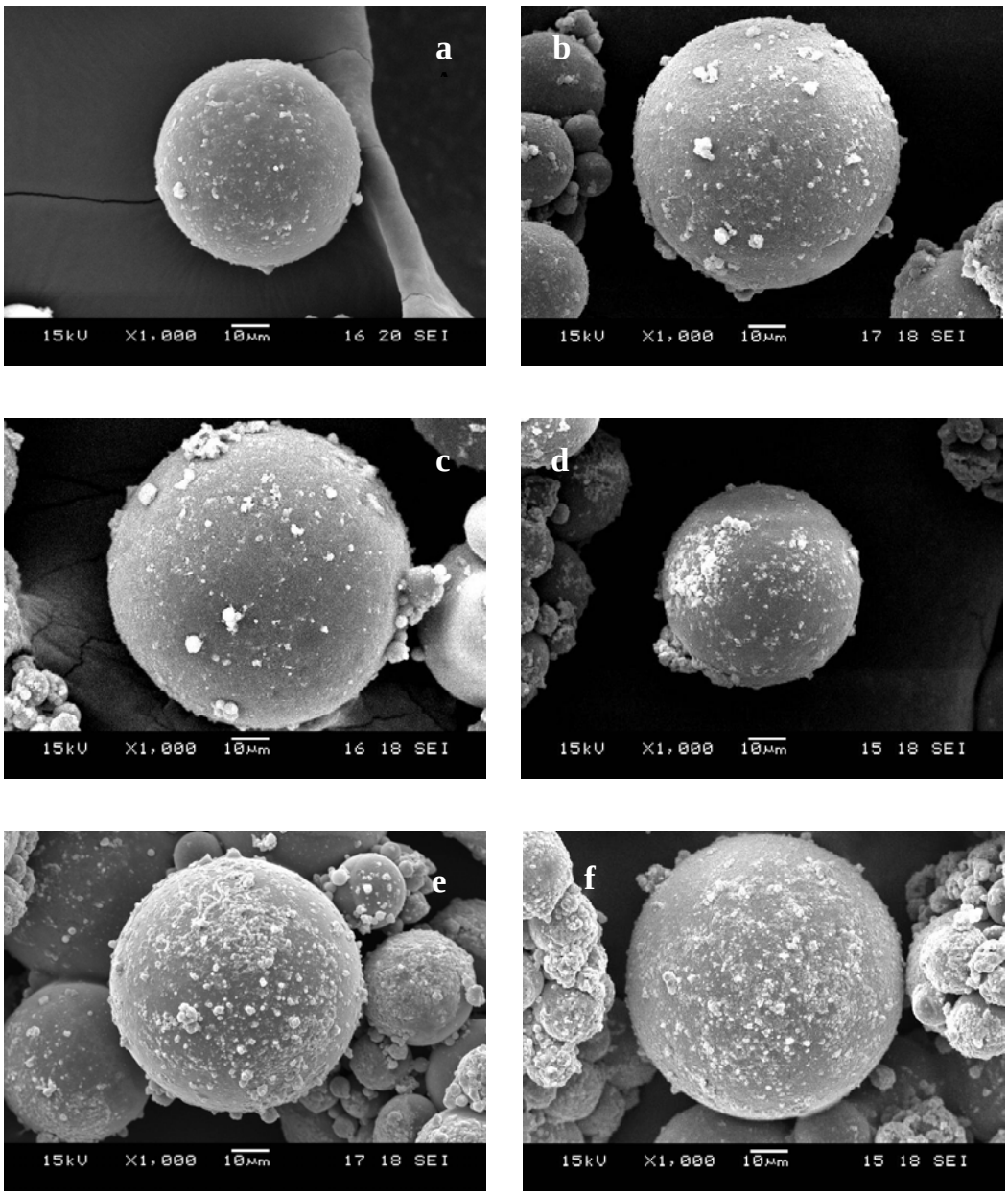

Figure 4.1.5 SEM micrographs of uncoated (a) and Ni-P coated (b-f) microspheres (50~100 μm) at 1000X magnification

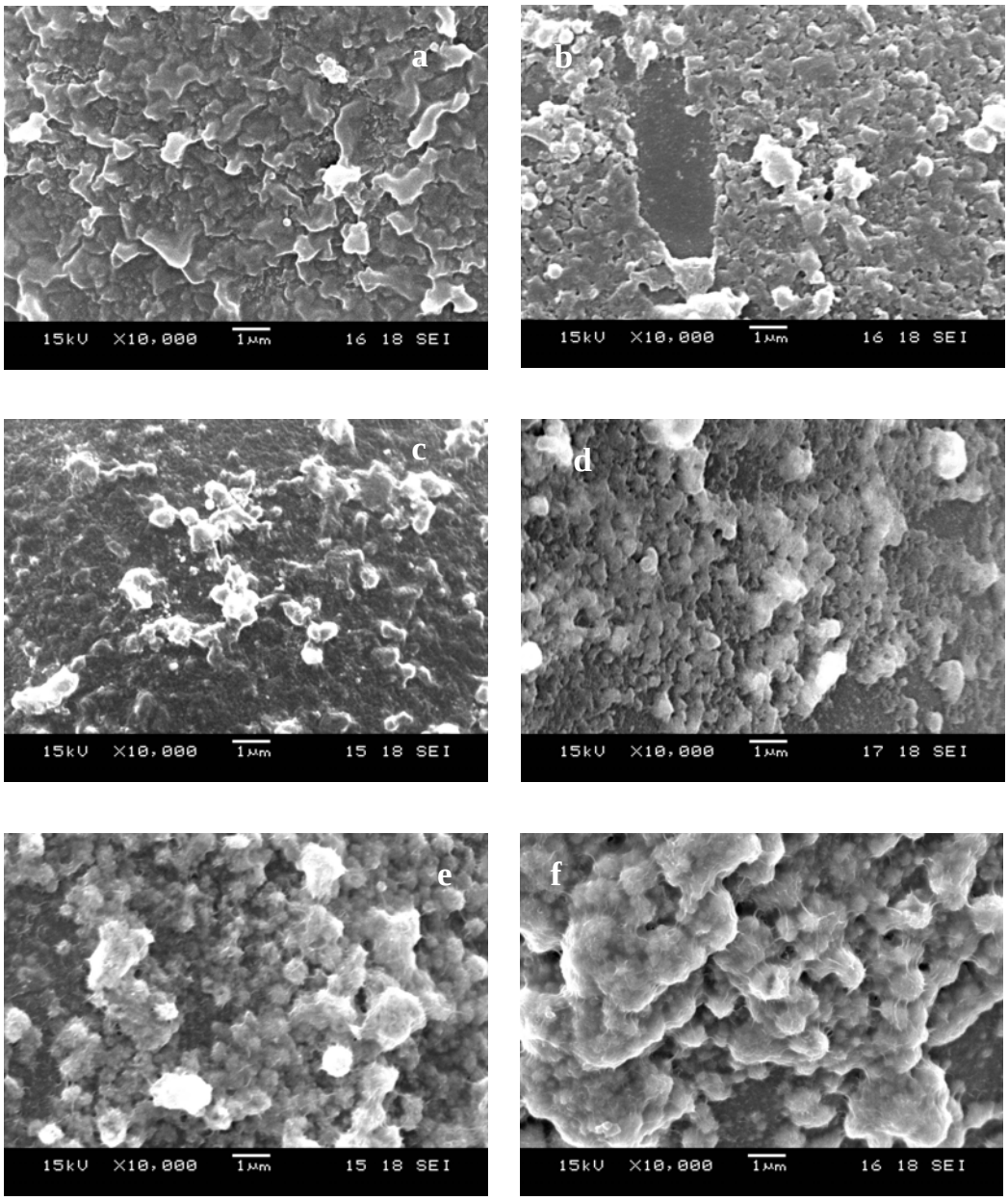

Figure 4.1.6 SEM micrographs of the surfaces of (a) uncoated, (b-d) lightly to moderately Ni-coated, and (e-f) heavy Ni-coated PMADVB microspheres at 10000X magnification

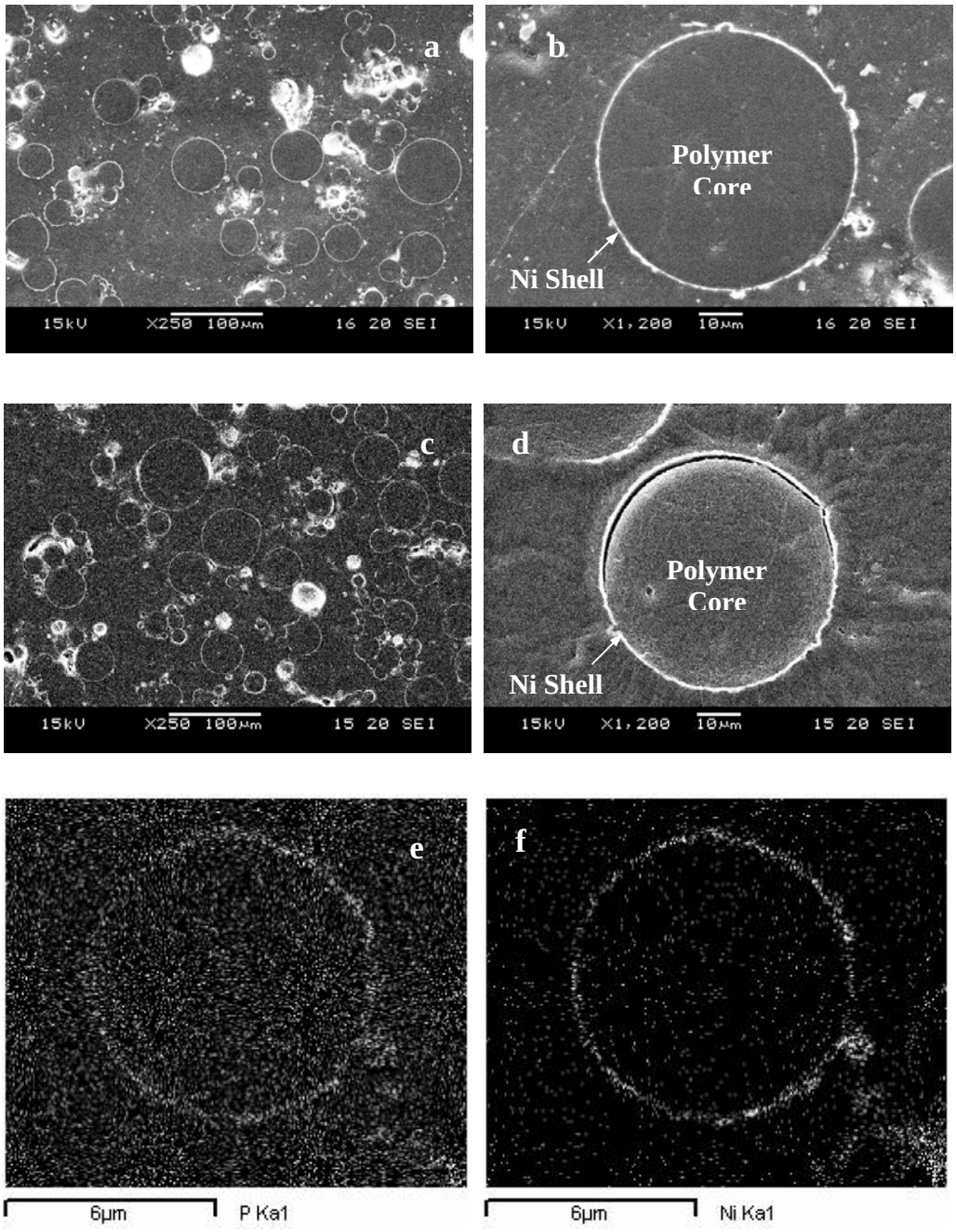

Figure 4.1.7 SEM cross-sectional views of the Ni-P coated PMADVB (a-b) 15.7% and (c-d) 23.3%. (e-f) are the EDS element mapping of (c-d).

4.1.6 Influence of Ni-P Layer on Glass Transition of PMADVB Network

The DSC profiles of the four types of the Ni-P coated powders with different metal loadings are compared in Figure 4.1.8. The measurement condition was strictly controlled to maintain them in parallel as detailed in experimental section. The most precise determination of the glass transition temperature has to be done by locating the temperature of half-freezing through cooling down an equilibrium melt (or rubbery state) at a specified rate (Wunderlich, 1997). This approach is especially adept at detecting the thermal effect of the Ni-P shell since changes in heat dissipation course can be more easily sensed than changes in heat absorption course in the temperature range under investigation. Different cooling segments (segment 3) differentiated by the width of glass transition range were observed. In addition, the measurement of the second reheating profile (segment 4) was also conducted (Figure 4.1.9) for comparison with the cooling profile.

Comparing the cooling and heating curves of an identical sample in Figure 4.1.8 and 4.1.9, the former is often more obvious as to the nature of the heat transport phenomena observed. In contrast to their uncoated counterpart, the plated powders demonstrate greater specific heat changes ($\Delta C_P = C_{P-rub} - C_{P-gla}$) and broader glass transition range with increasing Ni-P contents. It may note that the specific heat of nickel shell ($C_P \approx 0.1 cal/gK$) does not undergo any change within the temperature range of study. Figure 4.1.9 also displayed a similar trend about the change in ΔC_P with increasing the metal content as observed in the cooling profile (Figure 4.1.8), nevertheless, the breadth of glass transition range in the heating profile cannot be related with the Ni-P percentage. This irregularity is seemingly due to the hysteresis or enthalpy relaxation behavior originated from the random nature of the chain

entanglements in the matrix of PMADVB beads at the cold state. The other possible reason is related to a sludgy starting of segment motions at the polymer-metal interface. In summary, the cooling curve suits better the investigation of how metallization affects the thermal response of PMADVB network over its glass transition range.

Further inspecting the DSC analytical results, one can see the three characteristic temperatures of a glass transition process labeled in Figure 4.1.8, of which T_o is the onset of glass transition (onset of a gradual changes of slope with respect to the base line); T_e is the ease point of glass transition and T_g is the temperature at which the sample has gained half of the heat capacity of rubbery state. These three temperature points of the samples are summarized in Table 4.1.1. The data revealed that T_o decreased a bit and T_e increased clearly with increasing the metal loading. This phenomenon could be interpreted as the happening that Ni-P metal deposition layer allows to establish a near spherical temperature field inside each polymer sphere. As a result, changes in temperature will be passed on to the polymer matrix symmetrically along radial direction. A concert segment motions then becomes possible in response to the variation of temperature. In other words, in a relatively low cross-linked polymer network, heavy physical entanglements and physical cross-linking among different segments are inevitable. Hence a spherical temperature filed is important to coordinate different segment motions in the polymer matrix in response to the change of temperature.

The ending value T_e corresponds to the ease of glass transition and the emergence of rubbery plateau. The deposition of a relatively thick nickel layer would constraint expansion of the enclosed polymer matrix upon heating, which is to lift up to a certain

extent the overall segment motion energy barrier due to a swarming environment or a reduction in the fraction of free volume. This phenomenon was obvious in the sample with the highest Ni-P coating (row 6 in Table 4.1.1); there is a larger climb in both T_g and ΔC_p between row 6 and row 5 in comparison with the differences between other neighboring samples. However, such impact on polymer thermal behaviors caused by compression stress did not happened in the initial three Ni-P coated samples (row 2 to 4) as they gave almost the same T_g. A pertinent explanation for it is that Ni-P deposition had yet formed a continuous shell in these three samples. In the second high Ni-P coated sample (row 5), both the spherical temperature field effect (rising of T_e) and the Ni-P shell confinement effect (increase of T_g) coexisted, but the impact of the latter effect was not as significant as the former one for ΔC_p did not rise.

Table 4.1.1 DSC results for the pristine and the coated PMADVB microspheres with different Ni-P loadings

No	Ni-P wt %	T_o (^oC)	T_g (^oC)	T_e (^oC)	T_g Width (^oC)	ΔCp ($J.g^{-1}.K^{-1}$)
1	0.0	1.5	23	47.5	46	0.09
2	0.4	1.5	24	48	46.5	0.09
3	1.0	1.5	24	47	45.5	0.09
4	4.6	1	24.5	45	44	0.10
5	15.7	-1	27.5	48	49	0.10
6	23.3	-1	34	53	54	0.12

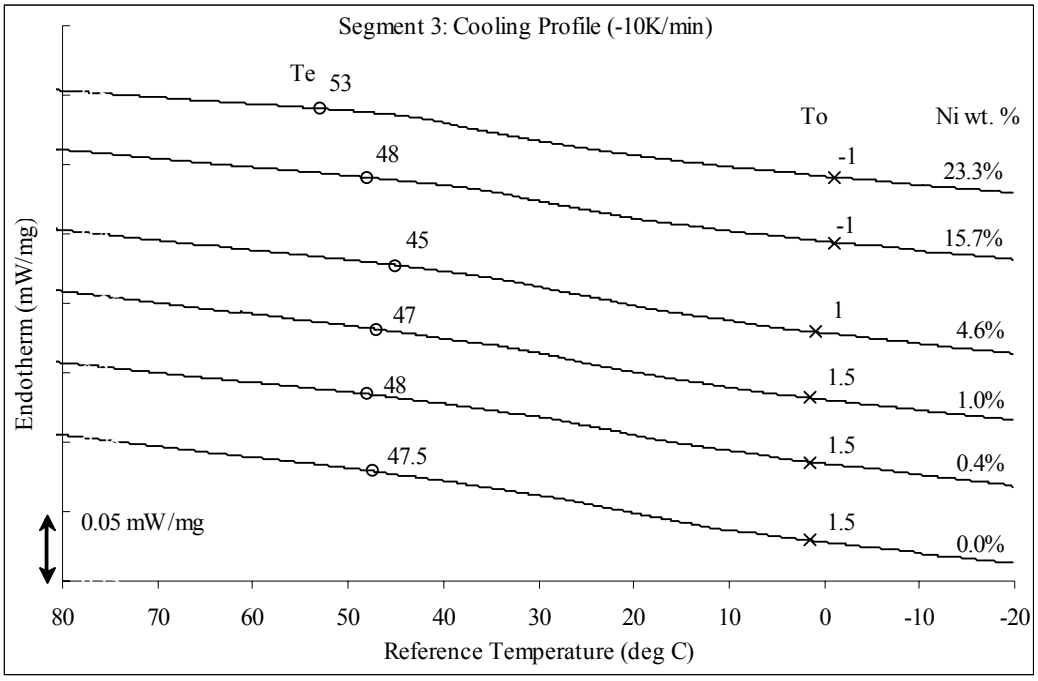

Figure 4.1.8 DSC thermograms of pristine and coated PMADVB under different metal loadings (Segment 3: Cooling Profiles)

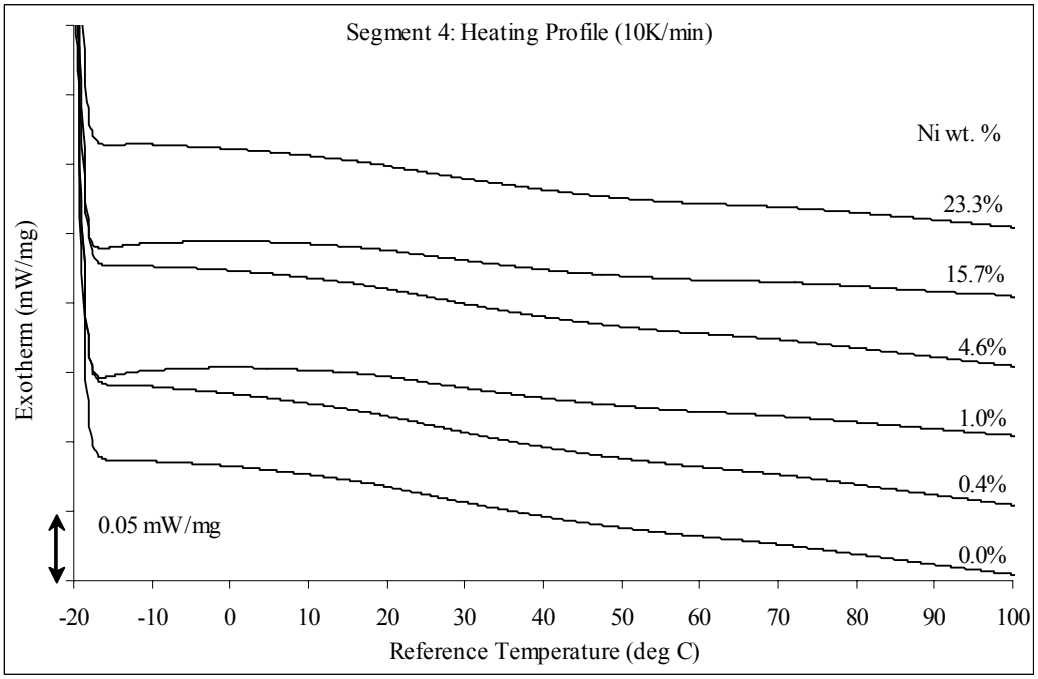

Figure 4.1.9 DSC thermograms of pristine and coated PMADVB under different metal loadings (Segment 4: Reheating Profiles)

4.1.7 Sound Wave Attenuation

The sound attenuation performances of the samples listed in Table 4.1.1 can be best represented by the pristine PMADVB powder and the two coated ones, which have the Ni-P loading of 15.7% and 23.3%, respectively. These two metal loadings are of particular interest as they show a more significant broadening effect of T_g range, as compared with the lower loading cases. The pristine PMADVB demonstrates a clear damping effect, evidenced in Figure 4.1.10, where the output sound level for each test is plotted against the testing frequency. Also, its α values exceed 0.4 over the most testing frequencies (Figure 4.1.11). As remarked by Jarzynski (1990), the sound attenuation includes scattering by in-homogeneities, mode conversion at boundaries, redirection and intrinsic absorption by conversion to heat in a viscoelastic material. Therefore, it is believed that the damping capability of the pristine PMADVB microspheres is related to the deformation and relaxation of the polymer matrix since the testing temperature falls in the middle of the glass transition range of PMADVB. The lowest α value appearing on Figure 4.1.11 happens at ca. 750 Hz, which is speculated to be the resonance of the Perspex tube of the device. Another resonance frequency band shows up at 350-400 Hz. Resonance arises when the successive echoes reinforce the pressure on the inner face of the tube and the surface of the testing disk. At the resonance frequencies, the device acts as a horn that increases the sound intensity output of the source and thus lowers the α values for all attenuated acoustic waves.

In comparison, the two Ni-P alloy coated samples show clear improvements in acoustic wave damping within the testing frequency range, especially at the resonance frequencies. This effect can be linked with the expansion of the glass transition range

of PMADVB network, which allows the network to more easily convert the acoustic vibrations into heat. To verify whether the spherical Ni-P shell is crucial to sound attenuation, a reference sample was prepared by using a mixture containing 15.7 wt % of Ni powder (with mean particle size <5 μm) and PMADVB powder. It turned out that this reference sample has a poorer capacity of attenuation as compared with the coated counterpart with the same metal content. This observation supports the essential of the spherical shell to the change of viscoelastic behavior of the PMADVB core.

The rough Ni deposition layer is deemed to play a role in scattering and redirecting the incident sound waves, which was accompanied by the intrinsic damping in viscoelastic PMADVB network. It has been aforementioned that the Ni shell comprises randomly assembled submicron-sized metallic grains, it is also likely that the incident sound was converted to a lot of smaller sound wave propagating fields, wherein destructive interference acted accordingly to assist damping the sound energy.

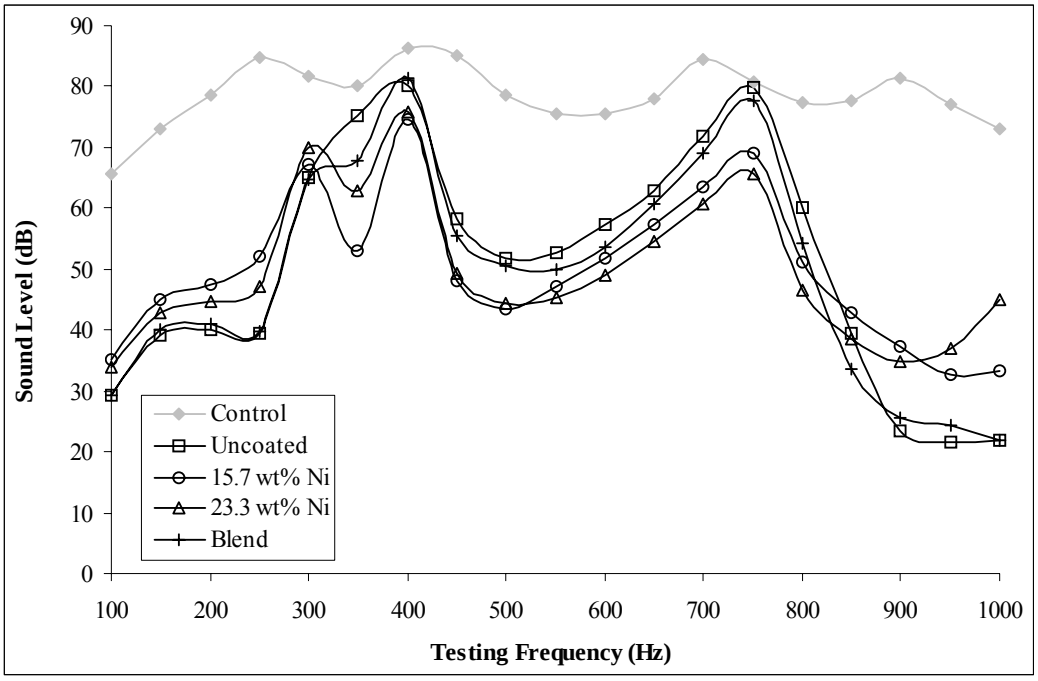

Figure 4.1.10 Acoustic attenuation behaviors of pristine and coated PMADVB under frequency range 100-1000 Hz (Reference test: Conducted using a mixture of PMADVB and 15.7% Ni powder), Sound Level vs. Frequency

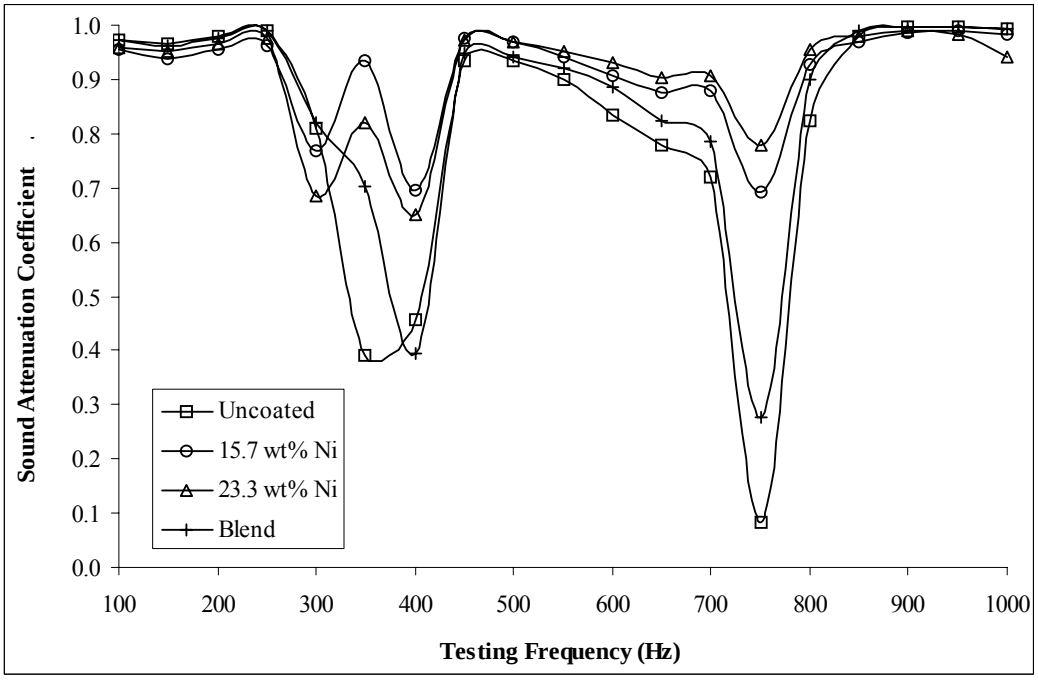

Figure 4.1.11 Acoustic attenuation behaviors of pristine and coated PMADVB under frequency range 100-1000 Hz (Reference test: Conducted using a mixture of PMADVB and 15.7% Ni powder), Sound Attenuation Coefficient vs. Frequency

4.1.8 Ultrasonic Wave Attenuation

Ultrasonic treatment enhances the copper ions removal by accelerating the molecular transport towards and from the adsorbent surface and by increasing the regeneration of exhausted absorbents. To promote adsorption of copper ions, ultrasound decreases the pore diffusion resistance of the biomass adsorbent and lowers the liquid film resistance surrounding the solid surface. The higher the incident ultrasound intensity will be the greater the extent of enhancement in mass transport of the copper ions towards the biomass surface and across the pores. This behavior can be attributed to the induced turbulence and additional convective mass transport inside the pores caused by micro-jets and pressure shocks (Bathen, 2003). The influence of ultrasound with higher intensity is greater, which indicates depletion of the liquid film thickness around the adsorbent surface, and also a better penetration of the ultrasound into the pores.

Ultrasound also promotes the desorption of adsorbed molecules, i.e. the adsorbed copper species other than $Cu(H_2O)_6^{2+}$ ions. The rate enhancement was due to an increase in diffusive transport within the pores caused by acoustic vortex microstreaming. The activation energy for desorption decreased with an increase in ultrasonic power density, thus making the ultrasound weaken the adsorption bond. The generation of "hot spots" due to cavitation and acoustic microstreaming in the pores seemed to enable the rupture of the strong sorbate-surface bonds (Rege et al., 1998) and improve desorption rates when an ultrasonic filed was applied. Desorption, which is an endothermic process, is promoted if such a bubble collapse occurs in the vicinity of the adsorbent surface wherefore adsorbed molecules at this spot go into solution. After such a cavitation event the active places for adsorption are available again. Adsorbate molecules of the solution are taken up by the adsorbent again until

equilibrium is reached. Consequently, molecules keep going into solution at some places, whereas in other areas molecules adsorb onto the adsorbent surface. In the mean time less active places for adsorption are occupied under ultrasonication, hence shifting the global adsorption isotherm towards lower surface concentrations of adsorbate.

Pore-diffusion resistance was probably more dominant than surface reaction for desorption without ultrasound. With regard to the adsorption-desorption kinetics of the biomass adsorbent under ultrasonic field, surface kinetics seemed to play a more significant role than pore diffusion (Rege et al.; 1998; Breitbach et al., 2001). For simplicity, the rate of adsorption or the rate of removal of copper ions was modeled as a first-order rate law:

$$-\frac{dC}{dt} = k_s C \qquad (4.1.6)$$

Upon integration gives

$$\ln\left(\frac{C}{C_0}\right) = -k_s t \qquad (4.1.7)$$

where C = concentration of adsorbate (copper ions) at time t, k_s = overall surface reaction rate constant, C_0 = initial concentration of the copper(II) ion.

For a fixed ultrasonication time, the value of k_s under different damping conditions can be calculated if the concentrations of copper ion in the aqueous phase after ultrasonication are known. Table 4.1.2 tabulates the Cu^{2+} concentrations left in different damping systems after ultrasound treatment. Applying the assumption of surface diffusion-controlled adsorption, we attempt to establish a direct relationship between the adsorption rate constant and the ultrasound intensity. The sound wave or

acoustic intensity, I, is defined as the acoustic energy transported per unit area and time ($W.m^{-2}$) in the direction of propagation. For a plane traveling wave in a medium with density ρ and phase velocity c (Smith et al., 1996),

$$I = \frac{P^2}{\rho c} \tag{4.1.8}$$

Both the total sound level, and the attenuation of sound, is often expressed in a dimensionless unit, the decibel, where the sound level (SL) in decibels is,

$$SL = -10\log\left(\frac{I}{I_0}\right) = -10\log\left(\frac{P^2}{P_0^2}\right) = -20\log\left(\frac{P}{P_0}\right) \tag{4.1.9}$$

where P is the sound pressure at the observation point. P_0 in the present adsorption system is defined as the total incidence sound pressure when there was no damping layer implemented.

Furthermore, as far as the relationship between k_s and the intensity of incidence ultrasonic wave is concerned, though the intensity of ultrasonic wave could be related to pressure level of instantaneous air cavities formed in the aqueous solution, the cavitations pressures should not have a simple linear relation with the surface diffusion rate. This is because several forms of energies are released when an air cavity breaks up, and the ways how the energies are utilized to enhance the adsorption of Cu^{2+} ions on the biomass are also complicated. Therefore it would be appropriate to link the diffusion rate k_s with the acoustic intensity by the power-law as the powder term n can depict the net effect from balancing various impacts on the diffusion.

$$k_s = \frac{-\ln(C/C_0)}{t} = KI^n \tag{4.1.10}$$

$$I = (K^{-1/n}) \times (k_s)^{1/n} \tag{4.1.11}$$

$$SL = -10\log\left(\frac{I}{I_0}\right) = -10\log\left(\frac{(K^{-1/n})\times(k_s)^{1/n}}{(K^{-1/n})\times(k_{s0})^{1/n}}\right) = -10\log\left(\frac{k_s}{k_{s0}}\right)^{1/n} \qquad (4.1.12)$$

$$SL\times n = -10\log\left(\frac{\ln(C/C_0)}{\ln(C^*/C_0)}\right) \qquad (4.1.13)$$

where C^* is the concentration obtained from the control cell. The damping performances and capabilities for each type of sample can be ranked in terms of relative sound level attenuated (SL) and surface reaction rate constant (k_s) after the fixed intervals of sonication. These data are presented in Table 4.1.2. The control cell was employed to benchmark the sound attenuation efficiency of the different polymer packing layers.

Table 4.1.2 The results of copper ions adsorption and estimated sound level attenuation efficiency modeled under surface reaction controlled kinetics

No	Ni wt. %	$[Cu(H_2O)_6^{2+}]$ (M)	$k_s \times 10^4$	SL×n (decibel,dB)
1	0.0 (Control)	0.04388	4.5766	0.0000
2	0.0 (Uncoated)	0.07966	1.2636	5.5894
3	15.7	0.09316	0.3936	10.6553
4	23.3	0.09032	0.5654	9.0816
5	15.7 (Ref Test)	0.07528	1.5778	4.6250

Ultrasound attenuation is defined as the decrease in intensity of the acoustic wave as it propagates from the source (ultrasonic cleaner bath) to the receiver (biomass adsorbent). The packing of the uncoated PMADVB demonstrated very clear damping effect in comparison with the control cell. Although the absolute ultrasound level entering into the aqueous suspension could not be computed in the present system, the $SL \times n$, a relative value, is adequate for differentiating the damping efficiency of different testing samples. The ultrasound damping capability of the pristine PMADVB microspheres is similar to the mechanism described above for the low frequency acoustic attenuation. Also, the Ni-P coated PMADVB microspheres exhibited improvement in ultrasonic wave damping, as shown in the Figure 4.1.13. Equivalently, the estimated k_s value based on the kinetic model was found to decrease with increasing attenuation efficiency (Figure 4.1.12). The relative attenuation of sound ($SL \times n$) increased for the nickel loadings of 15.7 and 23.3 %. The facilitation of damping and attenuation due to the Ni-P coatings has been discussed in previous section. A similar reference test was also conducted by using a mixture containing 15.7% of Ni powder (with mean particle size <5 μm) and PMADVB powder as the damping medium. Clearly, this reference sample showed a poorer damping capacity than the coated counterpart, which is consistent with the sound attenuation test result.

The Ni-P coated PMADVB powder, with the Ni loading of 15.7%, displayed the optimal ultrasound attenuation result. Increasing the metal loading to 23.3% appears to be detrimental to ultrasonic attenuation, although its metallic layer was porous and the glass transition range the widest (54 ^{o}C). It is likely that thicker metallic shell prohibited part of the waves from entering into the polymer matrix, but transmits the wave fronts directly from one coated layer to another coated layer in a less attenuated

fashion. It is assumed that too thick a Ni deposit layer would respond counter-productively to decrease the damping efficiency, especially in high frequency response. In the low frequency range (Figure 4.1.11), the sample with 23.3% Ni-P loading was found to damp acoustic waves better than the sample with 15.7% Ni-P loading. It is suggested that a thinner but continuous Ni-P shell will be more effective for damping acoustic waves of ultrahigh frequencies.

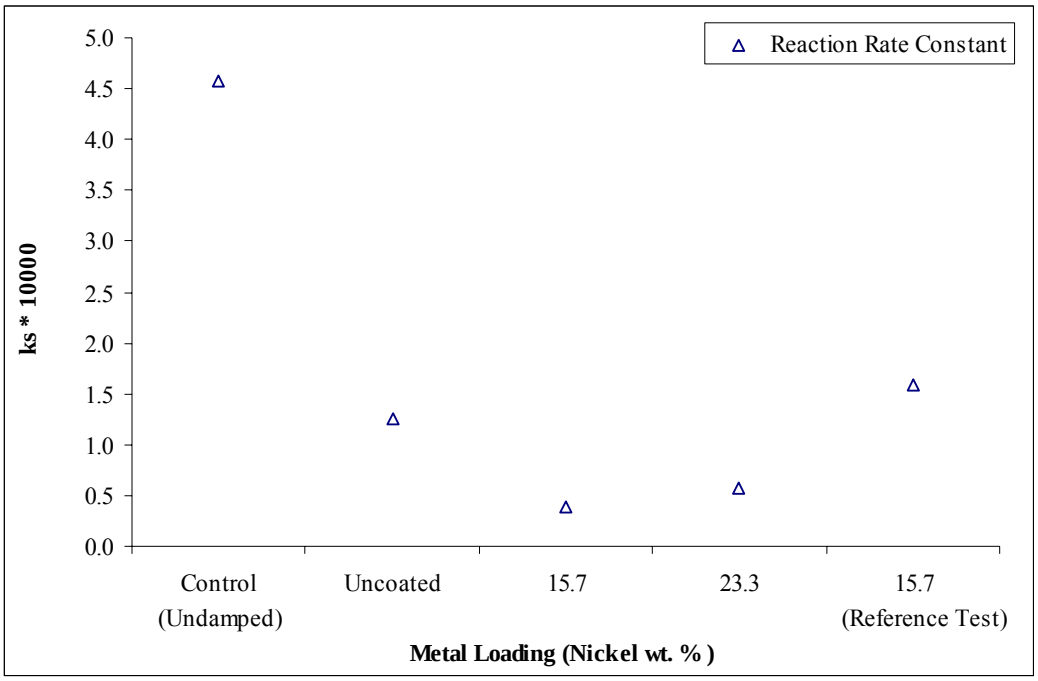

Figure 4.1.12 Surface reaction rate constant estimated by first order reaction kinetics based on ultrasonic attenuation test (Reference test: Conducted using a mixture of PMADVB and 15.7% Ni powder)

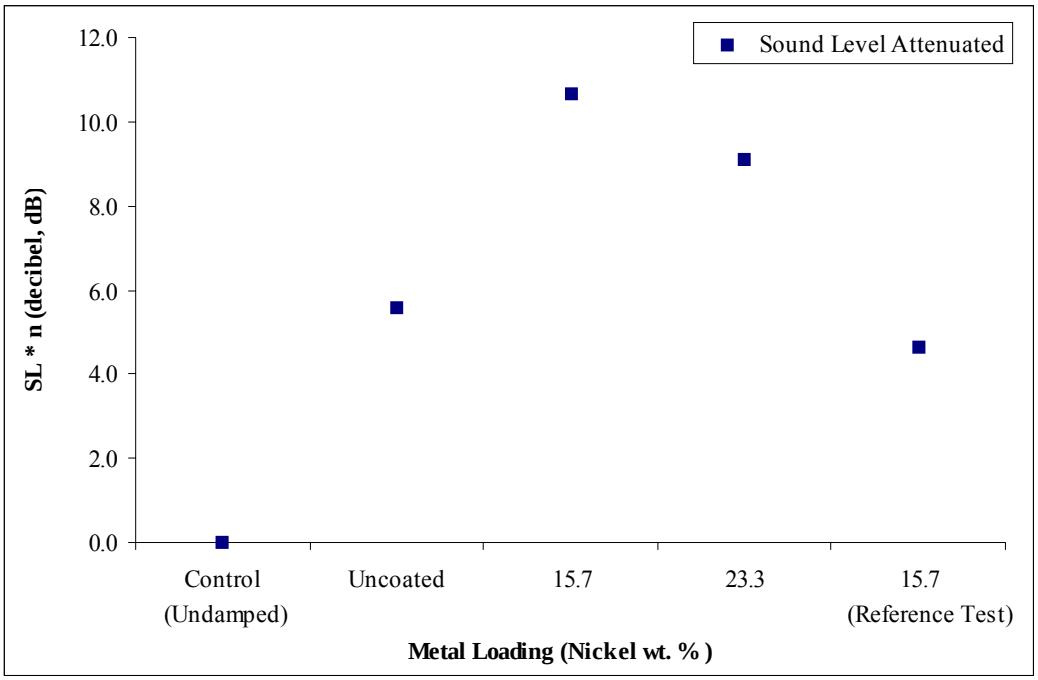

Figure 4.1.13 Estimated relative sound level attenuation based on ultrasonic attenuation test (Reference test: Conducted using a mixture of PMADVB and 15.7% Ni powder)

4.2 Acoustic Attenuation Effects of the Porous Polymer Microspheres

Executive Summary

In this section, three series of porous microspheres, namely poly(styrene-co-divinylbenzene), (SD series) poly(styrene-co-2-hydroxyethyl acrylate-co-divinylbenzene) (SDH series) and poly(acrylonitrile-co-divinylbenzene) (AD series) were synthesized and their acoustic absorption capabilities were investigated. The porous structures were created by introducing a porogen (a mixture of decane/toluene) into monomer droplets of the suspension polymerization system; the percentages of decane (25, 50 and 75%) affected not only the porous structure but also the size distribution of microspheres. This section focused attention on the sound damping effects of the porous particles. Specifically they are the relationship between pore size and sound attenuation coefficient at the same frequency as well as pore sizes and frequency of incident sound on the same absorbent basis. Finally, the effect of the nickel nanoparticles implanted in the porous matrix on sound damping properties has been investigated, accompanying with this study are the FT-IR and DSC analyses.

4.2.1 Size Distribution of PSTDVB Produced by Suspension Polymerization

Standard sieves were used to fraction the purified SD microspheres into three different portions: i.e. <50 μm and 50~100 μm and 100~300 μm. The amount of larger microspheres (100~300 μm portion) produced was found to be negligible. The stirring rod speed applied in the suspension polymerization system was fixed at 600 rpm, and the three porogen formulas (with volume ratio of decane:toluene = 1:1, 2:1 and 3:1) were used, which resulted in three different porous microspheres labeled as SD11, SD21 and SD31 respectively. The influence of porogen compositions on the size

distribution of the microspheres produced was identified and displayed in the column diagram (Figure 4.2.1).

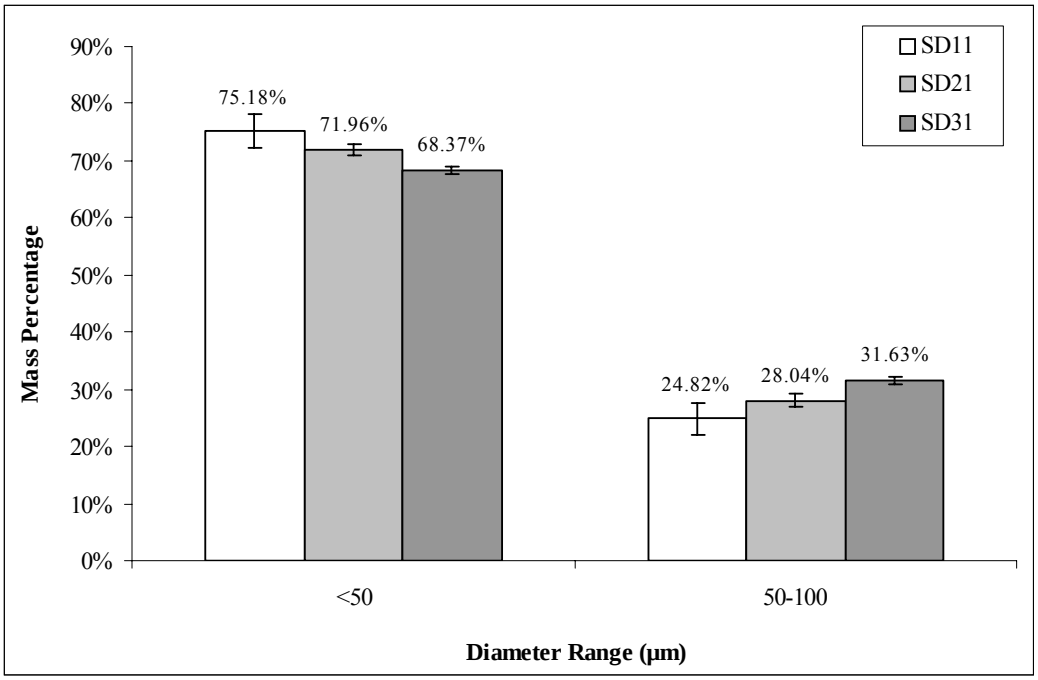

Figure 4.2.1 Size distribution of porous PSTDVB using sodium dodecyl sulfate as dispersant during synthesis

The portion of microspheres sized 50~100 μm was found to increase with increasing the decane content in the porogen. The properties of toluene and decane are listed in Table 4.2.1. Owing to the apparent difference in viscosities, it appears that increasing the decane content has effectively increased the mixture viscosity of the organic phase dispersed in water phase. Since the size distribution of the finally obtained polymer particles depended upon the size of droplets of the organic phase before the polymer matrix was formed. Thus, under a fixed stirring rate, the size distribution of microspheres produced shifted to high end when there was a finite increase in viscosity due to the addition of decane into the organic phase.

Table 4.2.1 Properties of pure decane and toluene

Properties at Ambient Temperature	n-Decane	Toluene
Density (kg/l)	0.73	0.87
Viscosity (cP)	0.92	0.56
Surface Tension (Liq-Vap, mJ/m^2)	23.9	28.5
Interfacial Tension (Liq-Water, mJ/m^2)	51.2	51.3

In the syntheses of SD microspheres, 0.5 wt % of sodium dodecyl sulfate (SDS) solution was used as dispersant. After dispersing the organic phase (mixture of monomers and porogens) in aqueous phase (micellar solution of SDS), the long lipophilic dodecyl chains were adsorbed onto the oil droplet surface, while the sulfate groups are oriented outwards from the interphase into the aqueous phase and were balanced by the counterions. The SDS stabilizers, being spread over the particle surface, created a protective layer which prevents coalescence of the particles upon

collision, on the course of polymerization (Hunter, 1993). The electrical charge produces a repulsive force between approaching droplets, and this prevents them from coalescing together.

The addition of SDS tends to produce smaller size microsphere as compared to the utilization of PVA, as discussed in section 4.1.1. PVA molecules created a steric and salvation barrier upon adsorption at the oil-water interface throughout the whole polymerization process. However, SDS molecules had more efficiently lowered down the tension at the oil-water interface. As a result, SDS appears to be a better choice of dispersants for producing smaller size particles. One of the difficulties commonly encountered was the aggregation of powders in the dried state due to the polymer-segment entanglements at the surface of these tiny particles. To lessen this, increasing surface charge through adding a strong electrolyte (e.g. NaCl) into the suspension polymerization system in addition of using surfactant was proved to be effective (Cao et al. 2000).

4.2.2 FT-IR Spectroscopy of Pristine SD, SDH and AD Microspheres

Fourier transform infrared (FT-IR) spectroscopy was employed to study the functionality of the pristine SD, SDH and AD beads. Their FT-IR transmittance spectra are shown in Figure 4.2.2, which are the identities of the three related functional groups: phenyl ($-C_6H_5$), 2-hydroxyethoxycarbonyl ($-COOCH_2CH_2OH$), and nitrile (-CN). For the spectra of SD with SDH, besides displaying the common benzene ring character: aromatic C-H stretching vibration (3100-3000 cm^{-1}), ring carbon skeletal vibration (1600-1580 cm^{-1}), C-H out-of-plane bending vibrations between strongly coupled adjacent hydrogens (900-667 cm^{-1}) and etc, the SDH

spectrum also reveals a very weak –OH vibration band at 3450 cm^{-1} because of a substantially low content of HEA unit in the SDH matrix (Table 3.2). Also because of this, the distinctive strong C=O stretching (1750-1735 cm^{-1}) and strong C-O stretching bands (1300-1030 cm^{-1}) were not apparent in the SDH series of HEA did not appear on the IR spectrum of SDH. On the spectrum of AD series, the cyanide (CN) constituent in AD series is characterized by C≡N stretching absorption of 2260-2240 cm^{-1} with a medium intensity.

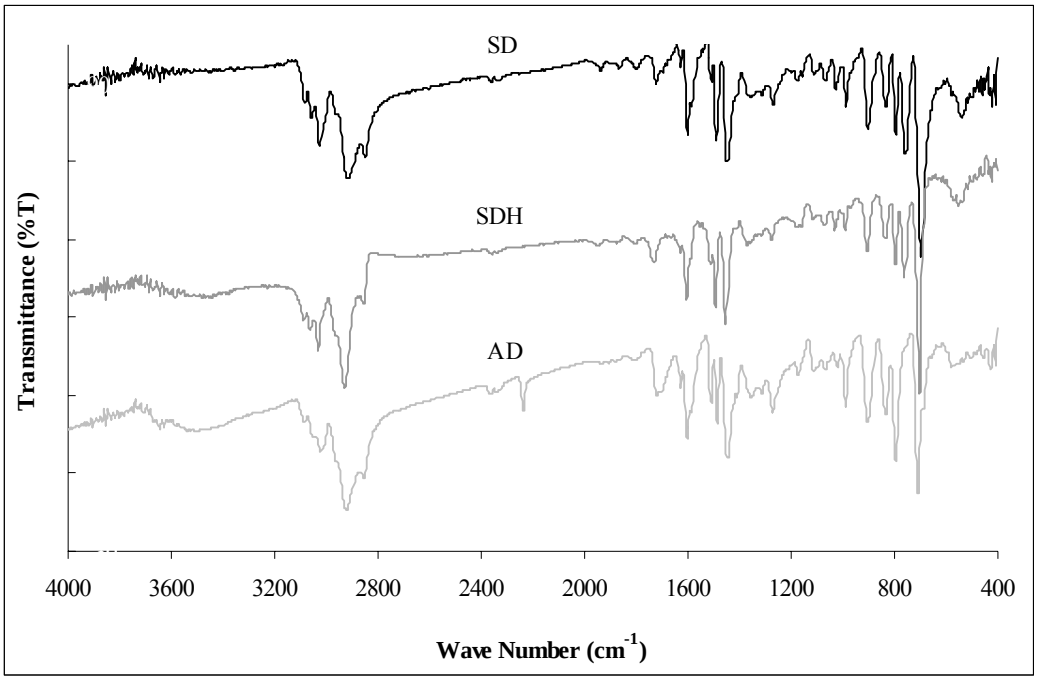

Figure 4.2.2 FT-IR fingerprints of pristine SD, SDH and AD samples

4.2.3 Studies on Pore Size and Distribution by Mercury Intrusion Porosimetry

Figure 4.2.3 presents the typical cumulative intrusion curves for styrenic microspheres prepared with and without the diluents (labeled by SD31, SD11 and SD0, respectively). Curve labeled by SD0 represents essentially nil pores and the intrusion volume shown is almost entirely due to filling in the interstitial voids among the microspheres. Curve SD11 is the characteristic intrusion profile for porous microsphere, which exhibits two distinct parts. The initial steep slope at lower pressure came from the interstitial voids, which was similar to the case for SD0. The second, the more gradual rise of slope is due to the pores within the microspheres. Curve SD31 displays the saturation intrusion value above the other two, which indicates that this sample exhibits higher pore volume.

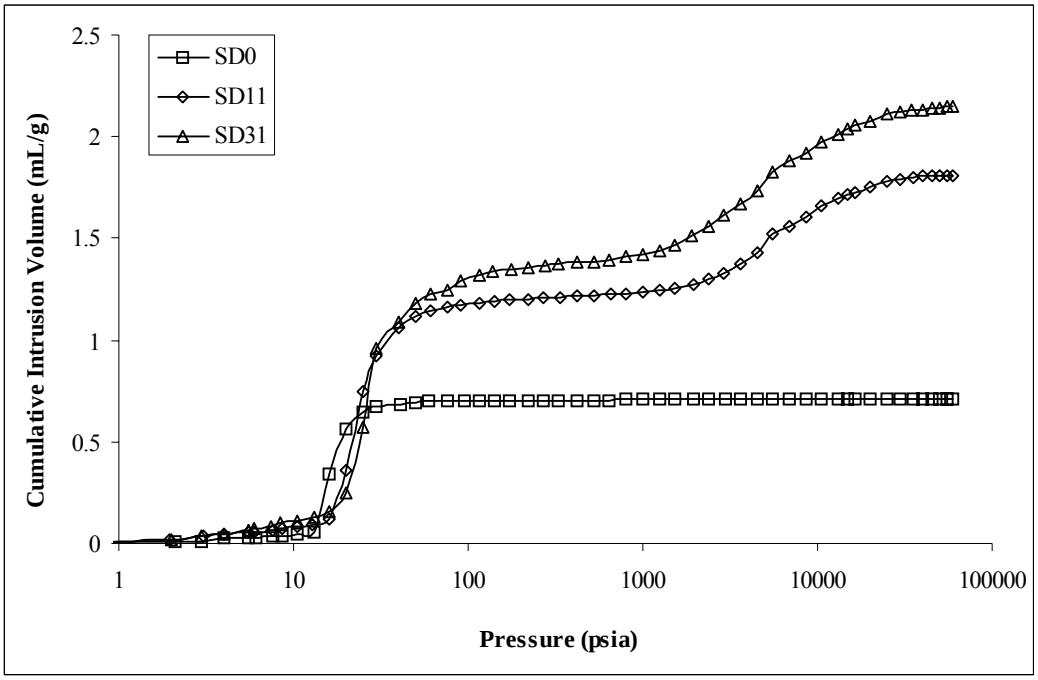

Figure 4.2.3 Cumulative intrusion curves of SD series (PSTDVB) from a mercury intrusion analysis

At the pressure interparticle void filling begins (the breakthrough pressure) the indication is an abrupt increase in the slope of the intrusion curve, followed by a notable decrease when interstitial filling is completed (Webb, 1997). A further increase in pressure will inject mercury into the voids within the individual microspheres. The incremental intrusion data under high and low pressure ranges characterize two kinds of pores, namely interstitial voids and microspheres pores. Table 4.2.2 summarizes the estimated properties measured by mercury porosimetry. Calculations based on full intrusion range (0.5-60000 psia) characterize the bulk properties of packing of the sample in the penetrometer. Whereas the porous structure of individual microspheres was reflected in the higher pressure range (500-60000 psia). For both SD and SDH series, it appears that the total microsphere pore volume, the average microsphere pore radius and porosity increase with increasing decane content in the diluents. The most decisive factor for generating the heterogeneity of the porous network of polymers is the solubility parameter and the volume fraction of diluents used.

Table 4.2.2 Full intrusion range (0.5-60000 psia) statistical calculation characterizes the bulk properties of the polymer packing within the penetrometer

	SD0	SD11	SD31	SDH11	SDH31	AD11	AD31
Computed over entire intrusion pressure range (0.5-60000 psia)							
Total Intrusion Volume (ml/g)	0.7063	1.8114	2.1451	1.8502	2.2327	2.0916	1.7346
Total Pore Area (m^2/g)	0.304	114.566	131.356	128.521	124.696	131.614	29.894
Average Pore Radius (2V/A) (Å)	46435	316	327	288	258	318	1160
Bulk Density (g/ml)	0.6128	0.3540	0.3133	0.3345	0.3074	0.368	0.3414
Apparent (Skeletal) Density (g/ml)	1.0806	0.9864	0.9550	0.8779	0.9803	0.8560	0.8372
Porosity (%)	43.2861	64.1165	67.1990	61.8949	68.6404	64.1615	59.2192
Computed over intrusion pressure larger than breakthrough pressure (500-60000 psia)							
Total Pore Volume (ml/g)	0.0013	05936	0.7596	0.6772	0.7597	0.7660	0.6422
Total Pore Area (m^2/g)	0.029	113.7	130.149	127.233	122.819	130.289	28.524
Average Microsphere Pore Radius (Å)	2	104	117	106	124	118	450
Microsphere True Porosity (%)	0.0782	21.0127	23.7943	22.6563	23.3539	23.4992	21.9247

Solvating diluents (SOL) generally produce small pores while non-solvating (NONSOL) ones produce large pores. During the synthesis of the SD network, toluene is a SOL to unfold the crosslinked polymer segments and to delay the precipitation of polymer network via high solvation degree. Decane is a NONSOL and leads to the earlier phase separation because of a considerably low solvation power to the SD network. The effect of diluents and the mechanism of formation of porous structures during polymerization had been studied in numerous publications (Wojaczynska et al., 1995; Erbay et al., 1998; Kangwansupamonkon et al., 2002; Okay, 2000). The difference between the solubility parameters of the diluents mixture (δ_m) and the copolymer (δ_p), $|\delta_m - \delta_p|$ is used to gauge the solvating power of the diluents to a cross-linked polymer (estimated in Table 3.2). The lower $|\delta_m - \delta_p|$ value corresponds to higher solvating power, and hence the pore size was found to be decrease with increasing toluene content in our studies.

The diluents system used in the all syntheses of SD and SDH is deemed to produce mesoporous materials (IUPAC classification, mesopores have radii in the range 10-250 Å). The pore size distribution curves plotted in log differential intrusion volume against pore radius are shown in Figure 4.2.4 and 4.2.5. As shown, for SD series, both samples exhibit broad pore size distribution well within the mesoporous regime, prominently between 15 and 200 Å where various peaks emerge. Increasing the decane content (SD31) shifted the pore distribution curve slightly towards larger pore size, especially for the segment of 150-1000 Å, prompting the formation of macropores. Similar distribution profiles were also generated in the SDH series, in which the right shifting of the SDH31 curve due to the decrease in solvating power was also observable though slightly. The sharp peaks were found in the regime less than 25 Å in

all distribution curves, indicates the existence of measurable interstices formed due to the agglomeration of nuclei in the early phase of polymerization processes.

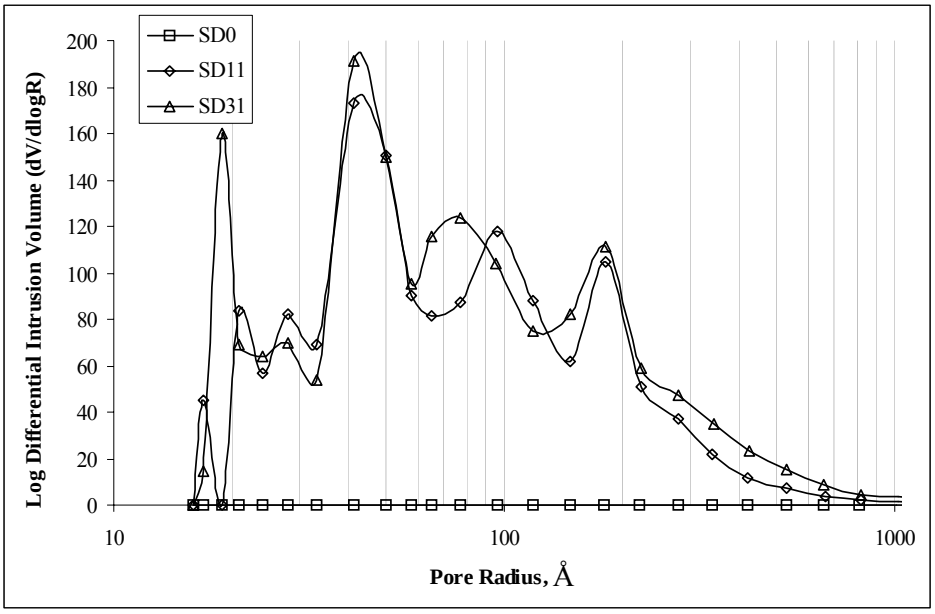

Figure 4.2.4 Log differential intrusion plot for SD0, SD11 and SD31 for the characterization of pore size distributions

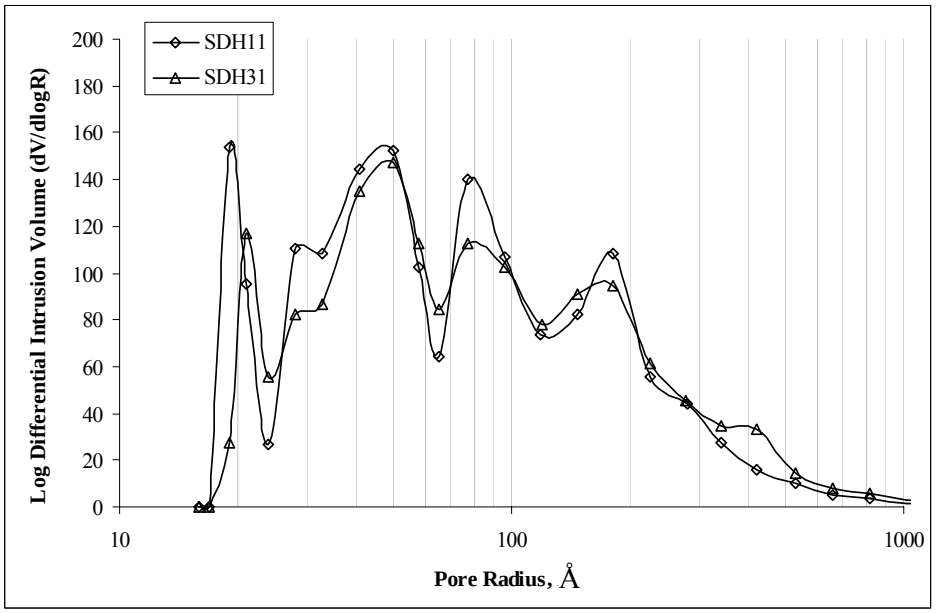

Figure 4.2.5 Log differential intrusion plot for SDH11 and SDH31 microspheres for the characterization of pore size distributions

For the copolymer acrylonitrile and divinylbenzene (AD series), the average pore radius for AD11 and AD31 is 118 and 450 Å, respectively (Table 4.2.2). This behavior may be due to the different reactivities and solubility parameters of the monomers. Acrylonitrile is much less reactive than DVB in the copolymerization system so that the polymer formed at the initial stages of polymerization contains more DVB units in the monomer mixture (Kolarz, 1994; Riqueza et al., 2002). Since AN monomers are poor solvents for DVB microgels, as the fraction of AN in the system increases, the earlier the phase separation of microgels occurs. With the presence of a higher decane-content in the feed for AD31 species, the diluents solvating power was further weakened and the extremely fast phase separation became inevitable. Pore size distribution curves show that AD11 is mesoporous, with the total intrusion volume found higher than SD11 and SDH11. For AD31 pore distribution situated between 100 and 1000 Å, the network is essentially macroporous (Figure 4.2.6).

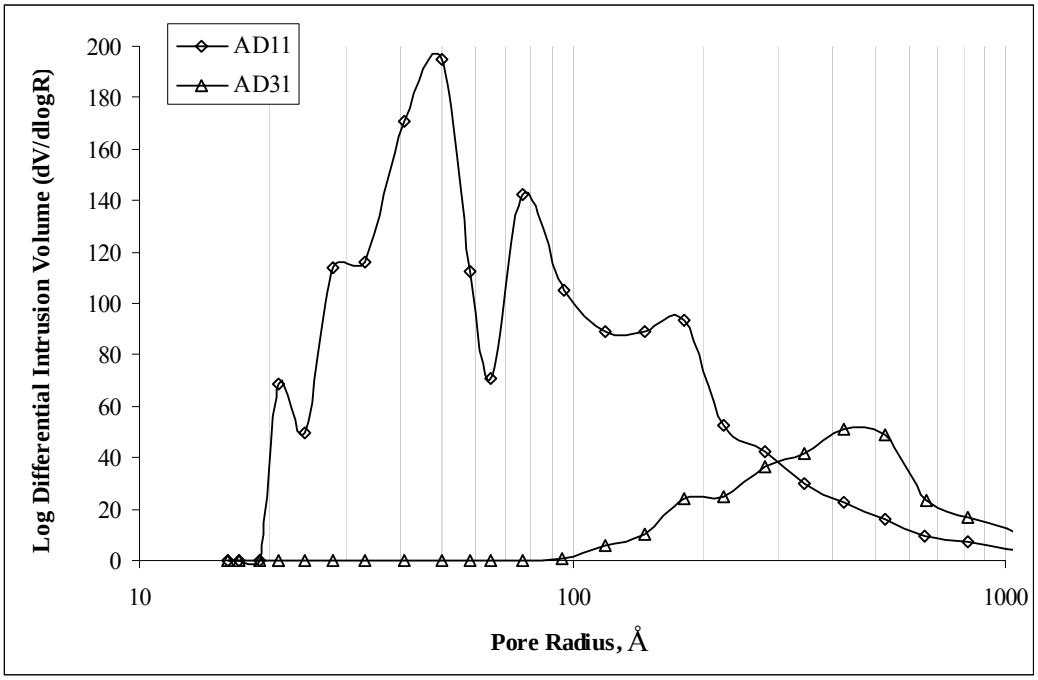

Figure 4.2.6 Log differential intrusion plot for AD11 and AD31 microspheres for the characterization of pore size distributions

The averages interstitial void radius and porosity are estimated from the mercury intrusion data of pressure ranged 0.5 psia up to the breakthrough pressure, corresponding to the inflection point of the cumulative intrusion curve (Figure 4.2.3). However, for the purpose of computation, the breakthrough pressure is fixed at 500 psia for all samples, to make sure that most of the interstitial voids have been filled by mercury. For SD series, it is interesting to note that the average interparticles void radius follows the trends:

SD0 (4.96μm)> SD11 (2.85μm) > SD31 (2.30μm)

The distribution curve below breakthrough pressure is amplified from the incremental intrusion curve (Figure 4.2.7), plot in logarithmic scale, as shown in Figure 4.2.8. It is intuitive to judge that the category (SD0) with minimum pore volume should give a corresponding minimum interstitial space. However, for this sample, it has been found microscopically that it exhibits a very smooth surface, compared to SD11 and SD31 counterparts. Since the contact between the rigid and smooth SD0 beads was more like point contacts, while the contact of beads with rougher surface was more like face contacts (gear-like match) when they were brought close under the high pressure, so the latter ones could be packed closer with a lower fraction of interstitial void. This occasion could be schematically illustrated by the sketch, as shown in Figure 4.2.9.

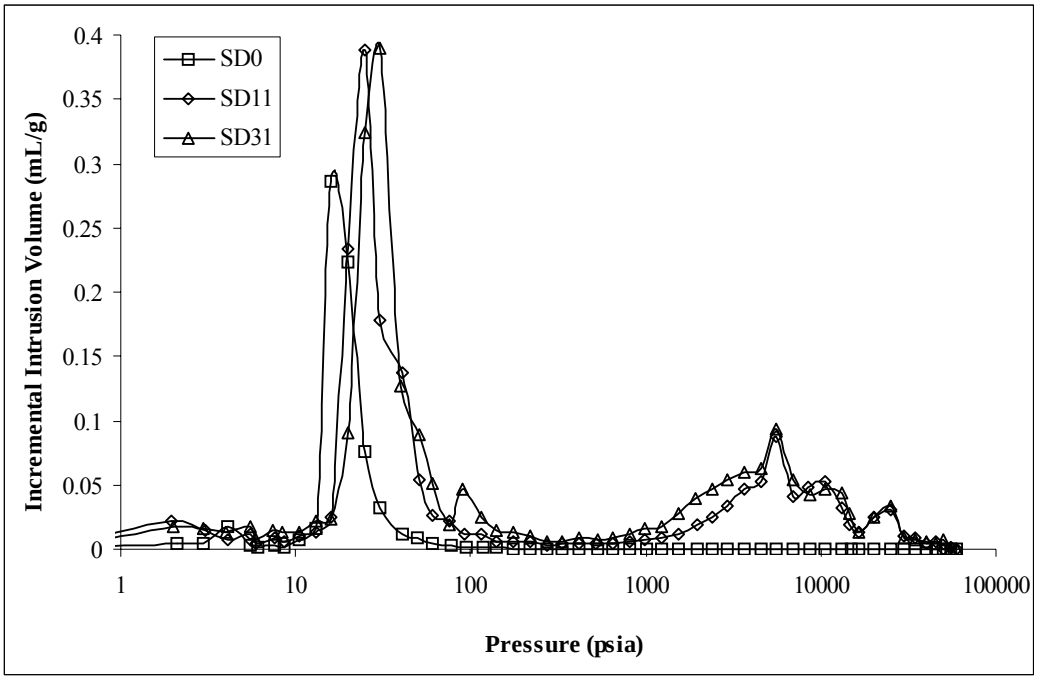

Figure 4.2.7 Incremental intrusion curves of SD series (PSTDVB) from a mercury intrusion analysis

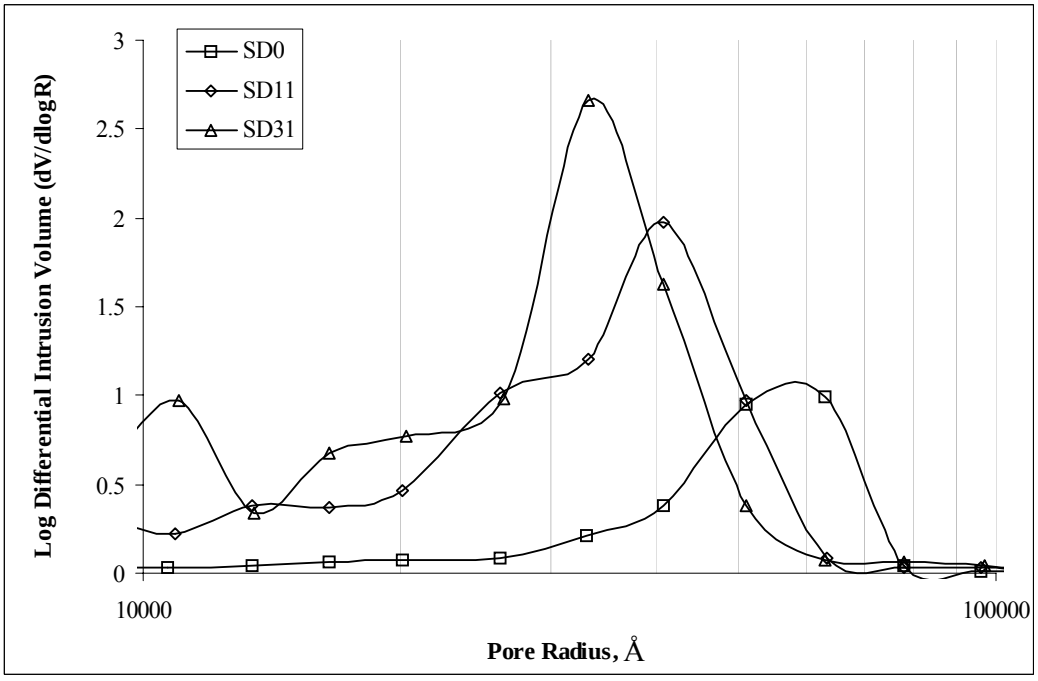

Figure 4.2.8 Log differential intrusion plot for SD0, SD11 and SD31 for the characterization of interstitial voids size distributions

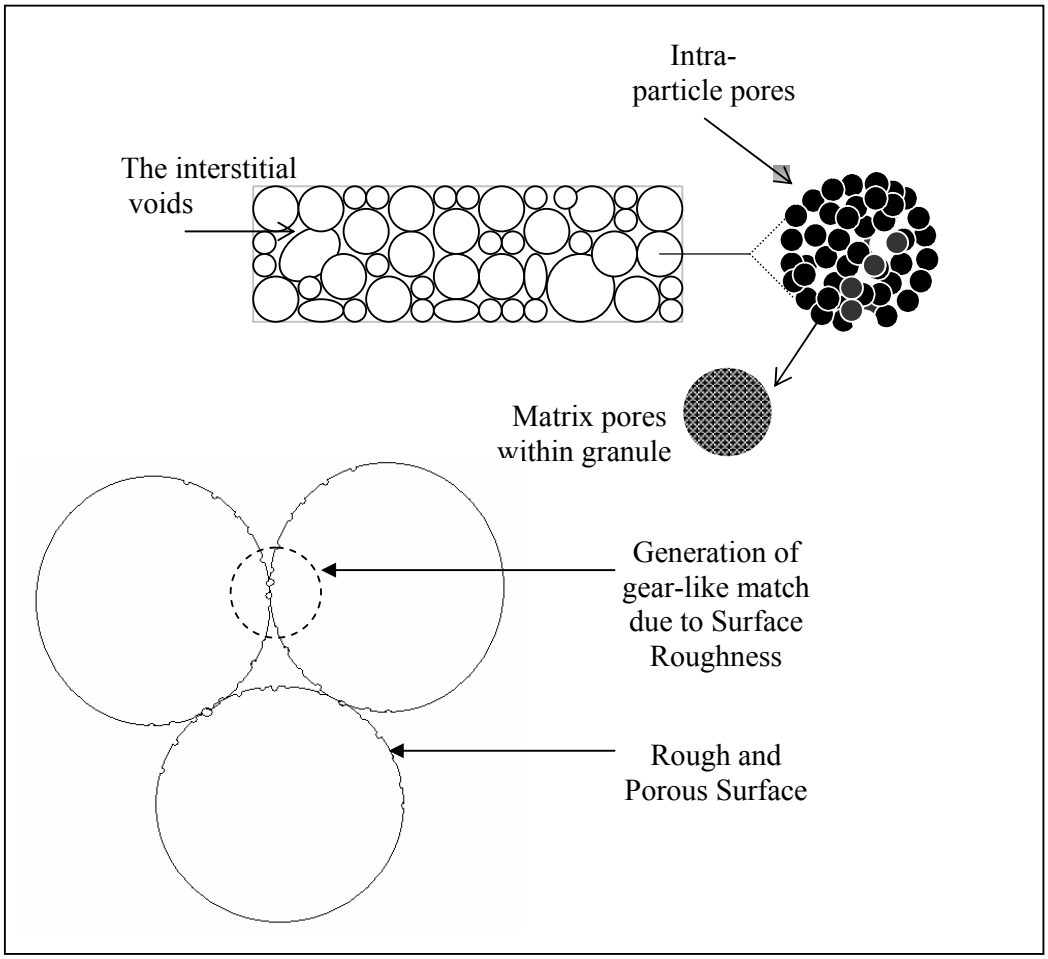

Figure 4.2.9 Three levels of porous structures existing in the disk used to conduct acoustic damping test

The same argument is held true for the SDH and AD categories despite the difficulty of creating a quantitative description that accounts for the distinctions of interstitial voids from the perspective of salvation power. Using porosimetry approach, it has been clearly shown that the packing density of powders in the penetrometer is very sensitive to the surface state of microspheres except the pressure applied. According to this fact, the important conclusion drawn is that the sound attenuation test result was to be affected by the different interstitial spaces due to use of different powders no matter the same hydraulic pressure was used for the sample (pellet or disk) preparation.

4.2.4 Matrix Morphology and Surface Topology of Porous Microspheres

Figure 4.2.10(a)-(c) presents the SEM micrographs of SD beads under low magnification. From Figure 4.2.10(a), the microspheres appear to have the utmost diameter less than 50 μm, with a broad distribution. This is typically the limitation of synthesizing polymer beads by suspension polymerization method. The SD0 beads displayed a very smooth and non-porous surface (Figure 4.2.10(b)). In contrast, the highly porous SD31 consists of rough and spongy-like surface, which is readily observable under low magnification.

A closer view by FE-SEM revealed the detailed porous images of the SD series (Figure 4.2.10(d)-(f)); it served as the direct and supportive evidence to the porosimetry analysis. As indicated in Table 4.2.2, porous matrixes were crafted by increasing progressively the content of decane in the toluene/decane diluents mixture. The SD11 sample (Figure 4.2.10(d)) is formed by flakes of interconnected polymer micro domain, which are distributed evenly. The surfaces were found to be porous, with the pores diameter less than 100nm. With higher toluene content in porogen system, the microsphere surface was observed to possess relatively small average pore size, as compared to the counterpart with higher decane content (Figure 4.2.10(e),(f)). In addition, agglomerates of grains of various sizes are responsible for the broad size distribution of pores. The larger interconnect agglomerates found on SD31 microsphere (Figure 4.2.10(f)) corresponded to the highest decane content, showing that lower solvating power in this particular porogen system lead to heavier phase separations and resulted in larger agglomeration in the end of synthesis. The results are consistent with porosimetry data.

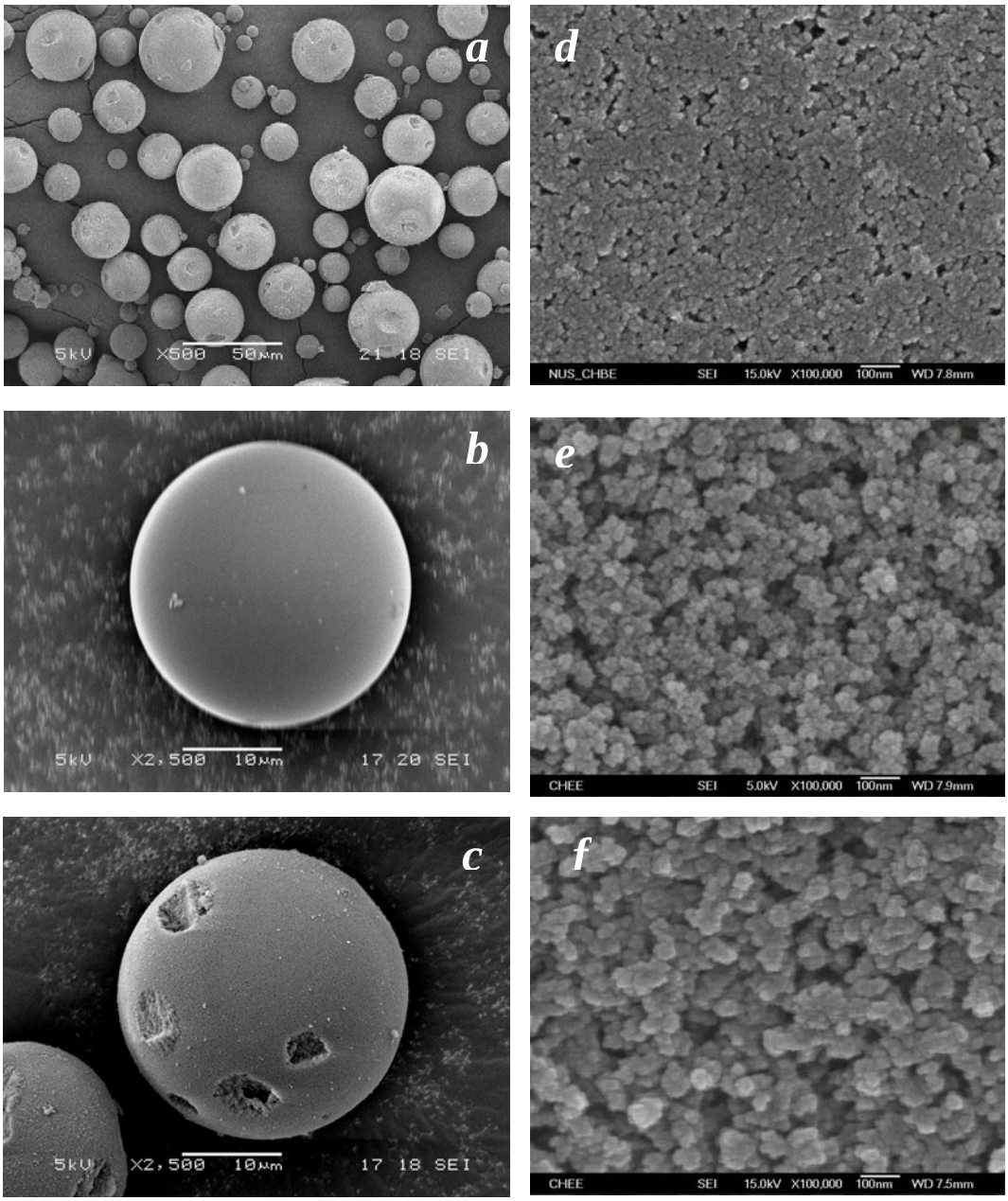

Figure 4.2.10 SEM micrographs of the microspheres (a) SD31 (broad view), (b) SD0, (c) SD31, at low magnification; FE-SEM micrographs of the SD series surface morphology affected by different solvating power (d) Dec/Tol=1:1, (e) Dec/Tol=2:1, and (f) Dec/Tol=3:1 at 100,000X

For AD series (Figure 4.2.12(a)-(b)), surface morphology of mesoporous AD11 was found to be analogous to SD11 and SDH11 counterpart. Yet, the agglomeration of particles on the AD31 surface is less obvious, and more clearly characterized by large and distributed dented channel. It is aforementioned that the AN monomers is less reactive compared with the DVB crosslinker. The density distribution across the radial direction of each microsphere is unquestionably the consequence. During the course of polymerization and extraction process, polymer chins in the shell layers of polyacrylonitrile beads that have much lower crosslinking degree than their cores would easily be softened and fused together whenever the glass transition barriers of the linear or lightly branched segments are surmounted. Meanwhile, very large pores were still formed as a result of the NONSOL effect of decane, which were also identified by mercury porosimetry measurement.

Figure 4.2.11(a)-(c) presents the surfaces deposited with tiny spherical nickel particles. The metallic grains have the size ranges 30-100 nm, distributed on the porous surface or incorporated into the voids. The approach developed for depositing nickel colloids directly onto porous polymer matrix, as detailed in section 3.3.2, was proven successful. Further improvement was carried out to pursue higher metal loading and more evenly distribution of the Ni nanoparticles onto porous polymer surface. It was realized by integrating a low content of hydrophilic monomer units, hydroxyethyl acrylate (HEA), with the SD network. Typically, 10 mol % of HEA was arranged to copolymerize with 90 mol% of ST, using same molar ratio of DVB as the crosslinker, to produce a nominal crosslinking degree of 50% (SDH series).

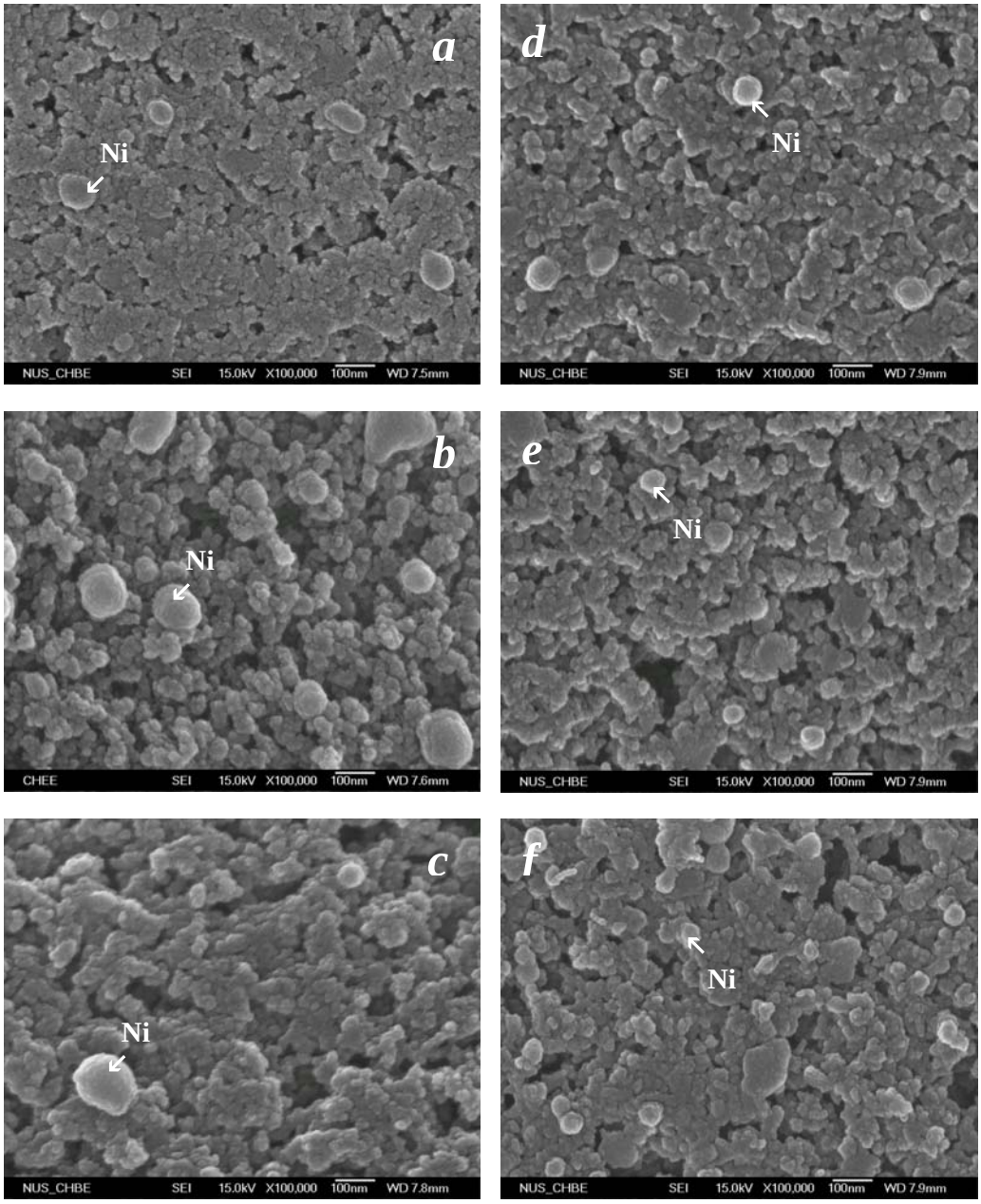

Figure 4.2.11 FE-SEM micrographs of the microsphere surface morphology (a-c) SD11-SD31 (d-f) SDH11-SDH31 deposited by nano-sized nickel particles at 100,000X magnification

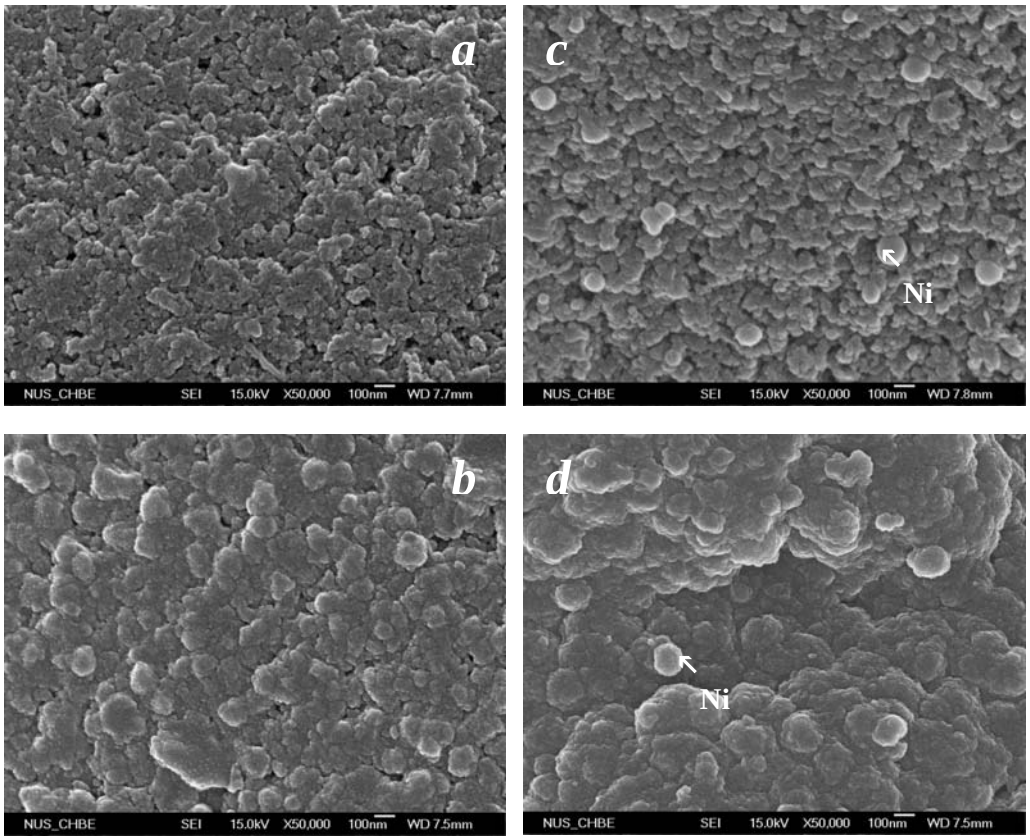

Figure 4.2.12 FE-SEM micrographs of the microsphere surface morphology (a) AD11, (b) AD31, (c) AD11 with nickel deposition and (d) AD31 with nickel deposition, at 50,000X magnification

Figure 4.2.11(d)-(f) present the surface morphologies of SDH series, deposited by nickel nanoparticles. On this substrate, smaller metallic grains, 30-80 nm, could be reached. The improvement was more noticeable on more porous surface, e.g. on the SDH31 surface, the nickel particles formed were smaller, more spherical and more uniformly distributed. Introduction of hydrophilicity to porous and bumpy surface enhanced infiltration of nickel ions into the polymer matrix from the methanol solution due to the improvement on solvent wettability and the decrease in pore diffusional resistance. Also, the rougher surface distributed by larger and deeper porous tend to capture the nickel grains formed during the reducing process, confined the growing of the grains and hence reduced their sizes. SDH11 displayed a less porous surface, which cut down the capability of lodging the nickel ions prior to reduction process. In short, the surface porosity and hydrophilicity have certain impact on regulating the size and shape of deposited nickel nanoparticles, provided that the loading and reduction procedures are controlled carefully.

A parallel study done was the metallization of the microspheres of AD series (AD11 and AD31). It appeared according to Figure 4.2.12(c)-(d) that the sizes of the nickel grains developed were bigger and irregular. The attempt to utilize the strong coordination ability of cyanide group on the surface of AD was not satisfactory. The nitrile group though possesses strong affinity with Pd ion to form complexes did not show the same effect on Ni ion. In summary, HEA modified SD matrix (SDH series) offered a better surface wettability to methanol and hence an apparent improvement on the metal loading.

4.2.5 An Approximate Physical Model for Sound Absorption in the Low Audio Frequency Field

The experimental setup and sample preparation for the sound absorption assessment have been described in section 3.4.4. In the low frequency sound field, the whole testing disk or some parts of it are driven to undergo vibration with reduced amplitudes relative to those of the incident sound wave, in which a substantial part of the original sound energy is dissipated into heat due to the non-elastic nature of vibration although a part of it was re-radiated into the right-hand-side chamber (Figure 3.1), which is equivalent to the penetration of sound. The absorption coefficient of this damping course can be approximately treated as the simplest case of a plane sinusoidal sound wave impinging perpendicularly onto a vibrating membrane, whose dynamic properties are completely characterized by its mass inertia (Kuttruff, 2000; Pierce, 1989).

For this case, we have

$$\alpha_v = \left[1+\left(\frac{\omega M}{2\rho_0 c}\right)^2\right]^{-1} \cong \left(\frac{2\rho_0 c}{\omega M}\right)^2 = \left(\frac{\rho_0 c}{\pi f d \rho_b}\right)^2 \qquad (4.2.1)$$

where α_v is the absorption coefficient due to the existence of non-elastic (or viscous) vibration component of the testing membrane, ω is the angular velocity of the incident sound, M is the mass per unit area of the testing disk, ρ_0 is the static value of air density, c is the sound velocity, d is the thickness of the membrane and ρ_b is the bulk density of the disk. This simplification is allowable if the characteristic impedance of air to sound travel is smaller as compared with the bulk reactance of the polymer disk. Thus the absorption brought about by the non-elastic vibration becomes noticeable in low audio frequency field.

As the testing membrane was a porous monolithic medium, through which sound waves penetrating was never a negligible factor because it consumed sound energy while the sound traveling through slim pore trenches. With this regard, Rayleigh model (Kuttruff, 2000) offers a highly idealized vision for understanding the pore-flow effect. This model supposes that sound propagation take place in a single, straight and narrow channel and consequently the profile of the air stream be determined completely by the viscosity of air, which is valid at sufficiently low frequencies and less twisted pore tubes. With the assumption of steady flow and same lateral distribution of flow velocities in the interior of the channel, the flow resistance of the channel per unit length has virtually the same value. For narrow channels with circular cross-section (radius r), the flow resistance per unit length is given by

$$R_f = \frac{8\eta}{r^2} \qquad (4.2.2)$$

where η denotes the viscosity of the streaming medium.

In fact, the testing membrane did not contain well-separated and shape-defined channels but rather irregularly shaped cavities which are mutually connected. To extend the applicability of Rayleigh model to the present porous medium, it can be assumed that the efficient flow resistance of the pellet is directly proportional to thickness (*d*) and the tortuosity (τ), and inversely proportional to the total porosity (ε) of the materials. Hence the effective flow resistance R_{eff} could be mathematically expressed by

$$R_{eff} \propto \frac{8\eta d\tau}{\bar{r}^2\varepsilon} = \psi\frac{8\eta d\tau}{\bar{r}^2\varepsilon} \qquad (4.2.3)$$

where ψ is the shape factor account of the complexity of the packing system with a proper dimension, and $\bar{r}$ is the mean radius of the pores in the testing disk.

For the Rayleigh model, by solving the force balance equation on an unit length element in a rigid channel, with R_f replaced by R_{eff}, the complex propagation constant for a porous packing disk can be expressed by:

$$k = \beta - i\gamma = \frac{\omega}{c}\left(1 - i\frac{R_{eff}}{\rho_0 \omega}\right)^{1/2} \qquad (4.2.4)$$

where $\beta = 2\pi/\lambda$ is the phase constant and γ is the attenuation constant. To study the limiting cases, for low frequency, since $\sqrt{-i} = \frac{1-i}{\sqrt{2}}$ and $\frac{\omega^2}{c^2} \to 0$

$$\beta - i\gamma = \left(\frac{\omega^2}{c^2} - i\frac{\omega R_{eff}}{\rho_0 c^2}\right)^{1/2} \cong \left(-i\frac{\omega R_{eff}}{\rho_0 c^2}\right)^{1/2}$$
$$= \left(\frac{\omega R_{eff}}{\rho_0 c^2}\right)^{1/2}\sqrt{-i} = \left(\frac{\omega R_{eff}}{\rho_0 c^2}\right)^{1/2}\frac{1-i}{\sqrt{2}} = \left(\frac{\omega R_{eff}}{2\rho_0 c^2}\right)^{1/2} - i\left(\frac{\omega R_{eff}}{2\rho_0 c^2}\right)^{1/2}$$

Therefore:

$$\beta = \gamma = \left(\frac{\omega R_{eff}}{2\rho_0 c^2}\right)^{1/2} = \left(\frac{\omega}{2\rho_0 c^2} \times \psi\frac{8\eta\tau\, d}{\bar{r}^2 \varepsilon}\right)^{1/2}$$
$$= (8\pi\eta\, d\,\psi)^{1/2}\left(\frac{f\tau}{\varepsilon\rho_0 c^2 \bar{r}^2}\right)^{1/2} \qquad (4.2.5)$$

or,

$$\alpha_p = \gamma = (8\pi\eta\, d\,\psi)^{1/2}\left(\frac{f\tau}{\varepsilon\rho_0 c^2 \bar{r}^2}\right)^{1/2} \qquad (4.2.6)$$

α_p is known as the absorption coefficient due to porous packing. Hence, for the low frequency absorptions where both intrinsic vibration and pore flow caused dissipative effects can be described by combining equations (4.2.1) and (4.2.6), namely the effective sound attenuation coefficient (α) at low frequency is modeled as:

$$\alpha = K_v \alpha_v + K_p \alpha_p$$
$$\alpha = K_v \left(\frac{\rho_0 c}{\pi f t \rho_b} \right)^2 + K_p \left(8\pi\eta d\psi\right)^{1/2} \left(\frac{f\tau}{\varepsilon \rho_0 c^2 \bar{r}^2} \right)^{1/2} \qquad (4.2.7)$$
$$= \phi_v + \phi_p$$

where K_v and K_p are the weighing factors for the respective mechanism, ϕ_v and ϕ_p are the contribution terms for the intrinsic vibration mechanism and the flow-related dissipative effect, respectively.

4.2.6 Characteristic Attenuation Behavior in Low Frequency Range

When the incident sound frequency band (100-400 Hz) was located to test the disks made up of three types of SD powders, the three corresponding profiles signaled by different attenuation coefficients were obtained (Figure 4.2.13). The sound attenuation coefficients increase slightly with increasing frequency up to 250 Hz, and their magnitudes displayed in this very low frequency range demonstrated that the pore-flow-related dissipative effect outweighed over the intrinsic-vibration-bound one. This phenomenon can also be elucidated by equation (4.2.7), in which the term standing for the intrinsic vibration effect reduces with increasing frequency and balances the increase of the second term. Beyond 250 Hz, the attenuation coefficient underwent a drastic drop due to the resonance of the testing tube as aforementioned (discussed in Section 3.4.4); however, the attenuation profile of the disk made of SD0 microspheres that do not contain intra-pores displayed a rather broader resonance band compared with those of the other two, this outcome implied that through channels in the testing disks due to the connections of intra-particle pores played a key role in conveying sound wave. In contrast, interstitial voids in SD0 disk could not be effectively linked to form penetrating channels and behaved like a vibrating wall instead under impact of the incident sound wave. It is thus estimated that the broader resonance band was the result of overlaps, both constructively and destructively, between the resonance band of the testing tube and the sound waves re-radiated from the intrinsic vibration of the disk.

The typical cumulative intrusion curves for the three types of SD powders (Figure 4.2.3) showed the existence of interstitial void and intra-particle pores, respectively. Curve-SD0 displayed only low pressure intrusion slope due to the filling at interstitial

voids among the microspheres. On the contrary, curve-SD11 and curve-SD31 both revealed also high pressure intrusion slopes due to the filling at intra-particle pores. Furthermore, the porosimetric analysis showed that both SD11 and SD31 contained meso-pores having abundant sizes around 100 Å while SD0 did not (Figure 4.2.4). Hence, it could be considered that it was these meso air cavities that introduced additional dissipative effect due to frictions of flow at air-polymer inter-phase. It follows that SD31 owning greater specific pore volume but similar mean pore radius should certainly offered more pronounced pore-flow dissipative effect.

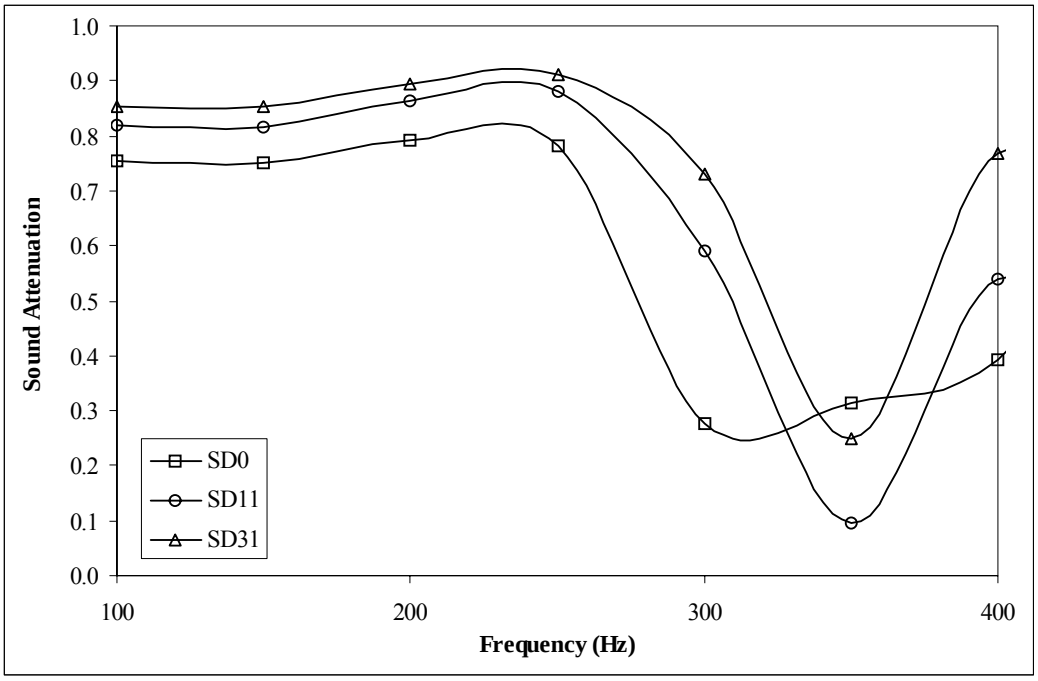

Figure 4.2.13 Sound attenuation behaviors of SD series at low frequency (100-400 Hz)

A further query about the pore-flow attenuation in the low frequency range is whether the pendant functional groups on the pore wall (i.e. on the cross-linked polystyrene backbone) will affect the sound damping effect. Two particular functional groups were investigated. For SDH series, introduction of a low content (~10% by mole) of the hydrophilic alcoholic group into SD (Table 3.2) did not change the profile as displayed on Figure 4.2.14 by SD series but altered the sequence of effect of porosity despite an insignificant difference. When inspecting the pore size distribution profiles of SDH11 and SDH31 (Figure 4.2.5), it can be found SDH11 contained a greater portion of meso-pores in the range from 80 to 100 Å than SDH31. Compared with the pore-size effect of SD series, it can be concluded that the pore channels with sizes around 100 Å were more effectively than bigger pores to damp the acoustic waves (<250 Hz), and the hydrophilic functional group did not enhance sound attenuation providing moisture effect was excluded by using dry disk and controlling short testing time. For AD series, use of strong polar acrylonitrile monomer to substitute all styrene monomer dramatically altered the pore size distribution (Figure 4.2.8); on this diagram AD11 displayed a much greater volume fraction of the meso-channels (around 100 Å) than AD31. Similarly, AD11 showed higher sound attenuation coefficient than AD31 (Figure 4.2.15). As the nitrile group of polyacrylonitrile has an ostensibly higher permanent dipole moment than the phenyl group of polystyrene, the AD network is more rigid than the SD network, and the raise of rigidity (elasticity) in a polymer network caused reduction in damping effect, which is particularly apparent at tube resonance frequency (at 350 Hz). The implication is clear: mechanical energy becomes more difficult to be converted to thermal energy via stimulating segment motions with increasing elasticity in the polymer network.

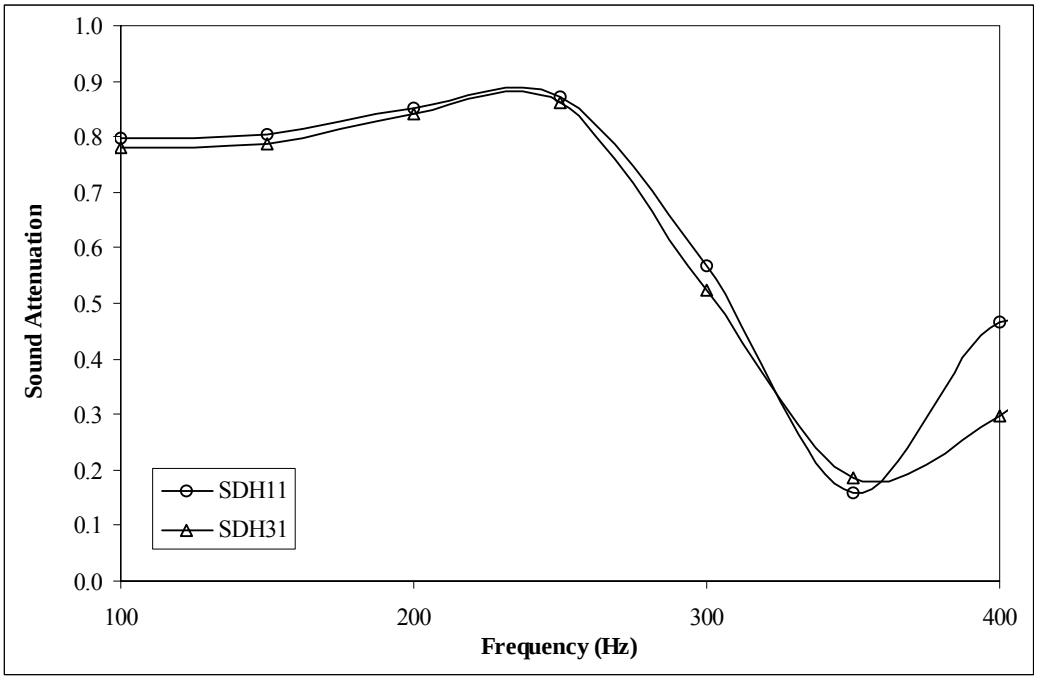

Figure 4.2.14 Sound attenuation behaviors of SDH series at low frequency (100-400 Hz)

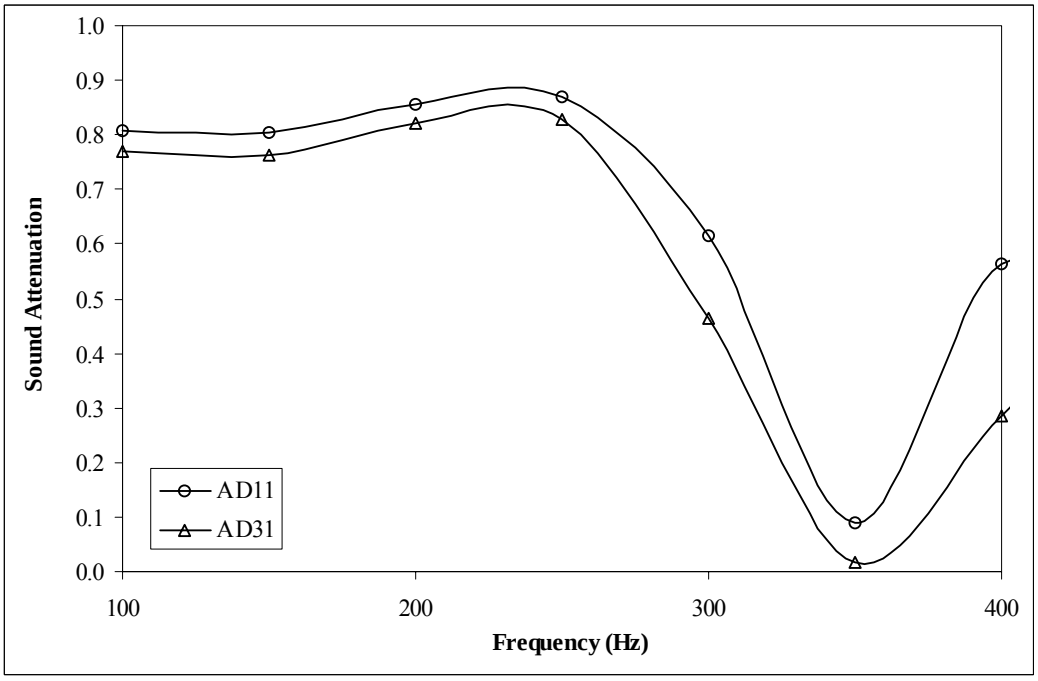

Figure 4.2.15 Sound attenuation behaviors of AD series at low frequency (100-400 Hz)

4.2.7 Characteristic Attenuation Behavior in High Frequency Range

In the relatively high frequency (4000–5000 Hz) sound field, the basic assumptions of the Rayleigh model are no longer valid. Under this circumstance the conversion of the longitudinal deformation of air into the shear deformation (relative segment motions) of the polymer network has reached the saturation limit, which means that the visco-component of polymer network would shrink with increasing frequency since its segment motions cannot follow the fast amplitude changes of the air impacts. The mismatch of impedance (elasticity) between polymer framework and air to the transport of sound waves is the main factor affecting the damping result. It will be expanded with making the polymer framework more difficult to undergo deformation (the molecular characteristic of elasticity), and will hence reduce the contribution of the polymer phase to the sound damping (or the loss modulus). However, increasing the impedance mismatch will possibly enhance energy storage in different forms of intra-molecular motions of air molecules due to elastic collisions. In the high frequency sound filed, the meso-sized channels made no difference from sub-micron interstitial voids in damping according also to Equation 4.2.7. Experimental observation showed that the different porous structures in either SD or SDH series did not change the sound attenuation coefficients clearly, which were all in the range of 0.6 – 0.8 (Figure 4.2.16 and 4.2.17). Nevertheless, in these two series lower porosity did present a small privilege in damping the sound wave despite insignificant porosity differences existing in each series. The representative case might be SD0 disk, which made up of nonporous microspheres as noted above, showed minor advantage over the porous counterparts. As remarked by Jarzynski (1990), the sound attenuation includes scattering by in-homogeneities, the action of denser matrix is related to higher availability of normal incidence surface, which was capable of reflecting and

redirecting part of incident high frequency waves. Similarly, AD31 pellet also exhibited somewhat higher sound attenuation coefficient than AD11 over the frequency range of study (Figure 4.2.18). Following the above interpretation, this was the rational outcome since AD31 possessed lower specific pore volume than AD11 (Table 4.2.2).

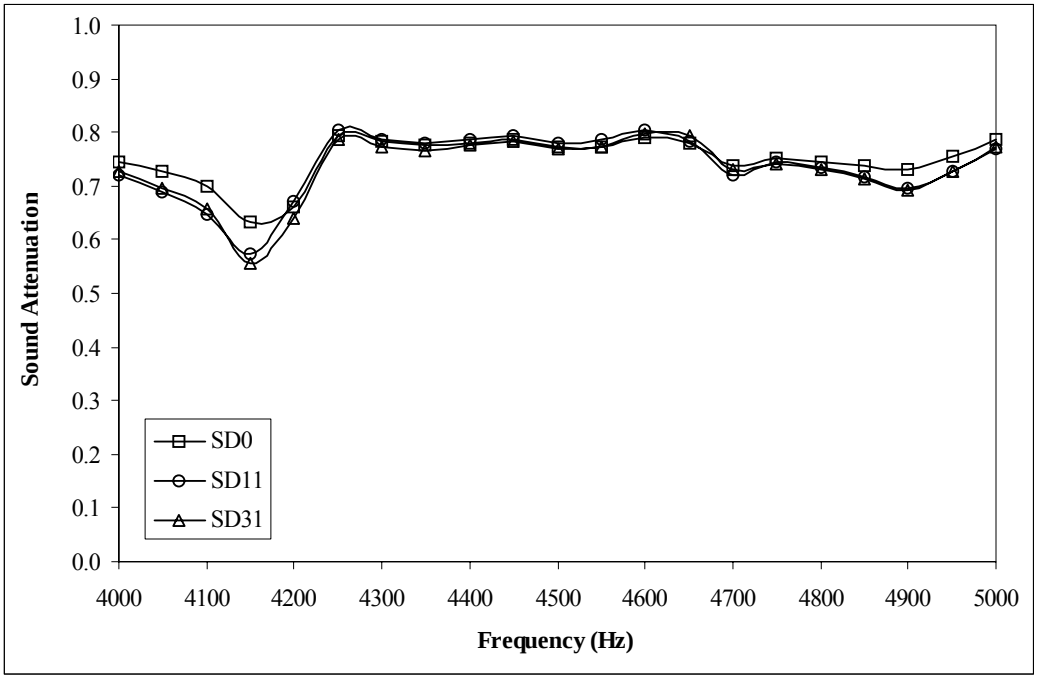

Figure 4.2.16 Sound attenuation behaviors of SD series at high frequency (4000-5000 Hz)

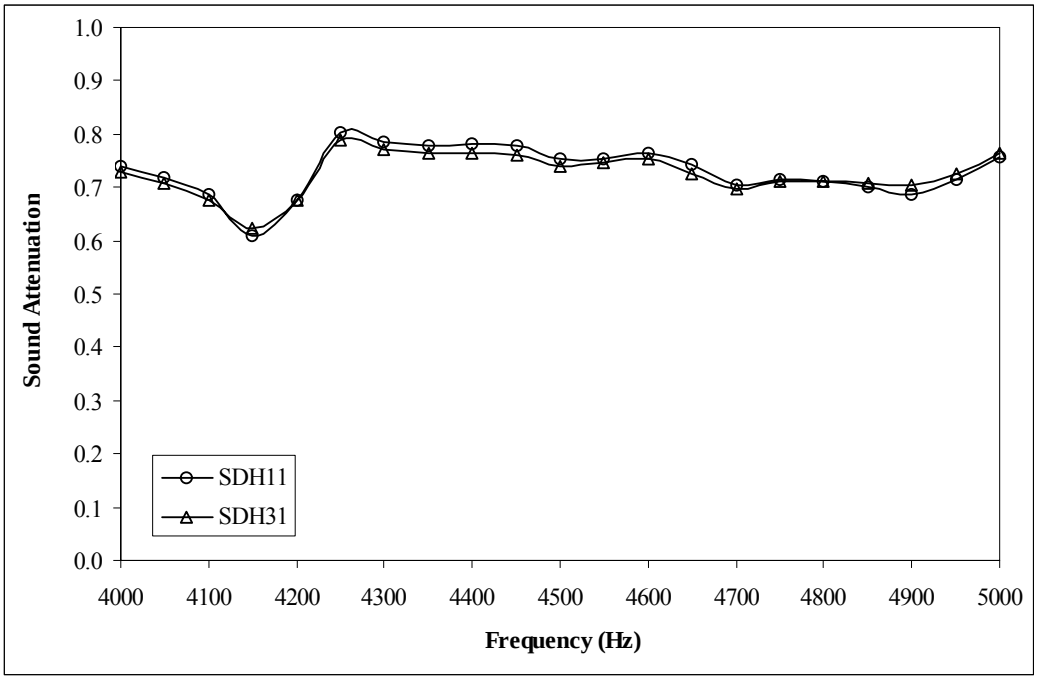

Figure 4.2.17 Sound attenuation behaviors of SDH series at high frequency (4000-5000 Hz)

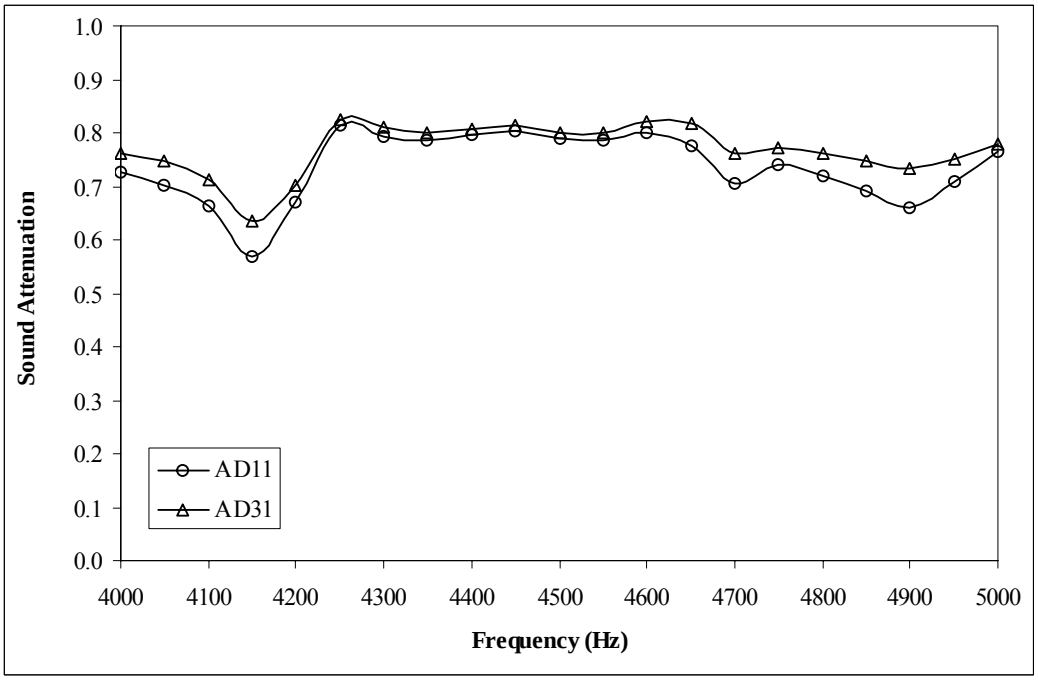

Figure 4.2.18 Sound attenuation behaviors of AD series at high frequency (4000-5000 Hz)

4.2.8 Effects of Tiny Ni Nano-Particles Deposited on Microspheres

When nano-sized Ni particles (<100nm, 0.5 % by weight) were deposited on the three types of polymer microspheres, they indeed altered the attenuation profiles displayed by the pure polymer counter parts, the effect (positive or negative) and extent were contingent on frequency. Such outcome is believed to have root cause from the highly dispersion of Ni nano-particles in the resided polymer matrix; the biggest Ni balls that could be recognized clearly on Figure 4.2.11 had diameters around 100 nm, there were smaller ones that intermingle with polymer grains. If assuming the density of Ni balls be 8 g/cm^3 and their mean diameter 100 nm, the testing disk (~1.4 cm^3) would contain about 6×10^{11} particles. Lest there are many unsaturated coordination sites on Ni nano-particles, adsorption of the free segments (between two crosslinking points) on Ni particle can never be omitted and the effect of adsorption on sound damping relies on several factors, including affinity of the pendant function groups with Ni(0) atom, flexibility of the free segments, distribution of crosslinking points and surface states of Ni particles.

A relatively simple way to understand the effect is the comparison of IR spectra and DSC diagrams of the samples before and after metallization. In comparison with SD11, SD11-Ni revealed the stronger peaks (transmittance %) of characteristic IR absorptions of the polymer (benzene skeletal vibrations and out-of-plane bending of C-H bonds) (Table 4.2.3). This is interpreted as the presence of electron donor (benzene ring) – acceptor (Ni atom) interaction, by which the structure formed was analogous to metallocene. It was likely that only a small fraction of phenyl groups involved this interaction because of no changes in IR frequencies on the whole. However, these allotted interaction sites perturbed the glassy assembly of linear polystyrenic segments

with including free space into it, hence a decrease in the extent of collective vibration of phenyl groups gave rise to a decrease in IR absorption. In addition, the continuous and feeble glass transition curvature (of SD11) was broken down into the two separate steps (for SD11-Ni) with the lower-temperature one more apparent was observed by DSC analysis, a sign of increasing freedom for thermal motions of the polymer segments (Figure 4.2.19). For the AD11 and AD11-Ni samples, there was an increase in the stretching frequency of C≡N bond by about 2 cm^{-1}, which suggested that the adsorption of a small part of nitrile groups to Ni particles would loosen the matrix density of the polyacrylonitrile assembly due to the twisting effect. As a result, strong dipole-dipole interaction between CN groups was partially freed. A slight decrease in the upper-bound T_g temperature also support the loosening of the AD matrix (Figure 4.2.20).

Table 4.2.3 FT-IR and DSC Traces of Ni Nanoparticle-Polymer (SD11 and AD11 series) Interactions

Samples		*IR finger prints* Frequency (cm^{-1})	Relative intensity (%)*	*DSC analysis* T_g range (^oC)
SD11	bending of C-H oop**	698.6 760.3 795.1 829.8	115.2 62.5 50.4 41.1	63 ~ 123
	Ring skeletal vibration	1455.0 1493.6 1605.5	78.0 73.3 67.2	
SD11-Ni	Oop bending of C-H	698.6 760.3 795.1 829.8	128.2 65.4 51.6 42.7	69 ~ 87 and 103.5 ~ 122.5
	Ring skeletal vib.	1455.0 1493.6 1605.5	83.4 73.2 61.1	
AD11	Ring skeletal vib.	1605.5	67.1	65 ~ 81 and 98 ~ 132
	C≡N stretching	2238.5	67.7	
AD11-Ni	Ring skeletal vib.	1605.5	65.8	68 ~ 84.5 and 106 ~ 126
	C≡N stretching	2240.5	66.1	

* Take the absorption peak of stretching vibration of saturated C-H bond at 2927-2933 cm^{-1} as the benchmark (100%). ** oop = our-of-plane (i.e. benzene ring ring).

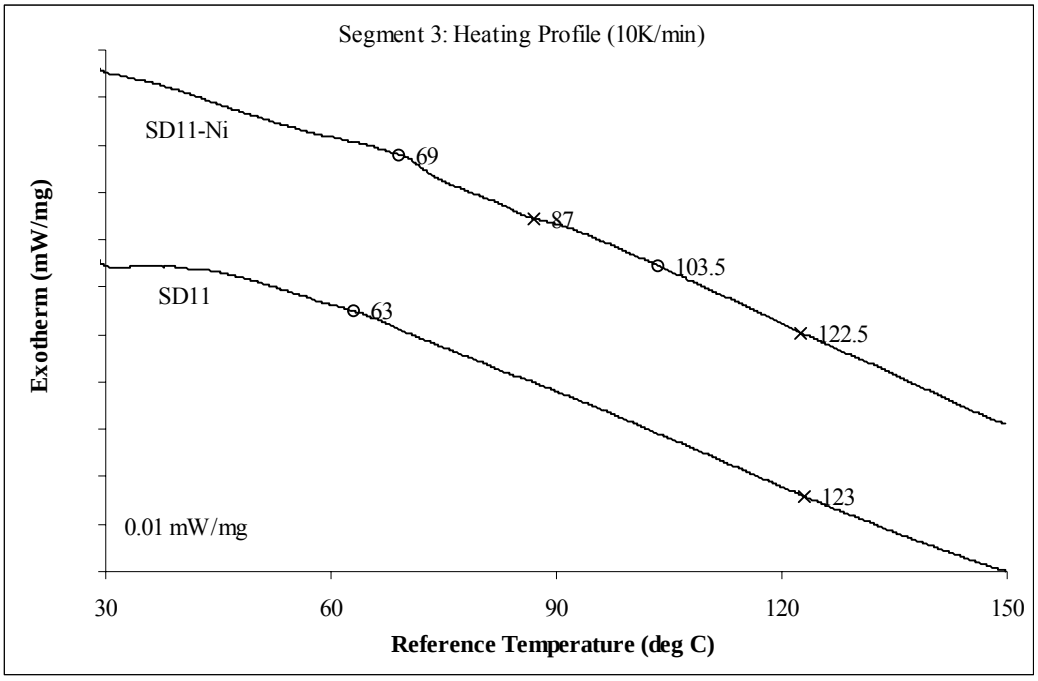

Figure 4.2.19 Effect of the Ni nanoparticles deposition on the thermal transition behavior of SD11 microspheres

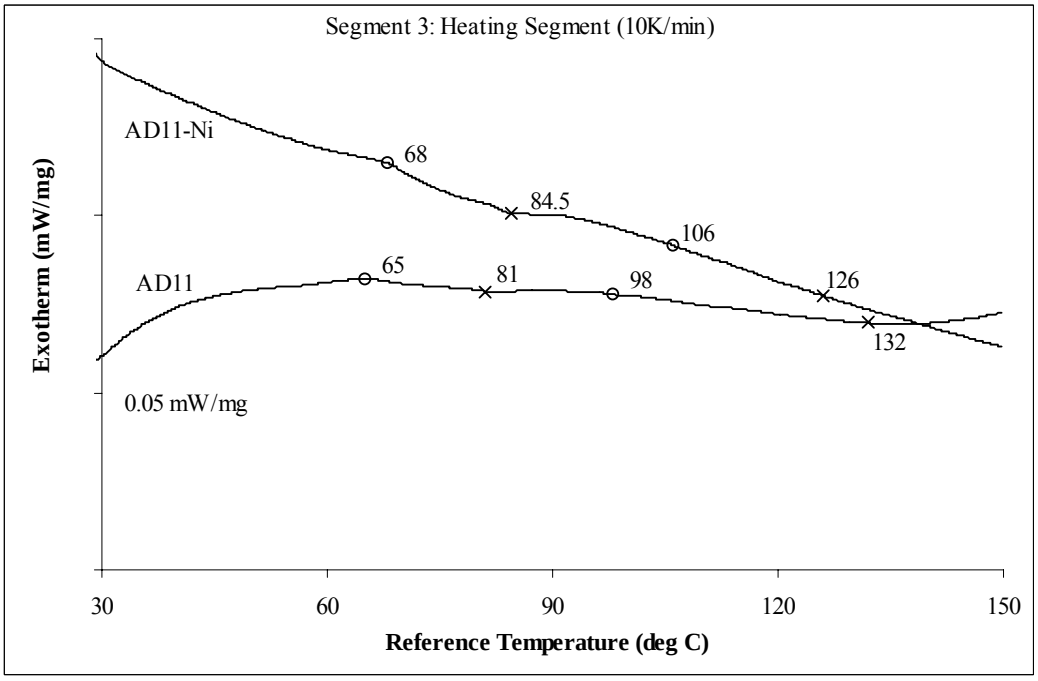

Figure 4.2.20 Effect of the Ni nanoparticles deposition on the thermal transition behavior of AD11 microspheres

In view of the low-frequency attenuation performance of the disk composed of Ni-nanoparticle embedded polymer microspheres, three groups of samples were studied (Figure 4.2.21, 4.2.22 and 4.2.23). The SD11-Ni and AD11-Ni exhibited rather similar responses to the change of frequency as their pristine counterparts revealed: they showed poorer attenuation capability than their non-Ni-loaded counterparts in the range below 250 Hz likely due to possessing less rigid matrixes (found by the IR and DSC characterizations). In equation 4.2.7, the ϕ_v plays the leading role in damping sound amplitude in the low frequency range, and therefore the matrixes of both SD11-Ni and AD11-Ni could be considered to have a lower ϕ_v than SD11 and AD11 did in this frequency range. This proves in turn that SD11 and AD11 possess higher rigidity. The relative softness brought about by implanting Ni particles into these two polymer matrixes could explain the broadening of their attenuation profiles when incident sound waves went up beyond 250 Hz, which is presumed to generate from small fluctuations of the intra-particle pore sizes as well as the matrix pores sizes, and consecutively the damping action due to viscous air-flow in meso-sized channels responded to the frequency change in a relaxation manner.

As a result, SD11-Ni and AD11-Ni reached the maximum sound attenuation (at c.a. 450 Hz) behind SD11 and AD11 (at around 300 Hz). The divergence between the pristine and Ni-embedded disks in damping sound amplitude in 420-700 Hz was primarily due to the effect of pore-flow dissipation since the Ni nanoparticles instigated a loose matrix. On the contrary, SDH11-Ni revealed an attenuation profile which was rather similar to SDH11; it implied that Ni nanoparticle might not intervene with the polymer-polymer interaction sustained by the hydrogen bonding between the hydroxyl groups of HEA units. However, SDH11-Ni still displayed small superiority

over SDH in the frequency range of 420-700 Hz. The Ni-nanoparticles scattering incident sound waves accounted for this damping effect.

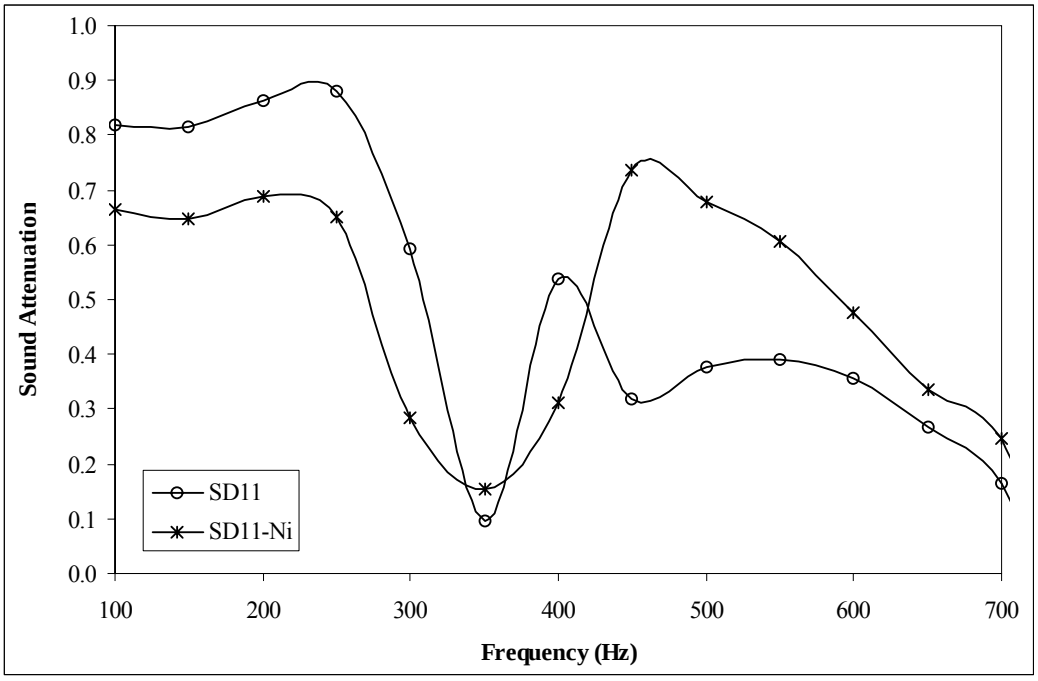

Figure 4.2.21 Comparison of sound attenuation behaviors of SD11 series at low frequency (100-700 Hz) for the studies of the metallic effect

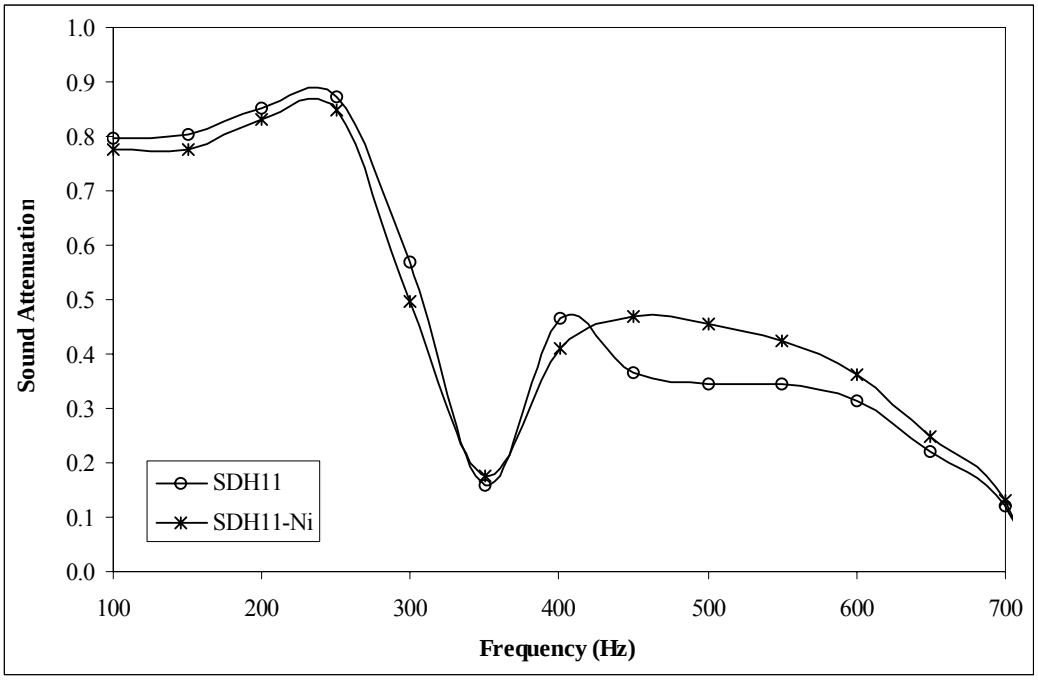

Figure 4.2.22 Comparison of sound attenuation behaviors of SDH11 series at low frequency (100-700 Hz) for the studies of the metallic effect

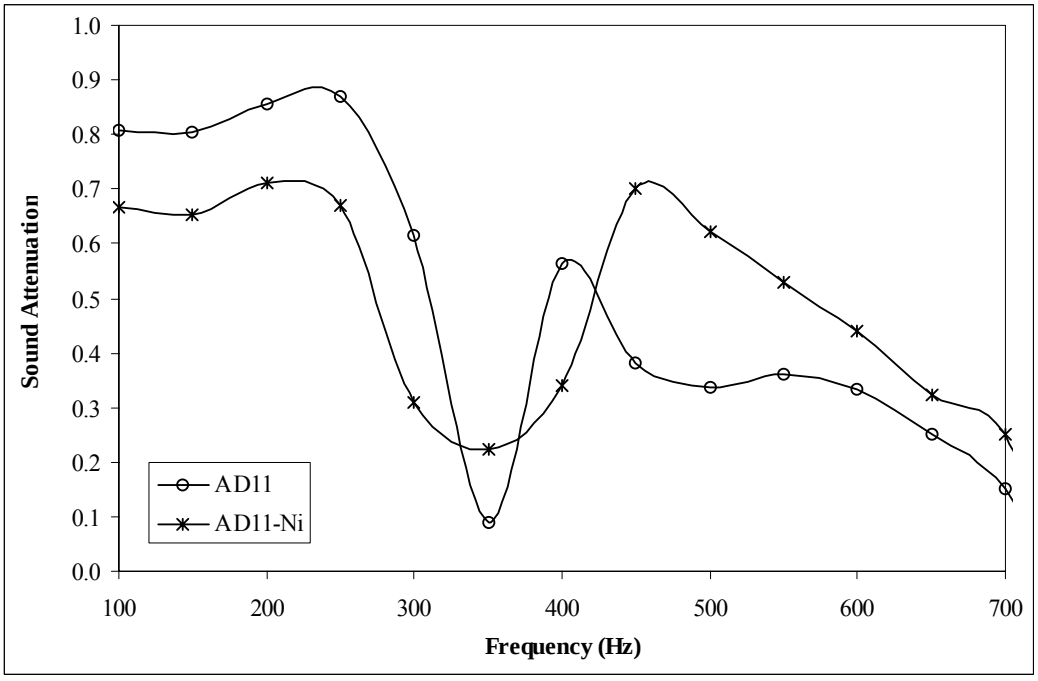

Figure 4.2.23 Comparison of sound attenuation behaviors of AD11 series at low frequency (100-700 Hz) for the studies of the metallic effect

As far as the high frequency range is concerned, as pointed out above, the porosity of the pristine polymer disks could offer only rather limited effects on the sound attenuation. In the same way, the implantation of Ni nanoparticles on porous microspheres of the three series of polymer networks could not lead to noticeable differentiations as well (Figure 4.2.24, 4.2.25 and 4.2.26). Further inspect the sound attenuation profiles of the SD11 and SDH11 series, the latter was found to achieve greater improvement of noise damping with the inclusion of Ni nanoparticles. This enhancement can be only ranked with respect to its pristine counterpart, as shown in Figure 4.2.24 and 4.2.25. The larger gaps found between curve-SDH11 and SDH11-Ni signifies that this series may be viable for more uniform nickel loadings. The random crossover between the response curves (for pristine and metallized samples) prompted that the microscopic air cavity and Ni nanoparticles inclusions act competitively as the wave scatters for the high-frequency incident sound, in addition to the aforementioned intrinsic vibration mechanism and the flow-related dissipative effect.

Pursuant to the above conclusion the main role of Ni nanoparticles was to enhance visco-component of the polymer network though they could also re-radiate part of incident sound waves and result in destructive interference. In contrast, high frequency sound waves promote elastic-component of the polymer network, canceling out the effect of Ni particles.

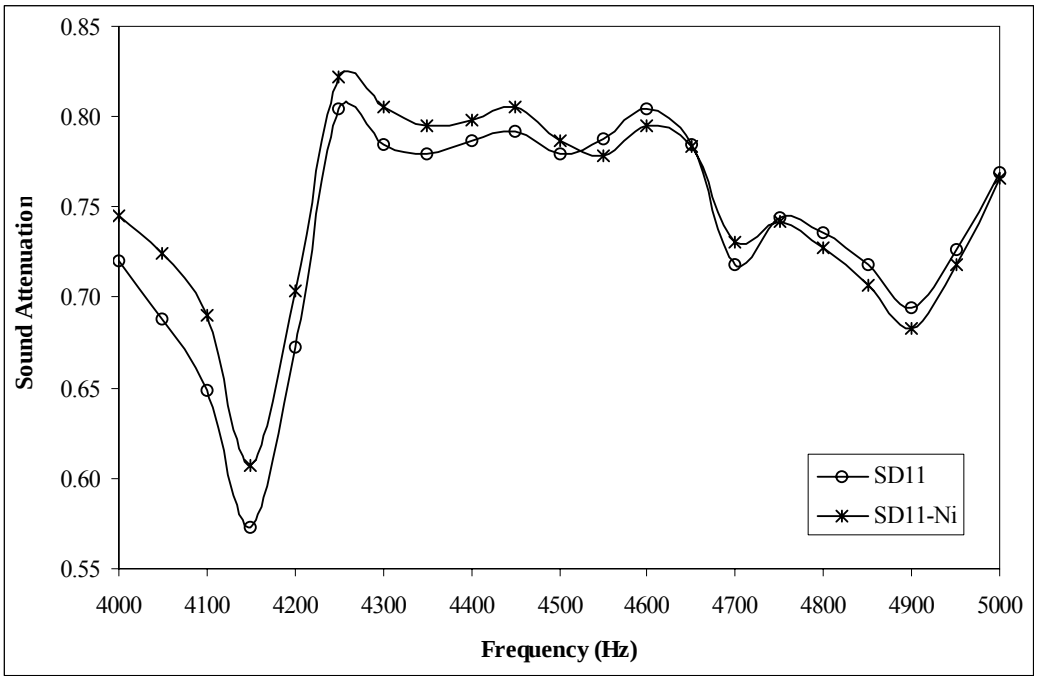

Figure 4.2.24 Comparison of sound attenuation behaviors of SD11 series at high frequency (4000-5000 Hz) for the studies of the metallic effect

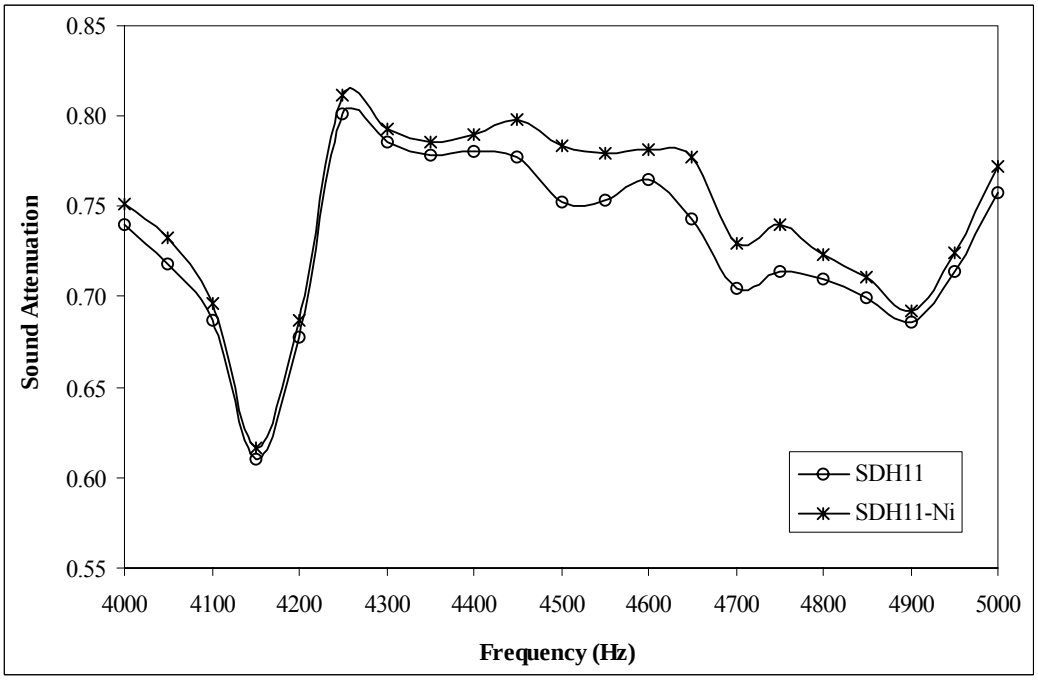

Figure 4.2.25 Comparison of sound attenuation behaviors of SDH11 series at high frequency (4000-5000 Hz) for the studies of the metallic effect

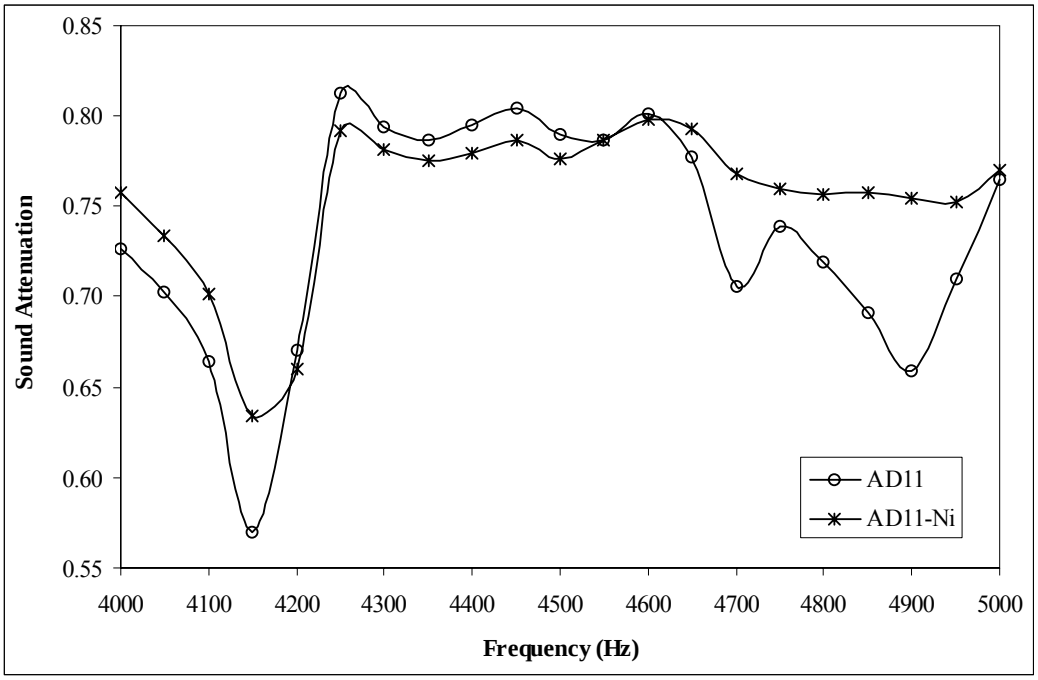

Figure 4.2.26 Comparison of sound attenuation behaviors of AD11 series at high frequency (4000-5000 Hz) for the studies of the metallic effect

4.3 Characterization of Semi-IPN Composed of Poly(styrene-co-divinylbenzene) Network and Linear Poly(ethyl acrylate)

Executive Summary

This section proposes a specific microsphere structure that combines the elastic porous network and the soft polymer chain together in an individual microsphere via polymerizing ethyl acrylate (EA) inside the pores of SD particles. The concentration of EA in toluene, which was used to lead EA into the porous SD matrix and as the polymerization medium of EA molecules subsequently, was varied to adjust the amount of poly(ethyl acrylate) (PEA) trapped inside the SD particles. The successful loading of PEA in SD resulted in a semi-interpenetrating composite, which was verified by gravimetric and FT-IR spectroscopy methods. Furthermore, electron micrograph of the PEA-SD microspheres clearly exhibited that PEA resided not on the surface but rather that inside the SD beads. Subsequently, the change in porosities after incorporation of PEA has also been accounted for briefly. The thermal transition behaviors clearly demonstrated the interaction between the PEA and SD, which augment the damping behavior found in semi-IPN normally. Finally, the semi-IPNs were evaluated in terms of sound damping capabilities within 100-700 Hz and 4000-5000 Hz, compared to their pristine and unloaded counterparts.

4.3.1 Effect of EA Feed on the PEA Loading in the Semi-IPN

For the incorporation of linear poly(ethyl acrylate) into the pre-constructed poly(styrene-co-divinylbenzene) network, the SD11 and SD31 were subjected to swelling by the solution of ethyl acrylate monomer in toluene. In order to compare the effect of porosity of the host network in the EA loading process, the same mass of porous SD11 and SD31 microspheres were dispersed and stirred in the solution of

ethyl acrylate in toluene (50% v/v) for 24 hours. After that, the suspension was filtered and the monomer-loaded particles collected were transferred into an aqueous solution containing PVA as the dispersant and followed by heating the mixture for 48 hours under stirring and inert atmosphere to polymerize the trapped EA. The details have been described in Chapter 3.

The loading result was assessed in term of mass increment of the microspheres after the polymerization and solvent extraction process. To investigate how the concentration of EA in the loading solution affected the PEA remained in the beads, SD11 powders were used, and the EA-Toluene mixture was diluted to 10% and 30%. The reaction conditions are tabulated in Table 3.4 (Chapter 3), and the amounts of PEA gained under the different conditions are reported in Table 4.3.1.

Table 4.3.1 The mass gained after introduction of PEA in SD11 and SD31 powders

Symbol	Mass of unloaded SD beads (m_1) (g)	Mass After PEA Loading (m_2) (g)	Mass Increment (m_2 - m_1) (g)	PEA Gain (PEA Mass/Total Mass)*100%
SD11EA10	5.0063	5.6108	0.6045	10.77%
SD11EA30	5.0008	5.5450	0.5442	9.81%
SD11EA50	5.0055	6.4292	1.4237	22.14%
SD31EA50	5.0036	6.9466	1.9430	27.97%

Table 4.3.1 gives the effective (after purification) PEA mass loading after conducting 48 hours of polymerization. Compare with the SD11 series, the initial concentration of 10% and 30% EA resulted in similar PEA loading in the host matrix. This indifference is regarded as the result of competitive swelling between EA and toluene the host

matrix. When toluene content was higher than EA, the matrix of SD was occupied more by molecules of toluene as it is more alike the styrenic unit of SD and thus the major part of EA could polymerized in the intra-particle pores. The PEA molecules formed at these loci were thus much more easily be washed away during the post polymerization purification than those really penetrating through the SD network; the other key factor was the molecular weight of PEA produced, the lower initial concentrations of EA were to yield shorter chains of PEA with fixing other polymerization conditions. The higher EA content would enhance the entering of EA molecules into SD matrix though their swelling ability is weaker than toluene and the generation of longer PEA chains. As a result, the PEA chains were more likely retained by the "hook", i.e. segments that grew in the SD matrix. This was reflected in SD11EA50 sample, in which the final PEA gain was more than 22%. Further increase in PEA (about 28%) happened in more porous SD31 series, this is because the same 50% EA solution, the highly porous beads can adsorb a larger amount of monomer solution.

4.3.2 Characterization of PSTDVB-PEA Semi-IPN by FT-IR Spectroscopy

The FT-IR spectra of SD11EA10 (10.77 wt. %) and SD11EA50 (22.41 wt. %) displayed clearly the presence of PEA inside the matrix of SD11 after purification (Figure 4.3.1 and 4.3.2), and the same IR spectrum SD31EA50 exhibited. Their IR spectra all showed very distinct peaks at 1750-1735 cm^{-1} and 1300-1030 cm^{-1}, correspond to the C=O and C-O stretching vibrations of the ester functional group, respectively (Figure 4.3.1 and 4.3.2).

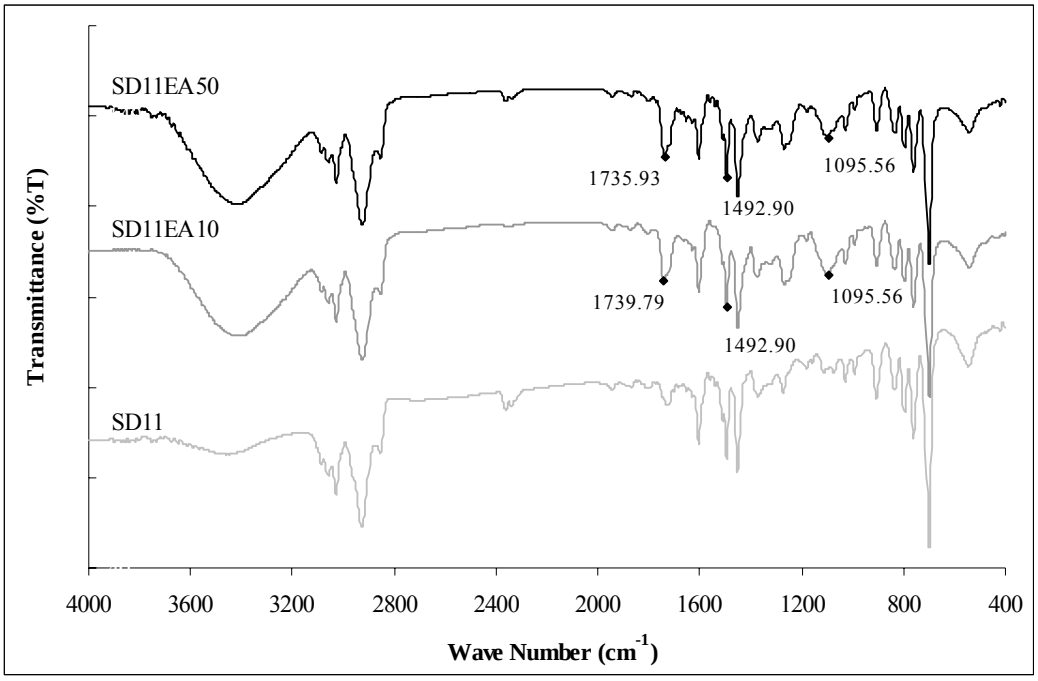

Figure 4.3.1 FT-IR fingerprints for SD series loaded with different amount of PEA

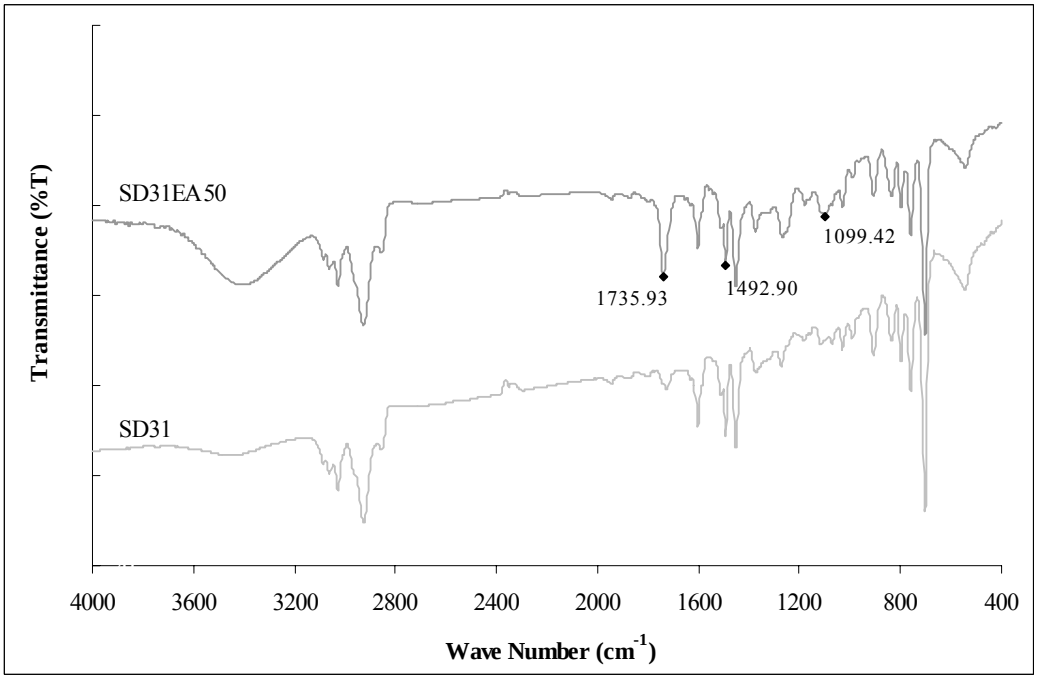

Figure 4.3.2 FT-IR fingerprints for SD31 series loaded with linear PEA segments

4.3.3 Mercury Intrusion Porosimetry for Pore Sizes and Their Distribution

The mercury intrusion porosimetry test for the PEA loaded beads was carried out in the similar procedure as described in Section 4.2. Table 4.3.2 presents the properties obtained from porosimetry measurement. The presence of PEA in SD (SD11EA or SD31EA) caused a drop in both pore area and pore volume. In addition, the decrease is found to be proportional to the amount of PEA loadings, consistent to the results computed in section 4.3.1.

Table 4.3.2 Full intrusion range (0.5-60000 psia) statistical calculation characterizes the bulk properties of the polymer packing within the penetrometer of different PEA Loadings

Sample Symbol	SD11	SD11EA10	SD11EA50	SD31	SD31EA50
(PEA Loading wt. %)	(0.00)	(10.77)	(22.14)	(0.00)	(27.97)
Computed over entire intrusion pressure range (0.5-60000 psia)					
Total Intrusion Volume (ml/g)	1.8114	1.2489	1.1922	2.1451	1.8619
Total Pore Area (m2/g)	114.566	114.74	38.888	131.356	31.28
Average Pore Radius (2V/A) (A)	316	218	613	327	1190
Bulk Density (g/ml)	0.354	0.4556	0.4452	0.3133	0.3465
Apparent (Skeletal) Density (g/ml)	0.9864	1.0573	0.9488	0.9550	0.9767
Porosity (%)	64.1165	56.9056	53.0777	67.199	64.5196
Computed over intrusion pressure larger than breakthrough pressure (500-60000 psia)					
Total Pore Volume (ml/g)	0.5936	0.3274	0.1473	0.7596	0.2661
Total Pore Area (m2/g)	113.7	114.14	38.213	130.149	30.119
Average Microsphere Pore Radius (A)	104	57	77	117	177
Microsphere True Porosity (%)	21.0127	14.9178	6.5575	23.7943	9.2210

The pore size distribution curves plotted in log differential intrusion volume against pore radius are shown in Figure 4.3.3 and 4.3.5. As shown, for SD series (Figure 4.3.3), SD11EA10 (10.77% PEA) exhibit slightly distinct pore distribution compared to the unloaded counterpart. Compare to SD11 curve, the SD11EA10 curve presents a higher distribution in the range 20-60 Å, compensated by the higher pore size, 80-1000 Å. This infers that the low PEA loading process had effectively occupied the larger holes which are more accessible by EA monomers during the loading process. After polymerization, the linear chains have slight entanglement with the SD porous matrix, results in the formation of secondary pores which are smaller in sizes (20-60 Å).

For the higher PEA content (22.14%) as shown in curve-SD11EA50, the pore size distribution profile is flattened, expanding over the range of 30-300 Å. It appears that the insertion of higher PEA amount reduce drastically the pore volume of the SD11 matrix. Moreover, larger amount of bulkier PEA linear chains are capable of blocking the pore radius of less than 30 Å during the polymerization process. Consequently, only larger mesopores are assessable by the mercury intrusion in the resulting beads. The same behavior was found in the comparison of SD31 series, as shown in Figure 4.3.5. In this category, the highest PEA loading (27.97%) enhances the pore filling process, as the pore size distribution curve has been restrained under 60-1000 Å, with much less differential intrusion volume.

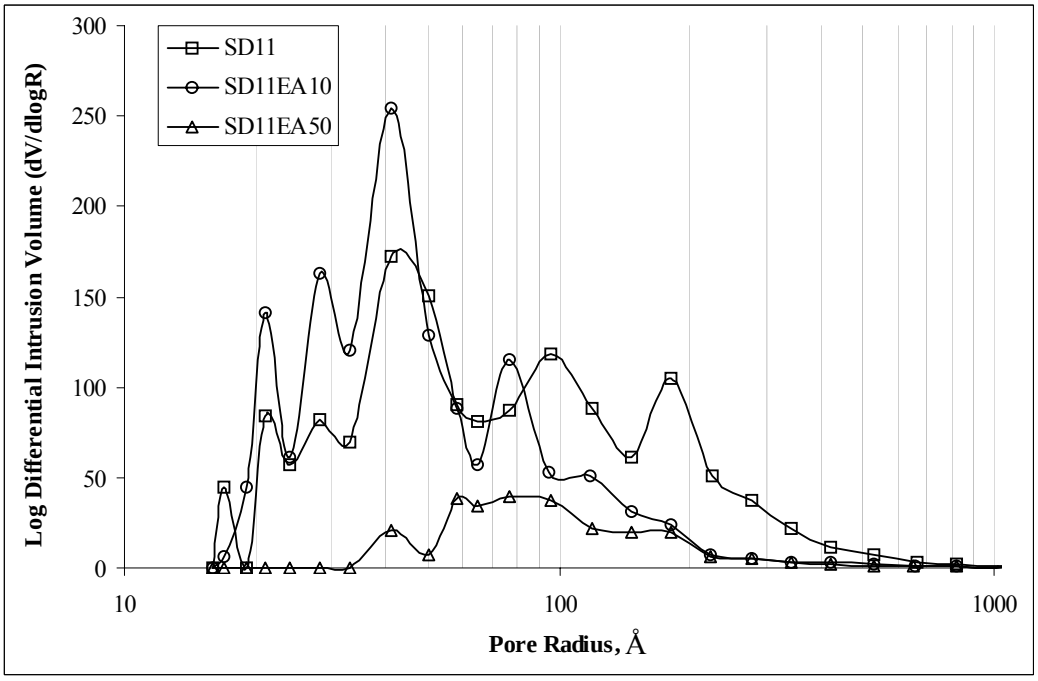

Figure 4.3.3 Log differential intrusion plot of SD11, SD11EA10 and SD11EA50 for the characterization of pore size distributions

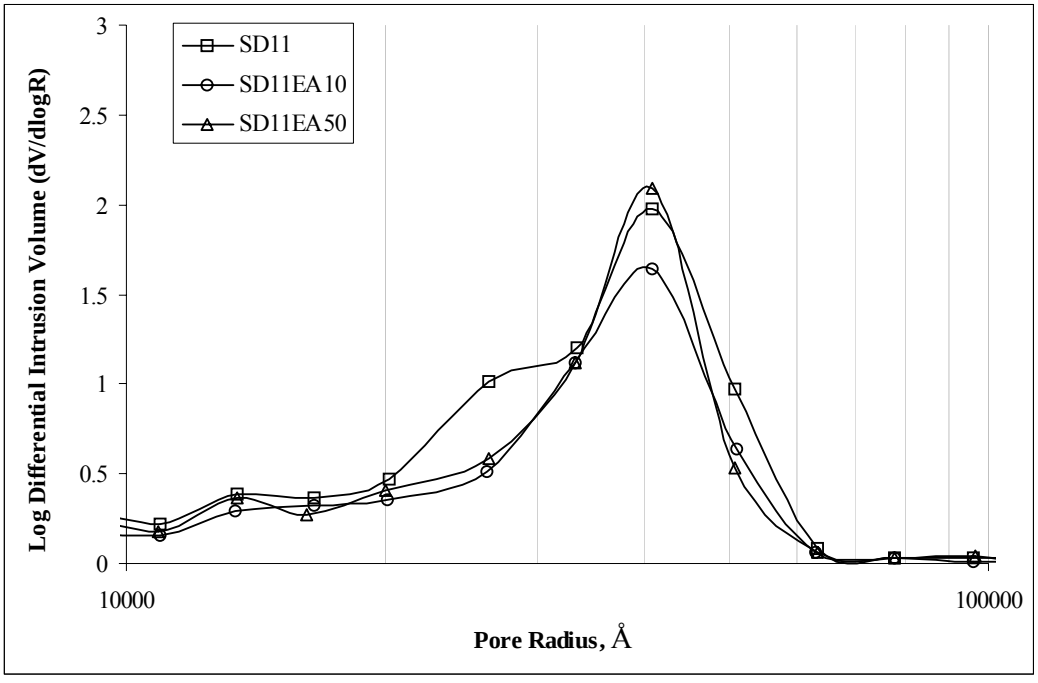

Figure 4.3.4 Log differential intrusion plot of SD11, SD11EA10 and SD11EA50 for the characterization of interstitial voids size distributions

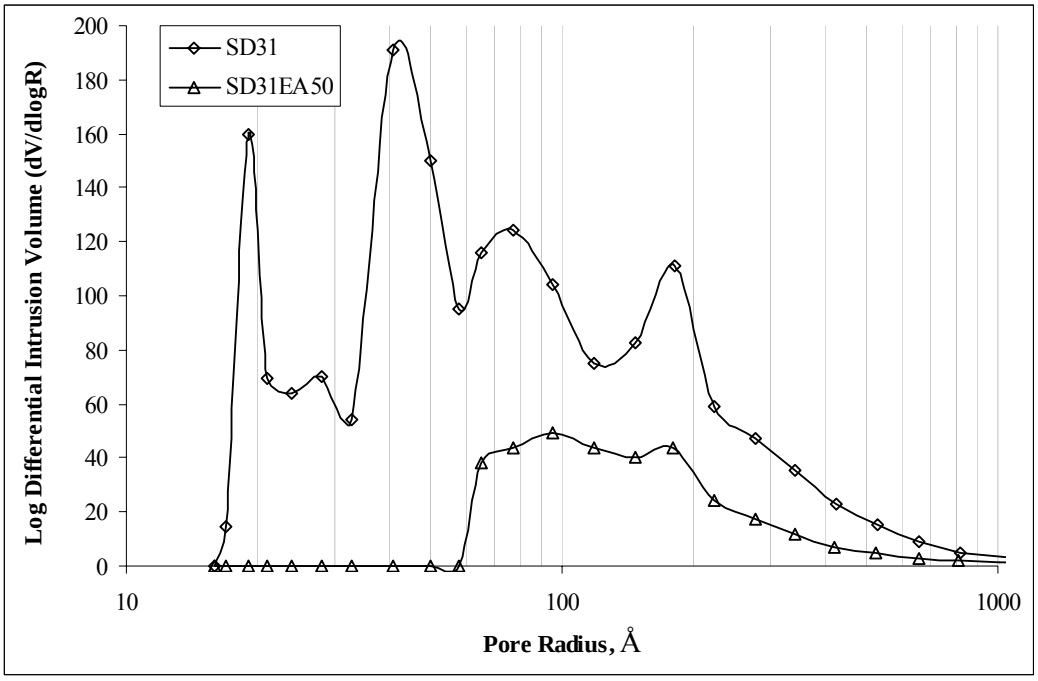

Figure 4.3.5 Log differential intrusion plot of SD31 and SD31EA50 for the characterization of pore size distributions

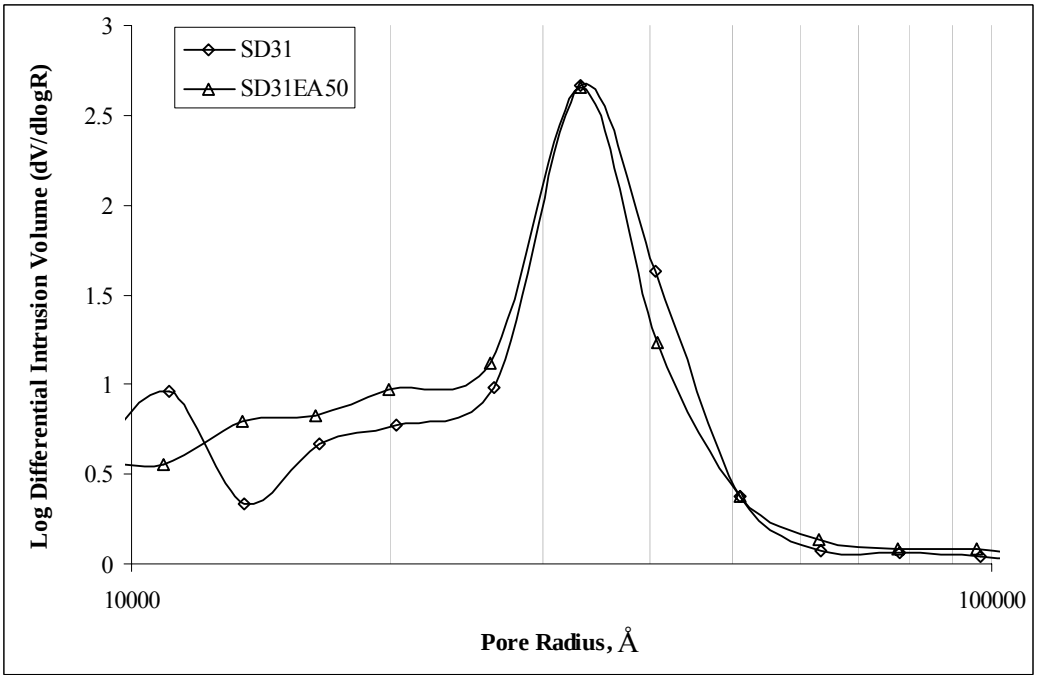

Figure 4.3.6 Log differential intrusion plot of SD31 and SD31EA50 for the characterization of interstitial voids size distributions

Compared with the low pressure or large radius (10000-100000 Å) differential intrusion profile in Figure 4.3.4 and 4.3.6, the effect of PEA loading on interstitial voids of the beads packing was investigated. It appears that the PEA-loaded beads demonstrated exactly the same microsphere packing density as the unloaded one, as the intrusion curves tend to overlap without any shifting. This positive outcome further proved that the PEA insertion had taken place in the porous matrix instead on the surface or exterior part of the SD beads. If the PEA segments had formed an outer soft jacket on the surface of the beads, it could have been observed that an increase in packing density in the time of mercury intrusion analysis.

In summary, formation of PEA inside the porous SD beads was confirmed by the reduction of their mesopore volumes and no any significant change in the inter-particle packing density. Furthermore, higher PEA loading has blocked the matrix pore radius below 30 Å as shown in mercury intrusion characterization.

4.3.4 The Surface Morphology of PEA-SD Semi-IPN Beads

The surface morphology has been investigated by high magnification FE-SEM. Figure 4.3.7 (a-b) presents the micrographs of SD11EA50 surface, at 10,000X and 100,000X, respectively, whereas the SD31EA50 is shown in Figure 4.3.7 (c-d). The lower magnification pictures revealed the morphology which was very similar to the unloaded SD beads (section 4.2). Obviously, SD31 series exhibited more porous surface, even though for highly PEA loaded sample (Figure 4.3.7 d). Besides, there was no separated PEA lumps found to be at the surface of all microspheres. This is a desired feature achieved by the current loading procedure because of very likely the role of PVA, which was used to disperse the EA-loaded microspheres in heating

medium (water) and could also confine the EA molecules inside the pores of particles during vigorous agitation.

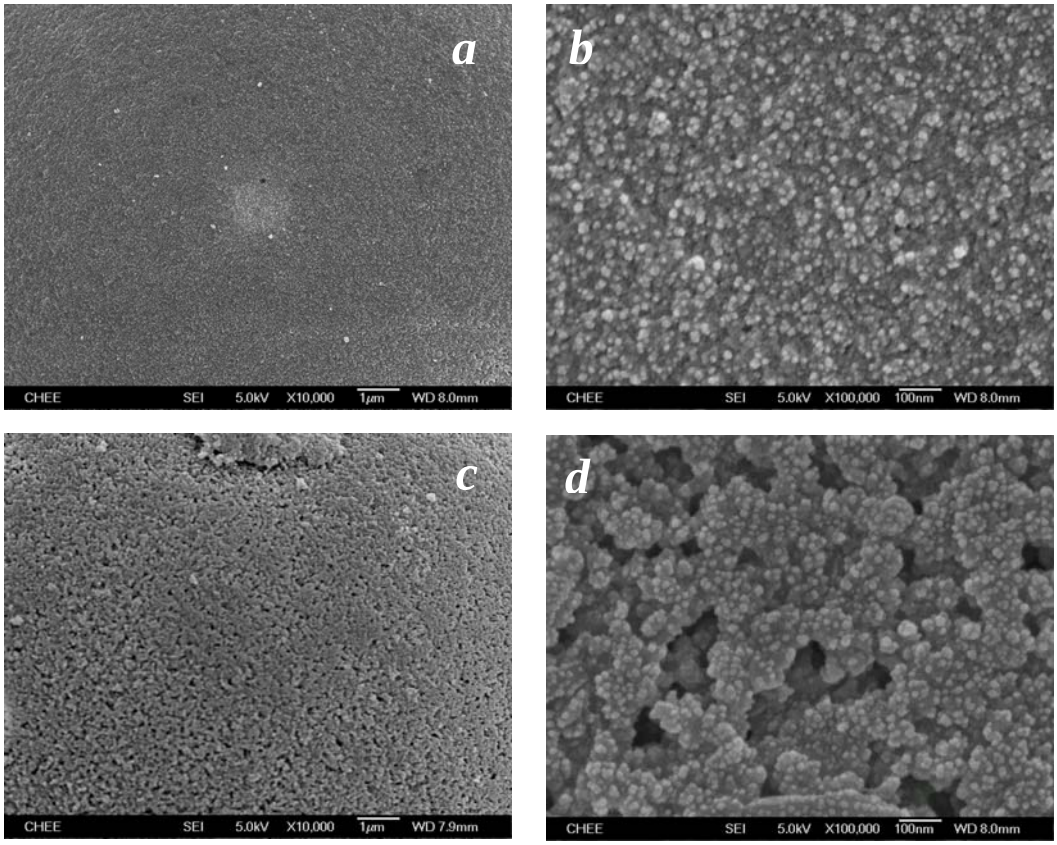

Figure 4.3.7 FE-SEM micrographs of the PEA-PSTDVB semi-IPN microspheres surface morphology (a, b) SD11EA50 and (b, d) SD31EA50 at 10,000X and 100,000X magnifications, respectively

4.3.5 Thermal Behavior of the PEA-SD Semi-IPN

The DSC profiles of the unloaded SD microspheres (SD11) and three types of the semi-IPN beads with different PEA loadings are compared in Figure 4.3.8. The measurement condition was strictly controlled as detailed in experimental section to maintain them in parallel. Typically, determination of the glass transition temperature was based on the second heating segment, the first heating and cooling segments were executed to remove the irregularity among the samples due to the hysteresis or enthalpy relaxation behavior originated from the random nature of the chain entanglements inside the semi-IPN beads. In other words, the thermal history for each sample had been rectified to have the similar level before determining their T_gs.

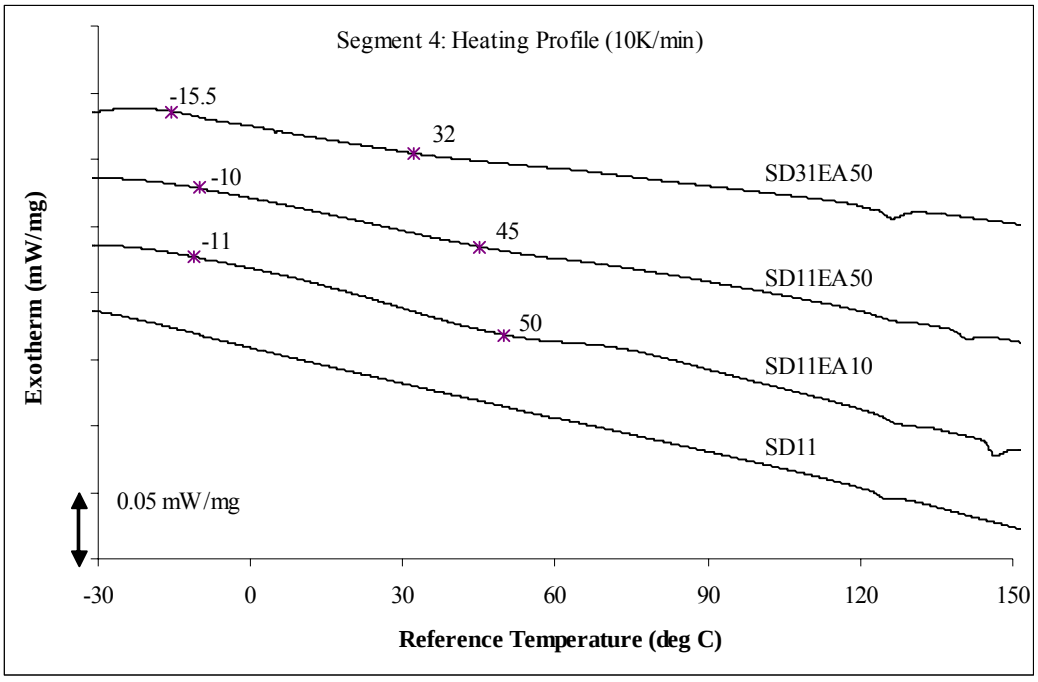

Figure 4.3.8 DSC profiles of the PEA-SD semi interpenetrating network

In contrast to their host counterpart, the PEA-loaded powders demonstrate two distinct thermal transition regions, ca 110~125 ^{o}C and -15~50 ^{o}C. Under similar definition of T_o (onset of glass transition), T_e (ease point of glass transition) and T_g (temperature at which the half of heat capacity is gained) shown in section 4.1, these temperatures were found out graphically and tabulated in Table 4.3.3. The data revealed that the pristine SD11 sample exhibit a glass transition range of 108.5~118 ^{o}C, a typical transition region for crosslinked styrenic network. On the other hand, the incorporation linear PEA into SD matrix had brought about a new glass transition region which was well located within ambient temperature region. As reported in literature (Andrews et al., 1999), the linear PEA has the T_g range between -25 and -22 ^{o}C. In a highly cross-linked porous SD network, heavy physical entanglements and physical cross-linking between the different segments of inserted PEA chains and more rigid SD network were inevitable. Hence the end-chain fixation effect and the intermolecular chains intertwine accounted for the thermal transition behaviors, which were similar to the chemically crosslinked PMADVB microspheres, shown in section 4.1.

Table 4.3.3 DSC results for the pristine and the PEA-loaded PSTDVB microspheres

Sample	Transition	T_o (^{o}C)	T_g (^{o}C)	T_e (^{o}C)	T_g Width (^{o}C)	ΔCp (J.g^{-1}.K^{-1})
SD11	1	-	-	-	-	-
	2	108.5	112	118	9.5	0.013
SD11EA10	1	-11	25	50	61	0.093
	2	112.5	124.2	127	14.5	0.031
SD11EA50	1	-10	21	45	55	0.031
	2	115.5	122.5	126.5	11	0.021
SD31EA50	1	-15.5	3.5	32	47.5	0.037
	2	111.5	119.5	121.5	10	0.019

Further inspecting the DSC profiles, it could be found that the glass transition region shifted towards lower temperature ranges when the PEA mass loading was increased. This trend turned out to be more obvious in SD31EA50-curve, in which the PEA loading was about 27.97%. The increase in the loading of PEA in bigger pores would lead to formation of tiny PEA bulk phases that resemble to pristine PEA than those entrapped in SD network; hence these rubbery PEA tiny domains lower down the apparent T_g. Secondly, SD31 beads are more accessible to the heat radiation from the surroundings, due to higher surface porosity and larger pore volume. Under similar heating rate, the trapped PEA segments will be more easily heated and relaxed in comparison with SD11EA series. Hence, lower onset and endset of T_g had been observed.

Within SD11 series, lower EA loading (SD11EA10, 10.77%) gave a wider glass transition range, ca. -11~50 ^{o}C, compared with SD11EA50. The lower PEA loading corresponded to more interfacial PEA phase within the rigid SD11 matrix. Upon heating, the two locations (namely bulk phase and interphase) responded in different manner due to difference in heat capacity and expandability. The larger free volume found in this sample can enhance a more coordinated motions of the polymer composite as the steric hindrance can be minimized. Thus, the glass transition range for SD11EA10 is expanded.

Similar to unloaded SD beads, the PEA-SD semi-IPNs displayed second glass transition region in the higher temperature direction, due to the contribution of highly crosslinked SD network. Under the observed transition behaviors, it is possible to expand the glass transition region by overlapping the low and higher transition region.

This can be done by keeping the PEA loading in low enough level while reducing the nominal crosslinking degree of the PSTDVB network. Further experiments need to be done to justify the prediction. However, the processes will involve drastic change in porosity of the matrix, the loading capacity and the large number of complications.

4.3.6 Characteristic Attenuation Behavior in Low Frequency Range

When the incident sound frequency band (100-700 Hz) was set to test the disks made up of three types of SD11 powders (pristine one and the PEA-loaded counterparts), the three corresponding profiles signaled by different attenuation coefficients were obtained (Figure 4.3.9). In light of the attenuation profile across the frequency scanning range, as addressed in the previous sections, it was affected largely by resonances of the testing tube, while the frequency-dependent sound absorption of the sample disks fluctuated only in a much narrower range relative to amplitude oscillations at resonances.

Similar to the attenuation behaviors found for pristine SD series with distinct porosities (Section 4.2.6), the sound attenuation coefficients for this group increase slightly with increasing frequency up to 250 Hz. Their magnitudes displayed in this very low frequency range demonstrated that the pore-flow-related dissipative effect outweighed over the intrinsic-vibration-bound one. Due to the analogous packing density and the similar interstitial voids distribution for all the SD11 samples, the sound attenuation curves tend to overlap. This behavior prompts that the pore dissipative effect happened indeed predominantly in the interstitial spaces.

In the above lower frequency range, the attenuation effect (i.e. the vertical position of the profiles) could be attributed to meso-cavity dissipative action. The porosimetric studies revealed that sample SD11EA10 is more abundant with mesopores (especially in the range of 20-60 Å), a result of filling PEA in larger pores ranging from size 80-1000 Å. Also, the higher PEA loading in SD11EA50 maintained a majority distribution in the mesopore range, the damping effect of which was however offset by a drastic reduce in specific pore volume. The low frequency attenuation responses exhibit the following trend:

SD11EA10 > SD11 > SD11EA50

This is consistent with the fact found in previous section, that is, the introduction of additional dissipative effect due to frictions of flow at air-polymer inter-phase is originated by the existence of meso air cavities. In this way, a larger specific pore volume offered more obvious pore-flow dissipative effect.

The gap of sound attenuating capability between SD31 and SD31EA50 was greater below 450 Hz with reference to the corresponding difference happening in SD11 series (Figure 4.3.10). This is due to the greater extent of decreases in both the meso cavities distribution and the specific pore volume in sample SD31EA50 (shown in Figure 4.3.5 and Table 4.3.2). With the insertion of linear PEA, the surface of SD31EA50 beads was found to be smoother compared to the pristine SD31, microscopically. This provided less interparticles flow resistance to the incidental acoustical waves, for which the conversion of mechanical energy to heat energy was facilitated by rougher SD31 surface.

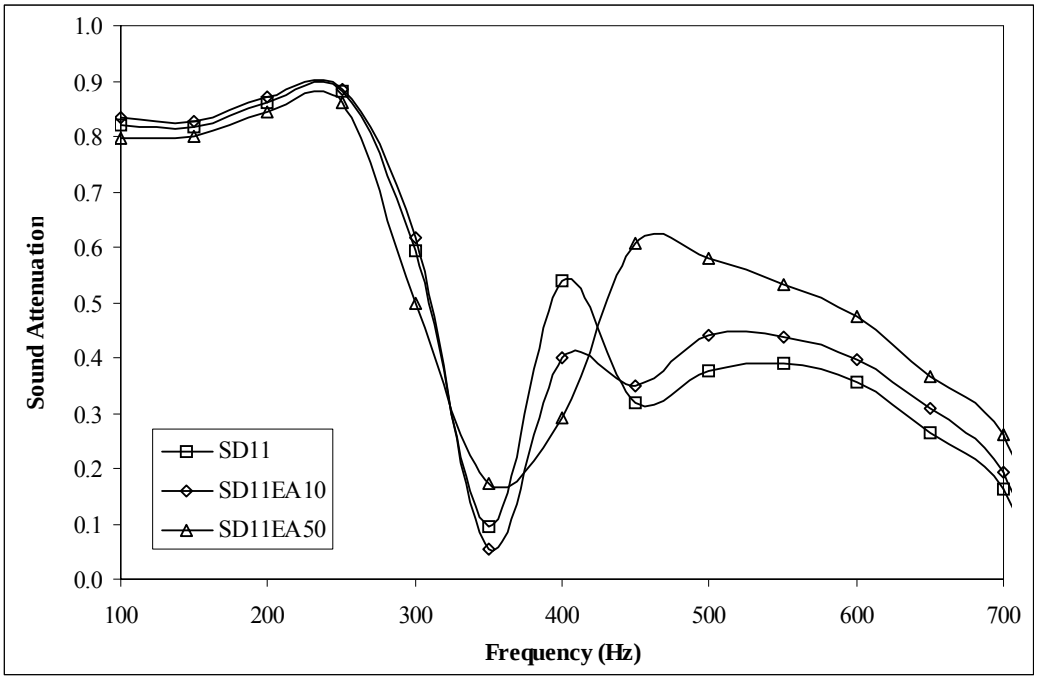

Figure 4.3.9 Sound attenuation behaviors of SD11 series semi-IPN at low frequency

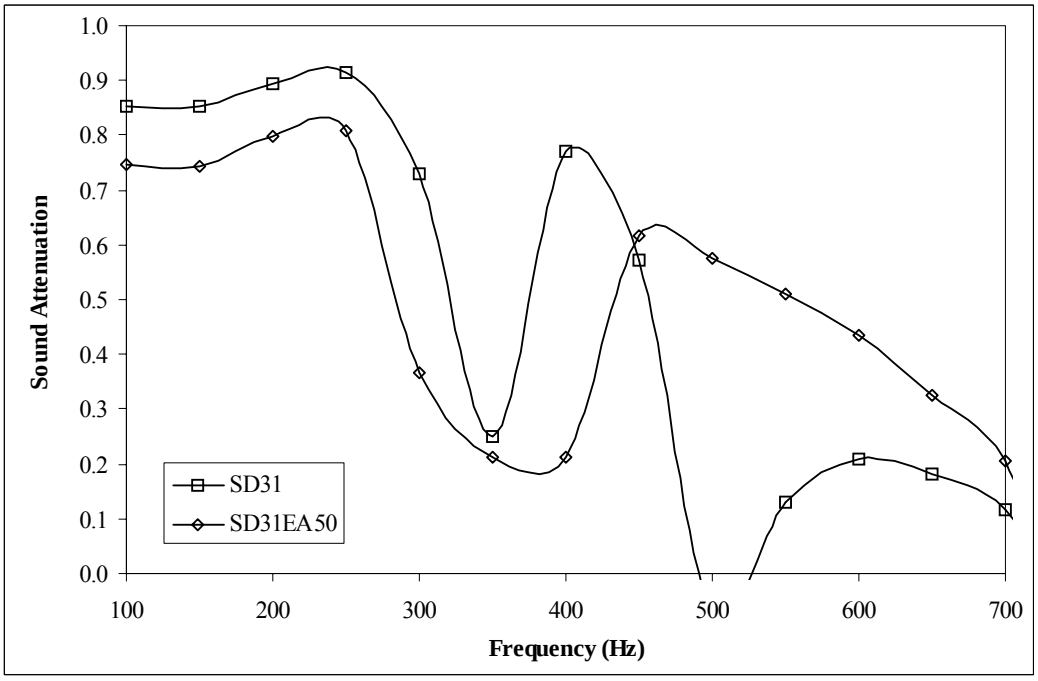

Figure 4.3.10 Sound attenuation behaviors of SD31 series semi-IPN at low frequency

In view of the higher frequency range after the resonance frequency (c.a. 450-700 Hz), the presence of PEA in the porous matrix of both SD11 and SD31 series played a role in enhancing the attenuation. It is deemed that the tiny domain of the PEA deposited in bigger pores was responsible to the raise of damping capability because the T_g range of PEA tiny phase was to shift up to ambient temperature direction with increasing the frequency, and as a result, the span of the loss tangent curve would also increase. The deformation and relaxation of the PEA domain in response to the incidental acoustic vibration converted the mechanical energy to heat energy. The other pushing effect is the inscribing of PEA domain in rigid SD matrix, this special physical environment helped to move the glass transition temperature of PEA towards ambient temperature as shown in Table 4.3.3.

4.3.7 Characteristic Attenuation Behavior in High Frequency Range

In the relatively high frequency (4000-5000 Hz) sound field, the conversion of the longitudinal deformation of air into the shear deformation (relative segment motions) of the polymer network has reached the saturation limit, which means that the damping behaviors of inserted PEA phase play the dominant role for any enhanced attenuation. Inspecting the sound attenuation curves, plotted in measured transmitted sound level (dB) against frequency, as illustrated in Figure 4.3.11 and 4.3.12, the semi-IPN showed a clear right-shifting of the response curves with respect to SD substrates. Here, the control curve was the sound level profile generated without the installation of testing disk. The time-temperature superposition principle of dynamic mechanical spectrum (DMS) infers an equivalent left-shift of the curve if plotted in temperature scale (Jones, 2001). Qualitatively, the effect of frequency is the inverse of the effect of temperature, increasing frequency being similar to the effect of decreasing temperature

at different rates. This is an indirect proof for a decrease in the glass transition temperature of whole absorbent resulted by the incorporation of linear PEA chain.

Compared with porous SD microspheres, the semi-IPN microspheres (SD11EA or SD31EA series) can apparently relax the incident frequency, especially the higher-frequency end; the high frequency sound wave promoting the elastic-component of the PEA might assist this relaxation process. A characteristic feature of PEA viscoelastic response is the phase lag between the strain and the applied stress, due to the loss mechanisms. It has been suggested that the origin of the phase lag in absorption is in the time delay of reorienting the polymer among the large number of metastable equilibrium positions possible. The damping behavior of the inscribed PEA domains can be more clearly reflected when the sound attenuation coefficient as a function of frequency is plotted, as shown in Figure 4.3.13 and 4.3.14. Here, the incorporation of PEA chains displays superiority of sound damping at two distinct frequency ranges, namely 4250-4500 Hz and 4700-5000 Hz. The maximum attenuation level (α) was about 80% (dB). It was also found that increasing PEA loading could improve rather limit the attenuation level in the higher frequency range.

The positive feature for attenuation enhancement in higher frequency range is important in noise control technology. The long-time exposure to human hearing to higher audio frequency is much susceptible to permanent hearing impairment if the exposure level is accompanied by substantial sound intensity. Knowing that the structure modification based on incorporation of tiny inclusion (e.g. metal particles discussion in Section 4.2) provide extra scattering mechanism to scavenge the incidental acoustic wave, the sound attenuation enhancement is very tiny compared to

intrinsic absorption. Here, we predict that by carefully control the rheological and thermal transition behavior of semi-IPN, it is possible to shift and to expand the applicable sound attenuation range.

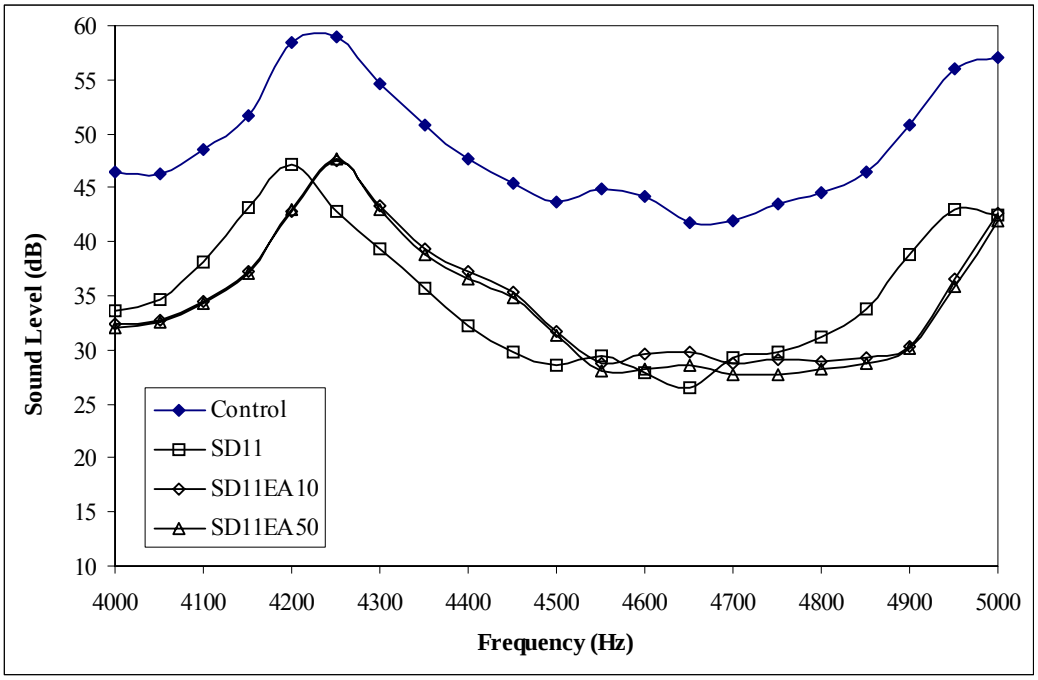

Figure 4.3.11 Sound attenuation behaviors of SD11 series semi-IPN at high frequency (Sound Level vs. Frequency)

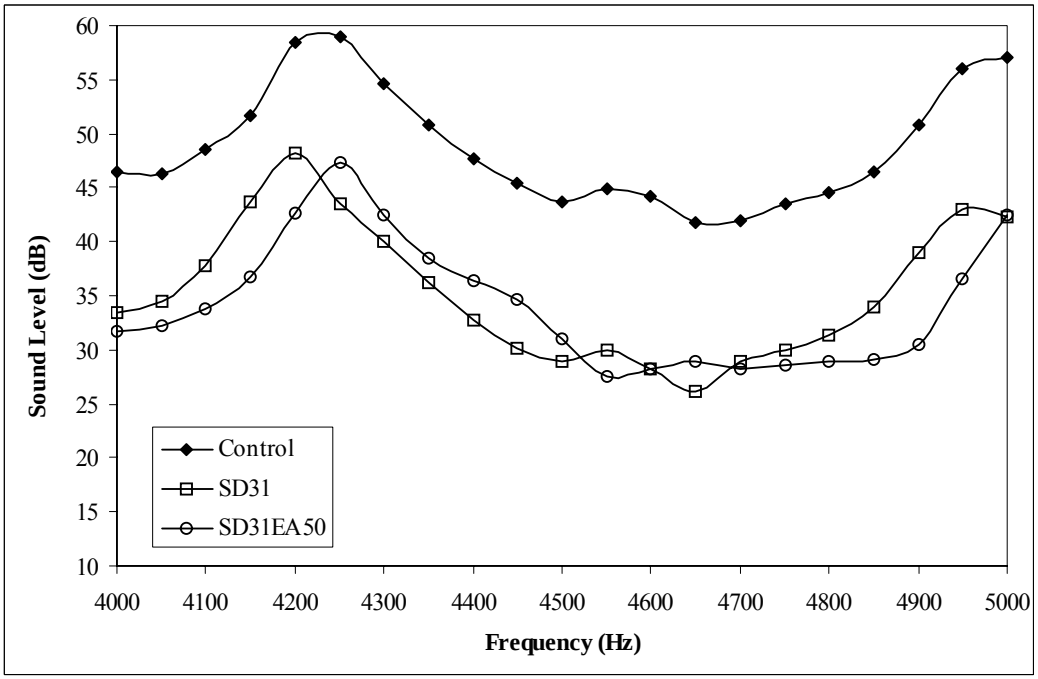

Figure 4.3.12 Sound attenuation behaviors of SD31 series semi-IPN at high frequency (Sound Level vs. Frequency)

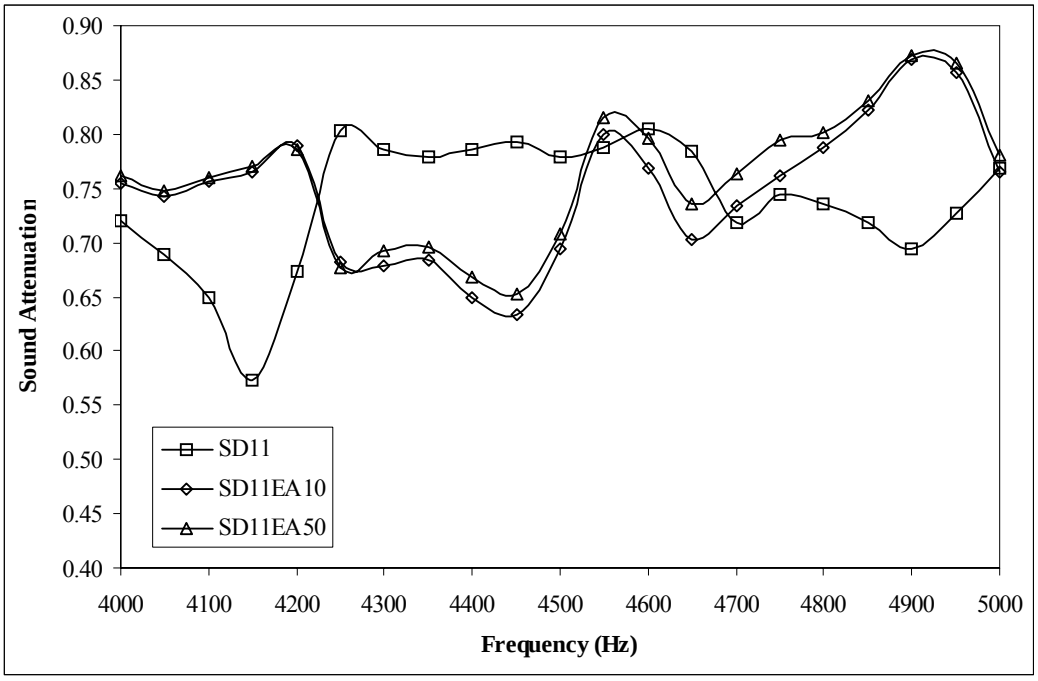

Figure 4.3.13 Sound attenuation behaviors of SD11 series semi-IPN at high frequency (Sound Attenuation vs. Frequency)

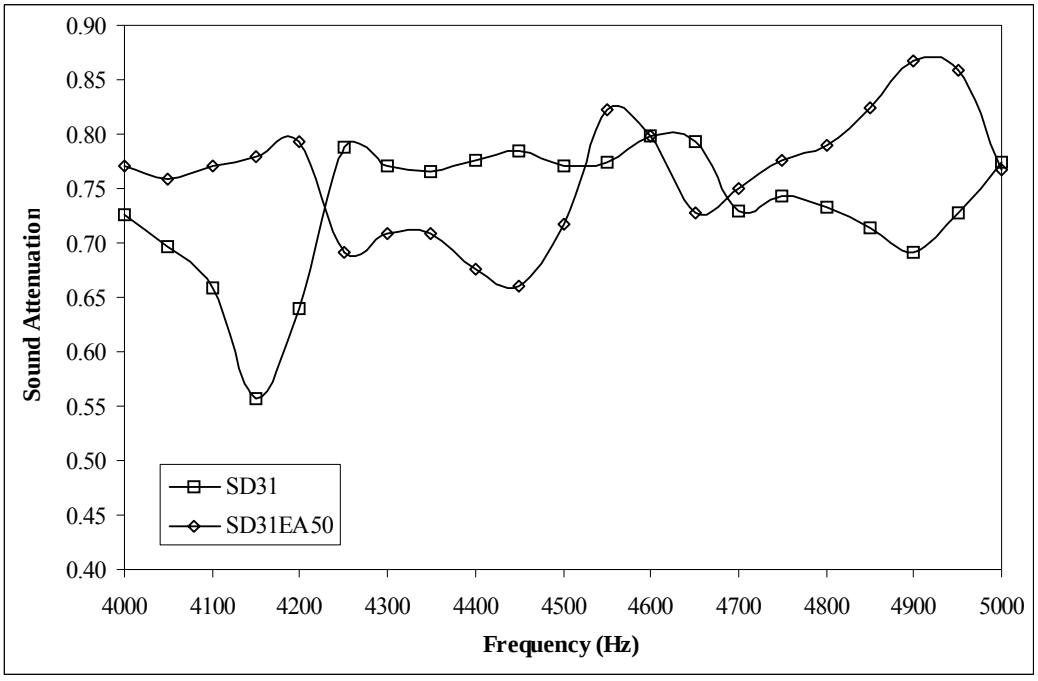

Figure 4.3.14 Sound attenuation behaviors of SD31 series semi-IPN at high frequency (Sound Attenuation vs. Frequency)

Chapter 5

Conclusions

The linear segment of poly(methyl acrylate-co-divinylbenzene) (PMADVB) network in microspheres (50-100 μm, $\overline{d}$ = 66 μm) exhibits a glass transition temperature range that is apparently higher than linear PMA homopolymer. Deposition of a thin Ni-P alloy layer on the PMADVB bead by means of electroless plating could expand the glass transition range depending upon the thickness of metal layer, which could be attained approximately up to 1~2 μm by setting different plating temperatures but fixing plating duration. This unique effect is attributed to the establishment of a spherical temperature field within each individual polymer bead because of a Ni-P deposition layer. In the sinusoidal acoustic waves (100-1000 Hz) and ultrasonic wave (35 kHz) attenuation studies, the Ni-P layer played a role in facilitating the reduction of acoustic power that enter the detector or probing system. This function is ascribed to the metal-assisted concert motions of polymer segments, in addition, wave-scattering at the sub-micron metallic-grains of which the metal deposition layer was formed accounts also for the wave attenuation.

In the porous microspheres (<50 μm, SD, SDH and AD series), the porosity and pore size distribution can be easily controlled by introducing a porogen (a mixture of decane/toluene) into the suspension polymerization system. Implantation of nano-sized Ni particles (d<100 nm) onto the surface of these microspheres (c.a. 0.5 wt %) via the in-situ chemical reduction approach could exert a significant influence on the packing density of polymer matrix, depending upon affinity of the pendant function groups with Ni(0) atom, flexibility of the free segments, distribution of crosslinking points

and surface states of Ni particles. A simplified theoretical model addressing the impact of membrane intrinsic vibration and the wave viscous pore-flow to the attenuation of low frequency sound waves was established. For the rigid elastic part of the porous medium, the acoustic attenuation can be accomplished by the existence of a temperature gradient layer adjacent to the wall, which converts mechanical energy to heat as well as by the destructive interference between incident and scattered sound waves, which is triggered by the elastic deformation of air micro-bubbles in tiny voids of porous medium. For the viscoelastic constituent, the intrinsic polymer segment motions convert sound energy into potential energy or heat by mode-conversion mechanism. Two particular audio frequency bands of the incident acoustic waves, 100-700 Hz and 4000-5000 Hz, were designated to examine the sound absorption behaviors of the samples. The percentage of meso-pores (diameter 20~40 nm) was identified to be responsive in dissipating the low audio frequency band but became dull to the high frequency band. Furthermore, the inclusion of the Ni particles gave rise to a promotion to the attenuation coefficient in the frequency range of 420-700 Hz but negligible effect on the high audio frequency band.

With the semi-IPN structure constructed by weaving in porous SD network the linear poly(ethyl acrylate) chains is concerned, such a structure combines the elastic porous network and the viscous polymer chain together in an individual microsphere. Due to the end-chain fixation effect and the intermolecular chains intertwine between linear PEA and heavily crosslinked SD network, the DSC studies revealed that the incorporation linear PEA into SD matrix had brought about a new glass transition region which embraces the ambient temperature, and is much higher than the T_g of pristine linear PEA (-25~-22 ^{o}C). In the acoustic absorption test, the semi-IPNs beads

display similar dependence of frequency and pore sizes on sound attenuation coefficient at 100-400 Hz. The presence of PEA in the porous matrix of both SD11 and SD31 series played a role in enhancing the attenuation at 450-700 Hz, due to the tiny deposited PEA domain, responsible to shift the T_g region up to ambient temperature, to expand the span of loss tangent curve and hence to raise damping capability. Compared with porous SD microspheres, PEA-SD microspheres could apparently relax the incident frequency, and the magnitude of which became large in the higher frequency sound range, and attenuate the higher frequency sound waves more effectively up to maximum attenuation level of 80% (dB). It was found that increasing PEA loading could improve rather limit the attenuation level in the higher frequency range.

Finally, we anticipate several opportunities for the improvement of this research:

- The assessment of ultrasound attenuation by indirect biomass adsorption can be replaced by direct measurement method. This is realized by constructing a larger-sized concentric adsorption chamber, with the installation of needle-shaped hydrophone in various location of the chamber, in order to measure the intensity of the ultrasonic wave locally and directly. It is also desirable to employ a tunable source of ultrasonic wave; however the facility is not yet available in lab-scale ultrasonic cleaner.
- For the acoustic wave studies, the current design have not properly circumvent with the geometric resonance problem of the cylindrical testing tube. This could be improved by utilizing a duct with variable (gradually increase) cross sectional area, to prevent the internal reflections that amplify substantial acoustic power over minor frequency distortion, especially in the vicinity of duct resonance frequency.

- In this research, the simplified measurement method is only able to compute for a lumped parameter, which accounts for both absorption coefficient and transmission loss simultaneously. The attenuation coefficient computed by the present method is only an approximation, as the standard impedance tube method (ISO 10534-1, ASTM C384-98, ISO 10534-2 and ASTM E1050) can accurately measure and calculate transmission loss and absorption coefficients directly by capturing the transmitted and reflected sound intensity using various detectors in one experiment. The method is nevertheless less cost-effective, as it involves installation of multiple condenser microphone, stringent sound level calibration and robust analyzer for the computation of standing wave ratio.
- For the synthesis of the microspheres using the suspension polymerization method, the products exhibit broad size distribution which in turn, will affect the constituency and quality of the pellet (testing disk) packing. Whenever the interstitial voids and the granular sizes have become the prime parameter of studying in the acoustical behavior, the viscoelastic or porous microspheres fabrication could be advanced by emulsion polymerization and seeded suspension polymerization techniques, with better upgrading in morphology and monodispersity,
- With regard to the EMI shielding capability of nickel coating, the hybrid and metallized microspheres energy damping capability will not be limited to the acoustical attenuation studies. The present sound attenuation kit can be modified as a measuring device in EMI study, when the proper electromagnetic wave generator and detector can be replaced and fastened in similar designed testing tube. Furthermore, the metallization (chemical reduction or electroless plating) of polymer beads by other kinds of metals, e.g. copper, cobalt, silver, platinum is an

exciting trend in this research, in which the interfacial properties of different metallic grains with various polymer chains remain unexplored and deserve greater attention and examination.

In conclusion, the viscoelastic and porous properties of the three novel types of microspheres were ascertained to be useful of energy damping, which was evidenced in substantial enhancement in acoustical and ultrasonic attenuation. The versatility of metallization by means of electroless plating and chemical reduction enabled further advance noise damping in certain frequency ranges. The conventional methods in terms of material synthesis and surface modification possess great potential of redefining the dominance of state-of-the-art technique, provided that the investment in experimental and theoretical studies can be realized in near future.

References

Abrantes, L. M. and J. P. Correia. Polypyrrole Incorporating Electroless Nickel, Electrochim. Acta, 45, pp. 4179-4185. 2000.

Aklonis, J. J. and W. J. MacKnight. Introduction to Polymer Viscoelasticity, 2nd Edition. New York: Wiley-Interscience. 1983.

Allard, J. F. Propagation of Sound in Porous Media, Modeling Sound Absorbing Materials. Ch. 4 & 7, Essex, UK: Elsevier Applied Science Publisher Ltd. 1993.

Andrews, R. J. and E. Grulke. In Polymer Handbook, ed by J. Brandup, E. H. Immergut and E. Grulke, pp. VI/199. New York: John Wiley. 1999.

Arshady, R. and A. Ledwith. Suspension Polymerization and its Application to the Preparation of Polymer Supports, React. Polym., 1, pp. 159-174. 1983.

Athavale, V. T. and C. S. P. Iyer. Studies on Some Metal-Hydrazine Complexes, J. Inorg. Nucl. Chem., 29, pp.1003-1012. 1967.

Attenborough, K., J. M. Sabatier and C. Frederickson. The Sound Field within a Rigid Porous Layer, Appl. Acoust., 45, pp. 283-296. 1995.

Barber, A. Handbook of Noise and Vibration Control, 6th Edition. pp. 315-324, Oxford, UK: Elsevier Science Publisher Ltd. 1992.

Bathen, D. Physical Waves in Adsorption Technology - An Overview, Sep. Purif. Technol., 33, pp. 163-177. 2003.

Benchekchou, B., M. Coni, H. V. C. Howarth and R. G. White. Some Aspects of Vibration Damping Improvement in Composite Materials, Compos. Part B - Eng., 29, pp. 809-817. 1998.

Bhansali, S. and D. K. Sood. A Novel Technique for Fabrication of Metallic Structures on Polyimide by Selective Electroless Copper Plating Using Ion Implantation, Thin Solid Films, 270, pp. 489-492. 1995.

Billmeyer, Jr. F. W. Textbook of Polymer Science, 3rd Edition. Ch. 6, pp. 132, New York: John Wiley & Sons, Inc. 1984.

Bort, D. N., S. I. Kuchanov and V. I. Zegel'man. Some Features of the Bulk (Suspension) Polymerization of Vinyl Chloride to High Degrees of Conversion, Polym. Sci. U.S.S.R., 17, pp. 3151-3158. 1975.

Boudjahem, A. G., S. Monteverdi, M. Mercy and M. M. Bettahar. Study of Nickel Catalysts Supported on Silica of Low Surface Area and Prepared by Reduction of Nickel Acetate in Aqueous Hydrazine, J. Catal., 221, pp. 325-334. 2004.

Boutin, B., P. Royer and J. L. Auriault. Acoustic Absorption of Porous Surfacing with Dual Porosity, Int. J. Solids Struct., 35, pp. 4709-4737. 1998.

Bradley, J. S., J. M. Millar, E. W. Hill, S. Behal, B. Chaudret and A. Duteil. Surface Chemistry on Colloid Metals: Spectroscopic Study of Adsorption of Small Molecules, Faraday Discuss., 92, pp. 225-268. 1991.

Brayner, R., G. Viau, G. M. da Cruz, F. Fievet-Vincent, F. Fievet and F. Bozon-Verduraz. Preparation, Characterization and Reactivity of Pd/Nb_2O_5 Catalysts in Hexa-1,5-diene Hydrogenation, Catal. Today, 57, pp. 187-192. 2000.

Breitbach, M. and D. Bathen. Influence of Ultrasound on Adsorption Processes, Ultrason. Sonochem., 8, pp. 277-283. 2001.

Brenner, A. and G. Riddell. Electroless Plating on Metals by Chemical Reduction, Journal of the Franklin Institute, 244, pp. 479-481. 1947.

Buravalla, V. R., C. Remillat, J. A. Rongong and G. R Tomlinson. Advances in Damping Materials and Technology, Smart Mater. Bull., 2001, pp. 10-13. 2001.

Cao, K., J. Yu, B. G. Li, B. F. Li, Z. R. Pan. Micron-Size Poly(methyl methacrylate) Particles by Dispersion Polymerization in Polar Media: 1. Particle Size and Particle Size Distribution, Chem. Eng. J, 78, pp. 211-215. 2000.

Chanaud, R. C., Effects of Geometry on the Resonance Frequency of Helmholtz Resonators, J. Sound Vib., 178, pp. 337-348. 1994.

Chen, B. H., L. Hong, Y. Ma and T. M. Ko. Effects of Surfactants in an Electroless Nickel-Plating Bath on the Properties of Ni-P Alloy Deposits, Ind. Eng. Chem. Res., 41, pp. 2688-2678. 2002.

Chung, D. D. L. Review: Materials for Vibration Damping, J. Mater. Sci., 36, pp. 5733-5737. 2001.

Chung, D. D. L. Structural Composite Materials Tailored for Damping, J. Alloy. Compd., 355, pp. 216-223. 2003.

Cummings, A. and S. P. Beadle. Acoustic Properties of Reticulated Plastic Foams, J. Sound Vib., 175, pp. 115-133. 1994.

Degen, A. and J. Macek. Preparation of Submicrometer Nickel Powders by the Reduction from Nonaqueous Media, Nanostruct. Mater., 12, pp. 225-228. 1999.

Dickey, N. S. and A. Selamet. Helmholtz Resonators: One-Dimensional Limit for Small Cavity Length-to-Diameter Ratios, J. Sound Vib., 195, pp. 512-517. 1996.

Domenech, S. C., E. Lima Jr., V. Drago, J. C. De Lima, N. G. Borges Jr., A. O. V. Avila, V. Soldi. Electroless Plating of Nickel-Phosphorus on Surface-Modified Poly(ethylene terephthalate) Films, Appl. Surf. Sci., 220, pp. 238-250. 2003.

Dowding, P. J. and B. Vincent. Suspension Polymerization to Form Polymer Beads, Colloid. Surface. A, 161, pp. 259-269. 2000.

Dowding, P. J., B. Vincent and E. Williams. Preparation and Swelling Properties of Poly(NIPAM) "Minigel" Particles Prepared by Inverse Suspension Polymerization, J. Colloid. Interf. Sci., 221, pp. 268-272. 2000.

Dressick, W. J., L. M. Kondracki, M. S. Chen, S. L. Brandow, E. Matijevic and J. M. Calvert. Characterization of a Colloidal Pd(II)-Based Catalyst Dispersion for Electroless Metal Deposition, Colloid. Surface. A, 108, pp. 101-111. 1996.

El-Aasser, M. S., R. Hu, V. L. Dimonie and L. H. Sperling. Morphology, Design and Characterization of IPN-Containing Structured Latex Particles for Damping Applications, Colloid. Surface. A, 153, pp. 241-253. 1999.

Erbay, E. and O. Okay. Macroporous Styrene-Divinylbenzene Copolymers: Formation of Stable Porous Structures during the Copolymerization, Polym. Bull., 41, pp. 379-385. 1998.

Esrom, H., R. Seebock, M. Charbonnier and M. Romand. Surface Activation of Polyimide with Dielectric Barrier Discharge for Electroless Metal Deposition, Surf. Coat. Tech., 125, pp. 19-24. 2000.

Esumi, K., K. Matshuisa and K. Torigoe. Preparation of Rodlike Gold Particles by UV Irradiation Using Cationic Micelles as a Template, Langmuir, 11, pp. 3285-3287. 1995.

Evans, E. J. and E. N. Bazley. Sound Absorbing Materials. London: Her Majesty's Stationery Office. 1960.

Feldheim D. L. and C. A. Foss, Jr. Metal Nanoparticles: Synthesis, Characterization and Applications. Ch 1, pp. 1-16, New York Basel: Marcel Dekker, Inc. 2002.

Finegen, I. C. and R. F. Gibson. Recent Research on Enhancement of Damping in Polymer Composite, Compos. Struct., 44, pp. 89-98. 1999.

Finegen, I. C. and R. F. Gibson. Analytical Modeling of Damping at Micromechanical Level in Polymer Composites Reinforced with Coated Fibers, Compos. Sci. Technol., 60, pp. 1077-1084. 2000.

Frenkel, S. Ya. On the Theory of Heterophase Polymerization - I. Molecular Weight Distribution in the Suspension Polymerization of a Water-Soluble Monomer, Polym. Sci. U.S.S.R., 4, pp. 136-146. 1963.

Frenkel, S., S. G. Lyubetskii and L. G. Shaltyko. The Theory of Heterophase Polymerization - III. Heterophase Polymerization in which the Polymer Precipitates as a Continuous Coagulum, Polym. Sci. U.S.S.R., 5, pp. 726-733. 1964.

Garbassi, F., M. Morra and E. Occhiello. Polymer Surfaces: From Physics to Technology. Ch. 1 & 2, West Sussex, UK: John Wiley & Sons Ltd. 1998.

Grigore, L. Metallic Microstructures by Electroplating on Polymers: An Alternative to LIGA Technique, Mat. Sci. Eng. B - Solid, 74, pp. 299-303. 2000.

Grulke, E. A. Suspension Polymerization. In Encyclopedia of Polymer Science and Engineering, 2nd Edition, Vol. 16, ed by H. F. Mark, N. M. Bikales, C. G. Overberger, G. Menges and J. I. Kroshwitz. New York: John Wiley & Sons. 1989.

Han, E. G., E. A. Kim and K. W. Oh. Electromagnetic Interference Shielding Effectiveness of Electroless Cu-Plated PET Fabrics, Synthetic Met., 123, pp. 469-476. 2001.

Hashim, S. and B. W. Brooks. Drop Mixing in Suspension Polymerization, Chem. Eng. Sci., 57, pp. 3703-3714. 2002.

Hofmann, F. and K. Delbruck. (to Farbenfabriken Bayer) Ger Pat. 250,690 (1909); 254,672 (1912); 255,129 (1912).

Howe, M. S. On the Helmholtz Resonator, J. Sound Vib., 45, pp. 427-440. 1976.

Hu, R., V. L. Dimonie, M. S. El-Aasser, R. A. Pearson, A. Hiltner, S. G. Mylonakis and L. H. Sperling. Multicomponent Latex IPN Materials: 1. Morphology Control, J. Polym. Sci. Polym. Chem., 35, pp. 2193-2206. 1997.

Hu, R., V. L. Dimonie, M. S. El-Aasser, R. A. Pearson, A. Hiltner, S. G. Mylonakis and L. H. Sperling. Multicomponent Latex IPN Materials: 2. Damping and Mechanical Behavior, J. Polym. Sci. Polym. Phys., 35, pp.1501-1514. 1997.

Huang, C. Y. and W. W. Mo. The Effect of Attached Fragments on Dense Layer of Electroless Ni/P Deposition on the Electromagnetic Interference Shielding Effectiveness of Carbon Fiber/Acrylonitrile-Butadiene-Styrene Composites, Surf. Coat. Tech., 154, pp. 52-62. 2002.

Hunter, R. J. Introduction to Modern Colloid Science. Ch.1, New York: Oxford University Press Inc. 1993.

Jarzynski, J. Mechanisms of Sound Attenuation in Materials. In Sound and Vibration Damping with Polymers, ACS Symposium Series 424, ed by R. D. Corsaro and L. H. Sperling, pp. 167-207. Washington, DC: American Chemical Society. 1990.

Jarzynski, J., E. Balizer, J. J. Fedderly and G. Lee. Acoustic Properties. In Encyclopedia of Polymer Science and Technology, 3rd Edition, Vol. 3, ed by H. F. Mark and J. I. Kroschwitz. Hoboken, New Jersey: John Wiley & Sons, Inc. 2003.

Jiang, G., M. Gilbert, D. J. Hitt, G. D. Wilcox and K. Balasubramanian. Preparation of Nickel Coated Mica as a Conductive Filler, Compos. Part A - Appl. S., 33, pp. 745-751. 2002.

Jo. W. H. and J. S. Yang. Molecular Simulation Approaches for Multiphase Polymer Systems, Adv. Polym. Sci., 156, pp.1-52. 2002.

Jones, D. I. G. Handbook of Viscoelastic Vibration Damping. Ch. 2 & 3, Chichester, West Sussex, UK: John Wiley & Sons, Ltd. 2001.

Kaltenpoth, G., M. Himmelhaus, L. Slansky, F. Caruso and M. Grunze. Conductive Core-Shell Particles: An Approach to Self-Assembled Mesoscopic Wires, Adv. Mater., 15, pp. 1113-1118. 2003.

Kangwasupamonkon, W., S. Damronglerd and S. Kiatkamjornwong. Effects of the Crosslinking Agent and Diluents on Bead Properties of Styrene-Divinylbenzene Copolymers, J. Appl. Polym. Sci., 85, pp. 654-669. 2002.

Kawaguchi, H. Functional Polymer Microspheres, Prog. Polym. Sci., 25, pp. 1171-1210. 2000.

Kim, J. W. and K. D. Suh. Highly Monodisperse Crosslinked Polystyrene Microparticles by Dispersion Polymerization, Colloid. Polym. Sci., 276, pp. 870-878. 1998.

Kim, S. S., S. T. Kim, J. M. Ahn and K. H. Kim. Magnetic and Microwave Absorbing Properties of Co-Fe thin Films Plated on Hollow Ceramic Microspheres of Low Density, J. Magn. Magn. Mater., 271, pp. 39-45. 2004.

Kishimoto, S. and N. Shinya. Development of Metallic Closed Cellular Materials Containing Polymers, Mater. Design, 21 pp. 575-578. 2000.

Kolarz, B. N., M. Wojaczynska, J. Bryjak and B. Pawlow. Comparison between Structure and Some Properties of Methacrylonitrile and Acrylonitrile Macroporous Copolymers, React. Polym., 23, pp. 123-130. 1994.

Kuttruff, H. Room Acoustics, 4th edition. Ch. 6, New York: Elsevier Science Publishers Ltd. 2000.

Kuzmik, J. J. Plating on Plastics. In Electroless Plating: Fundamentals and Applications, ed by G. O. Mallory and J. B. Hajdu, Ch. 14. Orlando, Florida: American Electroplaters and Surface Finishers Society. 1990.

Leff, D. V., P. C. Ohara, J. R. Heath and W. M. Gelbart. Thermodynamic Control of Gold Nanocrystal Size: Experiment and Theory, J. Phys. Chem., 99, pp. 7036-7041. 1995.

Lewin, D. R. Modeling and Control of an Industrial PVC Suspension Polymerization Reactor, Comput. Chem. Eng., 20, pp. 865-870. 1996.

Li, H. X., W. J. Wang, H. Y. Chen and J. F. Deng. Surface Morphology and Electronic State Characterization of Ni-P Amorphous Alloy Films, J. Non-Cryst. Solids, 281, pp. 31-38. 2001.

Li, Y. D., C. W. Li, H. R. Wang, L. Q. Li and Y. T. Qian. Preparation of Nickel Ultrafine Powder and Crystalline Film by Chemical Control Reduction, Mater. Chem. Phys., 59, pp. 88-90. 1999.

Liang, Y. C., F. Svec and J. M. J. Frechet. Preparation and Functionalization of Reactive Monodisperse Macroporous Poly(chloromethylstyrene-co-styrene-co-divinylbenzene) Beads by a Staged Templated Suspension Polymerization, J. Polym. Sci. Polym. Chem., 35, pp. 2631-2643. 1997.

Lim, V. W. L., E. T. Kang and K. G. Neoh. Electroless Plating of Palladium and Copper on Polypyrrole Films, Synthetic Met., 123, pp. 107-115. 2001.

Machado, R. A. F. and A. Bolzan. Control of Batch Suspension Polymerization Reactor, Chem. Eng. J., 70, pp. 1-8. 1998.

Macoveanu, M., E. Bezdadea and D. Feldman. The Stereoregularity of Poly(vinyl chloride) Obtained by Suspension Polymerization with Temperature Program, Eur. Polym. J., 13, pp. 165-167. 1977.

Mallory, G. O. and J. B. Hajdu. Electroless Plating: Fundamentals and Applications. Ch. 1, 4 & 7, Orlando, Florida: American Electroplaters and Surface Finishers Society. 1990.

Maschio, G., T. Bello and C. Scali. Optimization of Batch Polymerization Reactors: Modeling and Experimental Results for Suspension Polymerization of Methyl Methacrylate, Chem. Eng. Sci., 47, pp. 2609-2614. 1992.

Meenan, B. J., N. M. D. Brown and J. W. Wilson. Characterization of $PdCl_2/SnCl_2$ Electroless Plating Catalyst System Adsorbed on Barium Titanate-Based Electroactive Ceramics, Appl. Surf. Sci., 74, pp. 221-233. 1994.

Mehta, M., J. Johnson and J. Rocafort. Architectural Acoustics: Principles and Design. Ch. 4 & 5, Appendix H & J, Upper Saddle River, New Jersey: Prentice Hall. 1999.

Menard, K. P. Dynamic Mechanical Analysis. A Practical Introduction. Ch. 1 & 2, Washington, DC: CRC Press. 1999.

Mendizabal, E., J. R. Castellanos-Ortega and J. E. Puig. A Method for Selecting a Polyvinyl Alcohol as Stabilizer in Suspension Polymerization, Colloid Surface, 63, pp. 209-217. 1992.

Muller, G., D. W. Baudrand, G. D. R. Jarrett and C. R. Draper. Plating on Plastics, 2nd Edition. Ch.10 & 11, Teddington, England: Robert Draper Ltd. 1970.

Nicholls, D. and R. Swindells. Hydrazine Complexes of Nickel (II) Chloride, J. Inorg. Nucl. Chem., 30, pp. 2211-2217. 1968.

Okay, O. Prog. Polym. Sci., 25, pp. 711-779. 2000.

Okubo, M., Y. Konishi and H. Minami. Production of Hollow Polymer Particles by Suspension Polymerization, Colloid. Polym. Sci., 276, pp. 638-642. 1998.

Okubo, M., Y. Konishi, T. Inohara and H. Minami. Size Effect of Monomer Droplets on the Production of Hollow Polymer Particles by Suspension Polymerization, Colloid. Polym. Sci., 281, pp. 302-307. 2003.

Omi, S., A. Matsuda, K. Imamura, M. Nagai and G. H. Ma. Synthesis of Monodisperse Polymeric Microspheres Including Polyimide Prepolymer by Using SPG Emulsification Technique, Colloid. Surfaces. A, 153, pp. 373-381. 1999.

Omidian, H., M. J. Zohuriaan-Mehr and H. Bouhendi. Polymerization of Sodium Acrylate in Inverse-Suspension Stabilized by Sorbitan Fatty Ester, Eur. Polym. J., 39, pp. 1013-1018. 2003.

Perez-Herranz, V., M. Garcia-Gabaldon, J. L. Guinon and J. Garcia-Anton. Effect of Citric Acid and Hydrochloric Acid on the Polarographic Behaviour of Tin: Application to the Determination of Tin (II) in Presence of Tin (IV) in the Activating Solutions of the Electroless Plating of Polymers, Anal. Chim. Acta, 484, pp. 243-251. 2003.

Pessel, L., U. S. Pat. 2,430,581 (1947)

Pierce, A. D. Acoustics: An Introduction to its Physical Principal and Applications. New York: Acoustical Society of America, McGraw-Hill, Inc. 1989.

Popov, V. A., Ye. P. Shvarev, Yu. A. Zvereva, I. Pen'kov and G. P. Gladyshev. The Problem of the Acceleration of Suspension Polymerization of Vinyl Chloride at High Conversion, Polym. Sci. U.S.S.R., 17, pp. 1403-1406. 1975.

Raichel, D. R. The Science and Applications of Acoustics. New York: Springer-Verlag Inc. 2000.

Rege, S. U., R. T. Yang and C. A. Cain. Desorption by Ultrasound: Phenol on Activated Carbon and Polymeric Resin, AICHE J., 44, pp. 1519-1528. 1998.

Riedel, W. Electroless Nickel Plating. Ch. 1, pp. 1-4, Stevenage, Hertfordshire, England: Finishing Publications Ltd. 1991.

Riqueza E. C., A. P. de Aguiar, L. C. de S. Maria and M. M. P. de Aguira. Modification of Porous Copolymers Network Based on Acrylonitrile, Polym. Bull., 48, pp. 407-414. 2002.

Romand, M., M. Charbonnier, M. Alami and J. Baborowski. Electroless Metallization of Polymers: Simplification of the Process by Using Plasma or UV-Laser Pretreatment. In Metallized Plastics 5 & 6: Fundamental and Applied Aspects, ed by K. L. Mittal, pp. 3-23. Utrecht: VSP. 1998.

Roux, F. A. U. S. Pat. 1,207,218 (1916).

Saeki, Y. and T. Emura. Technical Progress for PVC Production, Prog. Polym. Sci., 27, pp. 2055-2131. 2002.

Shaltyko, L. G., V. G. Baranov, T. I. Volkov, V. V. Lutsenko and S. Ya. Frenkel. Theory of Heterophase Polymerization - II. Comparison of Molecular Weight Distribution of Polymers Prepared under Conditions of Homo- and Heterophase Polymerization, Polym. Sci. U.S.S.R., 5, pp. 630-637. 1964.

Shukla, S., S. Seal, J. Akesson, R. Oder, R. Carter and Z. Rahman. Study of Mechanism of Electroless Copper Coating of Fly-Ash Cenosphere Particles, Appl. Surf. Sci., 181, pp. 35-50. 2001.

Shukla, S., S. Seal, Z. Rahaman and K. Scammon. Electroless Copper Coating of Cenospheres Using Silver Nitrate Activator, Mater. Lett., 57, pp. 151-156. 2002.

Shvarev, Ye. P., Z. S. Zakharova and S. A. Nikitina. The Effect of Low Molecular Weight Surfactants on the Strength of Methyl Cellulose Adsorption Layers during Vinyl Chloride Suspension Polymerization, Polym. Sci. U.S.S.R., 17, pp. 82-87. 1975.

Smith, B. J., R. J. Peters and S. Owen. Acoustics and Noise Control, 2nd Edition. Ch. 1, Harlow, Essex: Addison Wesley Longman. 1996.

Sophiea, D., D. Klempner, V. Sendijarevic, B. Suthar and K. C. Frisch. Interpenetrating Polymer Networks as Energy-Absorbing Materials. In Interpenetrating Polymer Networks, Advances in Chemistry Series 239, ed by D.

Klempner, L. H. Sperling and L. A. Utracki. Washington, DC: American Chemical Society. 1994.

Souleimanova, R. S., A. S. Mukasyan and A. Varma. Study of Structure Formation during Electroless Plating of Thin Metal-Composite Membranes, Chem. Eng. Sci., 54, pp. 3369-3377. 1999.

Sperling, L. H. and V. Mishra. The Current Status of Interpenetrating Polymer Networks, Polym. Advan. Technol., 7, pp. 197-208. 1996.

Sperling, L. H. Interpenetrating Polymer Networks: An Overview. In Interpenetrating Polymer Networks, Advances in Chemistry Series 239, ed by D. Klempner, L. H. Sperling and L. A. Utracki. Washington, DC: American Chemical Society. 1994.

Sperling, L. H. IPN around the World II: Recent Advances. In Advances in Interpenetrating Polymer Networks, Vol. 4, ed by D. Klempner and K. C. Frisch. Lancaster, Pennsylvania: Technomic Publishing Company, Inc. 1994.

Sperling, L. H. Polymer Multicomponent Materials: An Introduction, New York: Wiley. 1997.

Sperling, L. H. Introduction to Physical Polymer Science, 3rd Edition. Ch. 8 & 9, New York: John Wiley & Sons, Ltd. 2001.

Stupenkova, L. L., T. A. Baiburdov, V. F. Gromov and E. N. Teleshov. Inverse Suspension Polymerization of Acrylamide, Polym. Sci. U.S.S.R., 33, pp. 1388-1394. 1991.

Sugihara, S., S. Okada, H. Ohtsuka, J. Yamaki. Effects of the Surface State of Plastics on Adhesive Strength in Electroless Plating, J. Appl. Polym. Sci., 59, pp. 1751-1758. 1996.

Toshima, N. and Y. Wang. Polymer-Protected Cu/Pd Bimetallic Clusters, Adv. Mater., 6, pp. 245-247. 1994.

Toshima, N., T. Teranishi, H. Asanuma and Y. Saito. Platinum Cluster Catalyst Supported on Porous Chelate Resin-Metal Complexes: Effect of Resin Porosity on Catalytic Activity, J. Phys. Chem., 96, pp. 3796-3799. 1992.

Tzeng, S. S. and F. Y. Chang. EMI Shielding Effectiveness of Metal-Coated Carbon Fiber-Reinforced ABS Composites, Mat. Sci. Eng. A - Struct., 302, pp. 258-267. 2001.

Vivaldo-Lima, E., P. E. Wood, A. E. Hamielec and A. Penlidis. An Updated Review on Suspension Polymerization, Ind. Eng. Chem. Res., 36, pp. 939-965. 1997.

Voronina, N. An Empirical Model for Rigid Frame Porous Materials with High Porosity, Appl. Acoust., 51, pp. 181-198. 1997.

Voronina, N. An Empirical Model for Elastic Porous Materials, Appl. Acoust., 55, pp. 67-83. 1998.

Voronina, N. N. and K. V. Horoshenkov. A New Empirical Model for the Acoustic Properties of Loose Granular Media, Appl. Acoust., 64, pp. 415-432. 2003.

Wang, P. H. and C. Y. Pan. Polymer Metal Composite Microspheres: Preparation and Characterization of Poly(St-co-AN)Ni Microspheres, Eur. Polym. J., 36, pp. 2297-2300. 2000.

Warshawsky, A. and D. A. Upson. Zerovalent Metal-Polymer Composites via Electroless Deposition on Functional Polymer, Polymer, 30, pp. 972-973. 1989.

Webb P. A. Volume and Density Determinations for Particle Technologists, Micromeritics Instrument Corporation Technical Report. 2001.

Webb, P. A. and C. Orr. Analytical Methods in Fine Particle Technology. Ch. 4, Norcoss, GA: Micromeritics Instrument Corporation. 1997.

Wen, G, Z. X. Guo and C. K. L. Davies. Microstructural Characterization of Electroless-Nickel Coatings on Zirconia Powder, Scripta Mater., 43, pp. 307-311. 2000.

Wojaczynska, M. and B. N. Kolarz. Structure of Some Styrene-Divinylbenzene Copolymers, J. Appl. Polym. Sci., 56, pp. 433-439. 1995.

Wunderlich, B. The Basis of Thermal Analysis. In Thermal Characterization of Polymeric Materials, 2nd Edition, Vol. 1, ed by E. A, Turi, Ch. 2. San Diego: Academic Press. 1997.

Xu, L. N., K. C. Zhou, H. F. Xu, H. Q. Zhang, L. Huang, J. H. Liao, A. Q. Xu, N. Gu, H. Y. Shen and J. Z. Liu. Copper Thin Coating Deposition on Natural Pollen Particles, Appl. Surf. Sci., 183, pp. 58-61. 2001.

Xu, M. C.; Z. Q. Shi, R. F. Shi, J. X. Liu, Y. Lu and B. L. He. Synthesis of the Absorbent Based on Macroporous Copolymer MA-DVB Beads and its Applications in Purification for the Extracts from Ginkgo Biloba Leaves, React. Funct. Polym., 43, pp. 297. 2000.

Yahya, G. O., S. K. A. Ali and E. Z. Hamad. Surface and Interfacial Activities of Hydrophobically Modified Poly(vinyl alcohol) (PVA), Polymer, 37, pp. 1183-1188. 1996.

Yak, S. In Advances in Interpenetrating Polymer Networks, Vol. 4, ed by D. Klempner and K. C. Frisch. Lancaster, PA: Technomic Publishing Company. 1994.

Yang, B., K. Takahashi and M. Takeishi. Styrene Drop Size and Size Distribution in an Aqueous Solution of Poly(vinyl alcohol), Ind. Eng. Chem. Res., 39, pp. 2085-2090. 2000.

Yin, X. and L. Hong. Role of a Pb^{2+} Stabilizer in the Electroless Nickel Plating System: A Theoretical Exploration, J. Phys. Chem. B, 108, pp. 10919-10929. 2004.

Yuan, H. G., G. Kalfas and W. H. Ray. Suspension Polymerization, J. Macromol. Sci. R. M. C., 31, pp. 215-299. 1991.

Zarr, R. R., M. W. Davis and E. H. Anderson. Room-Temperature Thermal Conductivity of Expanded Polystyrene Board for a Standard Reference Material, National Institute of Standards and Technology Interagency Report (NISTIR), 5838, pp. 1-39. 1996.